12-2008

Physics of Type Ia Supernovae

Ginger Bryngelson
Clemson University, gbrynge@clemson.edu

PHYSICS OF TYPE IA SUPERNOVAE

A Thesis
Presented to
the Graduate School of
Clemson University

In Partial Fulfillment
of the Requirements for the Degree
Master of Science
Physics

---

by
Ginger Bryngelson
December 2008

Accepted by:
Dr. Mark D. Leising, Committee Chair
Dr. Jeremy King
Dr. Bradley Meyer

ABSTRACT

Type Ia supernovae (SNe Ia), the thermonuclear explosion of a white dwarf, were once considered standard candles. However, increased observations reveal inhomogeneities in chemical composition and luminosity behavior, roughly dividing SNe Ia into three luminosity classes; super-luminous, sub-luminous, and normally-luminous. After introducing the problem in the context of previous observations and modeling, this thesis explores the physical processes occurring in a SN Ia after explosion, and discusses observations of SN light curves.

A simple model of the expanding ejecta calculates the energy deposition from the decay of radioactive ^{56}Ni as well as photon diffusion. It produces light curves that match early bolometric observations of normal SNe Ia. Variable chemical composition of the ejecta allows for testing a number of explosion scenarios. It becomes apparent that the shape of the light curve is sensitive to the amount and location of synthesized ^{56}Ni. Monitoring gamma ray transport through Compton scattering indicates that gamma rays escape at late times. At this epoch an assumption of instantaneous deposition of energy is inaccurate. It is unclear whether positrons escape the ejecta or are trapped at even later times.

The photometry of SN2007ax proved it to be the dimmest and reddest SN Ia observed. SN2008D was serendipitously observed in X-rays before it was even visible in optical light, revealing that an early x-ray outburst may accompany every core collapse SN. Subsequent observations resulted in a well-sampled, multi-band early light curve. Observations of SN2006D, another SN Ia, in B, V, R, I up to ~ 500 days after maximum light are also presented. The light curve may answer questions about the physics of SNe at late times, if more observations can be included. Future modifications of the simple model and strategies for useful observations are discussed.

DEDICATION

This thesis is dedicated to my parents and brother. Your unconditional love and support carry me through any trial I choose to face. And sharing the joy of my successes with you makes it worth the journey. I love you so much.

ACKNOWLEDGEMENTS

I would like to express my gratitude first and foremost to my advisor, Dr. Mark Leising. Your guidance and patience have helped me to understand the intricacies of SNe Ia, and also enhanced my general curiosity. I appreciate your tireless willingness to answer my questions. I also want to thank my committee, Dr. Jeremy King and Dr. Brad Meyer (and also Dr. Dieter Hartmann who might as well have been on my committee), for their continual guidance and interest in my graduate career. I want to thank Dr. Peter Milne for his invaluable help in observations and photometry, and for the chance to work with data from Super-LOTIS.

I also want to thank the many graduate students whose help and witty banter was instrumental in either my use of linux/photometry/idl, or my understanding of the physics of the cosmos. These include Roggie Boone, Eric Bubar, Blake Miller, Matt Troutman, Bethany Johns, Adria Updike, Keith Davis, Allen Parker, Mark Theiling, Brian Donehew, Joe Liskowsky, and Yu Chen.

A special thanks to Yu, Joe, and Tatsiana. Your friendship has brightened my life in Clemson, and kept me sane, happy, and cheerful.

TABLE OF CONTENTS

LIST OF FIGURES

List of Figures (Continued)

CHAPTER 1
INTRODUCTION

A supernova is the explosive end to a massive star's life, or, for a low mass star, is a fiery alternative to an otherwise dismal smoldering existence. These explosions can produce 100 times as much energy as the sun produces in its entire lifetime, and can temporarily rival the brightness of an entire galaxy. They enrich their surroundings with heavy elements formed in the explosion, and the next generation of stars inherits these heirlooms as they begin their own lives.

Type Ia supernovae have served as "standard candles," enabling astrophysicists to measure distances to galaxies over 1000 Mpc away. They have shed light on the shape and cosmological fate of the universe and may also play a major role in the emission of 511keV positron annihilation photons seen mostly in the bulge of the Galaxy. Their astrophysical importance begs further understanding.

Supernova Classification

Types of supernovae (SNe) were first distinguished phenomenologically through spectroscopic analysis. They were broken up into two main classes: those which contained no hydrogen lines (Type I), and those that exhibited strong hydrogen lines (Type II). Type I SNe were broken down further into categories of; Type Ia: those with strong silicon lines, Type Ib: strong helium lines, and Type Ic: neither strong silicon nor helium lines. A spectrum of each type can be seen in Figure 1.1. However, the physical differences in these systems categorizes the groups much differently.

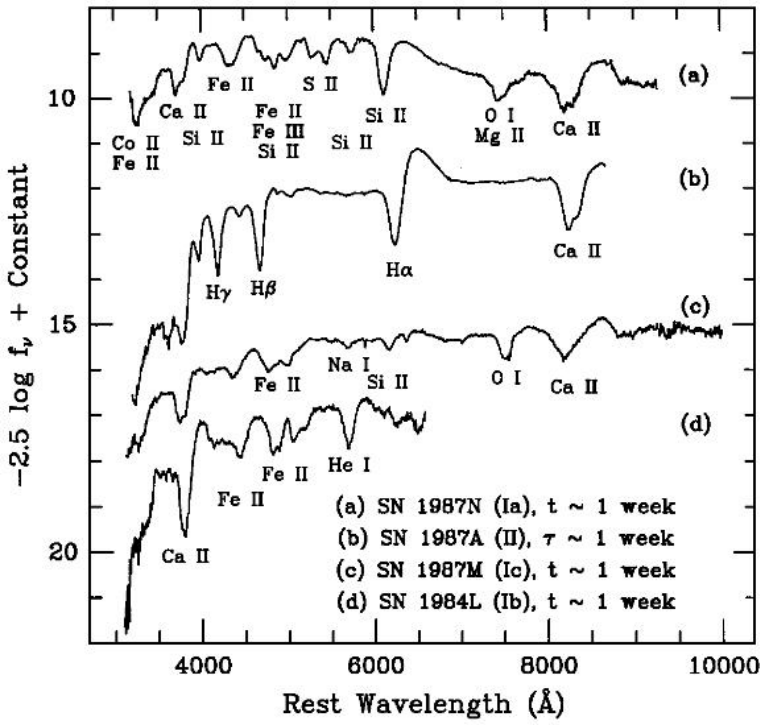

Figure 1.1 From Filippenko (1997). The early spectrum of the Type Ia,b,c and Type II supernova. t and τ are time after B-band maximum, or time after core collapse. Note the presence/abscence of Hydrogen/Helium which defines the SN Type.

1.1 Core Collapse Supernovae

Type II, Type Ib, and Type Ic SN are each the result of a massive star undergoing gravitational collapse and are thus collectively called core-collapse SNe (CC-SNe). After the helium burning stage, stars that are more massive than about 8 $M_\odot$ undergo burning of their carbon core, then succesively neon, oxygen, and silicon, generating progressively more massive products. These phases of nuclear burning temporarily halt the gravitational contraction by generating outward radiation pressure — photons "pushing" their way out of the star. Silicon burning produces a number of nuclei (incremented by alpha particles) all the way up to ^{56}Ni — the nucleus at which the binding energy per nucleon peaks for the ^{4}He capture chain. The reactions occur as:

$$^{28}\mathrm{Si} + {}^4\mathrm{He} \rightarrow {}^{32}\mathrm{S} + \gamma \tag{1.1}$$

$$^{32}\mathrm{S} + {}^4\mathrm{He} \rightarrow {}^{36}\mathrm{Ar} + \gamma \tag{1.2}$$

$$etc$$

$$^{52}\mathrm{Cr} + {}^4\mathrm{He} \rightarrow {}^{56}\mathrm{Fe} + \gamma. \tag{1.3}$$

At this point the pressure is so great, and the temperature high enough ($T \sim 2.5 \times 10^9$) that photons have enough energy to destroy heavy nuclei in a process known as photodisintegration (essentially the reverse of the above silicon burning) (Kotake et al., 2006). The photodisintegration of ^{4}He is,

$$^4\mathrm{He} + \gamma \rightarrow 2p^+ + 2n. \tag{1.4}$$

This deprives the star's core of thermal energy it would otherwise use to keep itself from collapsing. Heavy nuclei and protons (produced from the photodisintegration of ^{4}He) begin capturing the free electrons that had helped support the star through degeneracy pressure. Thus the star contracts rapidly until the repulsive nuclear strong force halts the inner core at a density $\rho > 3 \times 10^{14} g/cm^3$ (Kotake et al., 2006). The inner core rebounds, sending pressure waves into the infalling outer core. The pressure waves reach the speed of sound and turn into a shockwave, creating high temperatures as it travels through the still inwardly-traveling iron core. This instigates photodisintegration which saps the shock of

its energy. Here, the shock would stall if it were not for the neutrinos also created during the photodisintegration and electron capture. Though neutrinos are typically considered non-interacting particles, the density of the core is such that the energy of about 5% of the neutrinos is deposited into material just behind the shock. This deposition re-invigorates the shock. The production of neutrinos is enormous, and just 5% of their total energy is enough to generate a CC-SN of $E = 1 \times 10^{51}$ ergs[1] (Kotake et al., 2006).

The spectroscopic difference between SNe II, Ib, and Ic derives from the fact that these massive stars are at different stages in mass loss when Si burning begins. SNe Ib progenitors have had their outer hydrogen shell stripped away by stellar winds prior to the time of explosion, while SNe Ic progenitors have had even their helium shell stripped away. Because core-collapse supernovae are associated with massive stars, they are usually found in younger stellar populations — typically in the arms of spiral galaxies. None have been found in elliptical galaxies.

1.2 Type Ia Supernovae

Unlike CC-SNe, Type Ia supernovae (SNe Ia) are found in all types of galaxies — indicating that their progenitors have long lifetimes. Observationally, most SNe Ia have similar peak absolute magnitudes, brightness decline rates (light curves), and spectral evolution. This remarkable homogeneity led to their use as distance indicators and subsequently allowed astronomers to conclude that the universe is expanding at an accelerated rate (see appendix A).

The historically accepted explosion model that agrees well with most SNe Ia observations is the single-degenerate Chandrasekhar-mass explosion model (Hillebrandt and Niemeyer, 2000). In this case "single-degenerate" refers to one white dwarf (of mostly carbon and oxygen) whose core is electron degenerate. Left to its own devices, the white dwarf (WD) would spend its years simply cooling off (see appendix B). However, in a close binary system with another star, it may accrete mass from its companion and so begin the path to a more violent death. The WD increases in mass until it reaches the Chandrasekhar mass

[1] 1×10^{51} ergs is also known as one "foe," or one "bethe."

limit (1.39 $M_{\odot}$ for a carbon-oxygen WD) where electron degeneracy pressure can no longer support it against its own gravity. The star contracts enough to ignite its core of carbon resulting in a Chandrasekhar-mass explosion.

The burning front moves subsonically (a deflagration) – up to 30% the speed of sound – through the star, consuming fuel and releasing energy, until "quenched by expansion" (Hillebrandt and Niemeyer, 2000, and references therein). The deflagration creates iron peak elements in the central regions where the density is the highest. Yet in the outer layers, there is incomplete nuclear burning which produces intermediate mass elements (IME) such as ^{40}Ca, ^{32}S, ^{28}Si, & ^{20}Ne and even leaves unburned ^{12}C & ^{16}O, & ^{24}Mg (Hillebrandt and Niemeyer, 2000). The W7 model by Nomoto et al. (1984) is a widely accepted deflagration model that successfully reproduces the observed light curve (Section 1.2.1) and spectra (Section 1.2.2) of most SNe Ia. Other possible explosion scenarios are discussed in Sections 1.3.3 & 1.4.3.

Each observation produces more constraints on the explosion mechanism of SNe Ia. Most observations consist of 1) monitoring the rate of decline in luminosity — quantified in what is called a light curve, or 2) taking spectra, which indicate the chemical compostion and speed of the ejecta.

1.2.1 Light Curve

Figure 1.2 shows composite light curves from 22 SNe Ia from Riess et al. (1999) in *B,V,R,I*. The optical light curves are characterized by a fast rise-time and a delayed decline (.06 mag/day at early times, and .107 mag/day later) (Filippenko, 1997). However, to understand the shape of the light curve, we must examine the processes that occur in the ejecta.

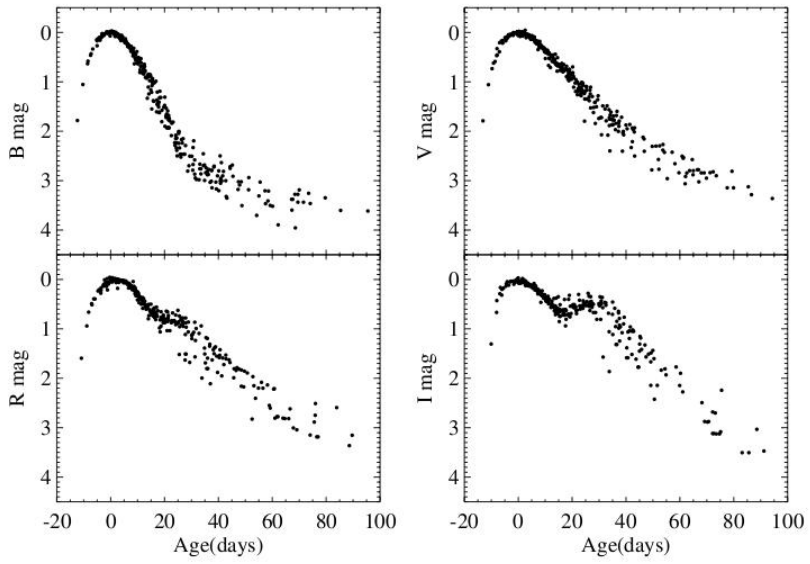

Figure 1.2 From Riess et al. (1999). A composite of 22 SNe Ia light curves up to ~ 100 days after maximum light, normalized so that maximum light is at a magnitude of 0.

The initial thermal energy of the SN explosion is transformed into kinetic energy by adiabatic expansion before it can be radiated. Thus the observed luminosity of SNe Ia must have another source. Colgate and McKee (1969) were the first to suggest that the beta decay of the radioactive ^{56}Ni, synthesized in the explosion, powers the continual expansion and luminosity of SNe Ia. The decay schemes of $^{56}\mathrm{Ni} \rightarrow {}^{56}\mathrm{Co} \rightarrow {}^{56}\mathrm{Fe}$ (Nadyozhin, 1994) are shown in Figure 1.3. ^{56}Ni electron capture decays with a lifetime of $\tau_{\mathrm{Ni}} = 8.80$ days to an excited state of ^{56}Co, which decays — cascading through subsequent excited states — to the ground state, releasing photons of average energy 1.72 MeV.

$$^{56}\mathrm{Ni} + e^- \rightarrow {}^{56}\mathrm{Co}^* + \nu_e \tag{1.5}$$

$$^{56}\mathrm{Co}^* \rightarrow {}^{56}\mathrm{Co} + \gamma\text{'s} \tag{1.6}$$

^{56}Co then decays with a lifetime of $\tau_{\rm Co} = 111.3$ days into an excited state of ^{56}Fe through electron capture 81% of the time, and through beta decay 19% of the time.

$$^{56}\mathrm{Co} + e^- \rightarrow {}^{56}\mathrm{Fe}^* + \nu_e \quad (81\%) \tag{1.7}$$

$$^{56}\mathrm{Co} \rightarrow {}^{56}\mathrm{Fe}^* + e^+ + \nu_e \quad (19\%) \tag{1.8}$$

After which, the excited state (^{56}Fe*) decays through multiple photon emissions to the stable ground state of ^{56}Fe.

$$^{56}\mathrm{Fe}^* \rightarrow {}^{56}\mathrm{Fe} + \gamma\text{'s} \tag{1.9}$$

The decay produces gamma rays of typical energy $\sim$ 1 MeV, while the positron may have kinetic energy ranging from 0-1.459 MeV (with typical energy being 0.632 MeV) (Nadyozhin, 1994). If the positron annihilates, it will also produce photons. For more on positrons in SNe Ia, see Section 1.6.1.

At early times the SN Ia ejecta are optically thick, and all ^{56}Ni gamma rays are deposited, predominantly through Compton scattering (see section 2.5.1). This creates energetic electrons which then thermalize through excitation/de-excitation and ionization/recombination. The optical photons created in this manner diffuse through and eventually escape from the outer photosphere-like layers of the ejecta. At this "diffusion dominated" point, the radiative output can be approximated as a blackbody. But the ejecta, traveling at 11-13,000 km/s, continue to expand, and from 100 to 200 days after maximum light, the SN transitions to a nebular phase. The optical depth decreases, the diffusion timescale is shortened, trapping is less-efficient, and light escapes from further and further into the ejecta. Once in the nebular phase, the material is optically thin and completely transparent to the gamma rays. Now, only the deposition of kinetic energy of the positrons from the ^{56}Co $\rightarrow$ ^{56}Fe decay power the light curve. The fraction of positrons that do not escape is dependent on the configuration of the magnetic field (Milne et al., 2001, and references therein).

Thus, the light curve shapes (as seen in Figures 1.2 & 1.4) are built from the evolution of escaping thermal photons. In the beginning, the ejecta is optically thick, so the random walk of these photons requires a long time before they reach the surface.

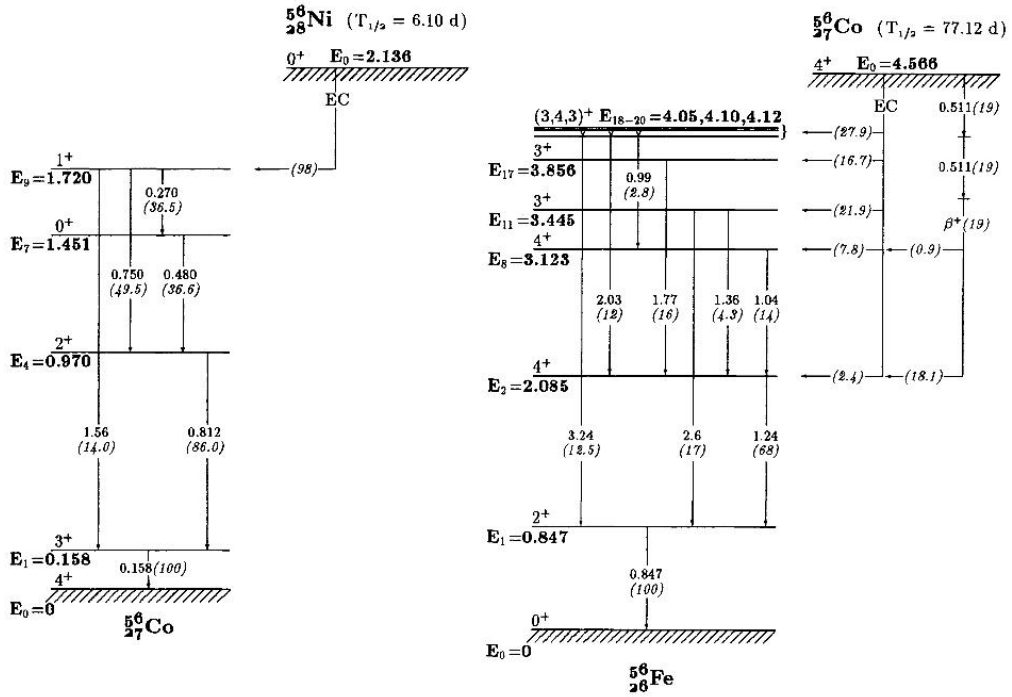

Figure 1.3 The simplified decay schemes of ^{56}Ni $\rightarrow$ ^{56}Co (left) and of ^{56}Co $\rightarrow$ ^{56}Fe (right) from Nadyozhin (1994). The number in parentheses at each transition is the percentage of photons per decay that undergo that transition, while the number in bold (if present) indicates the energy (in MeV) of the photon emitted.

Consequently, the light curve is initially dim, but progessively increases in luminosity as enough time has passed for more and more of these photons to escape. It is not until the amount of escaping energy catches up to the amount of built up energy that we see a maximum in the light curve (perhaps 18 days after explosion). The decrease that follows is due, in part, to the decreasing opacity. More gamma rays escape, thus less are energizing the ejecta.

Radiated photons in the ejecta tend to be in the UV and blue wavelengths, however the opacity at these wavelengths is very large. Radiation absorbed at these energies is redistributed through repeated fluorescences (Pinto and Eastman, 2000). An energetic photon excites a high-energy atomic transition, which de-excites in a cascade of lower energy transitions. The amount of light seen in an energy band depends on the number of transitions resulting in, and the monochromatic opacity for, each line in that energy band. Thus, each band exhibits a differently shaped light curve (as seen in Figure 1.4 taken from Kasen (2006)), which evolves differently with time.

At late times, the light curve in the infrared becomes more important as it begins to better trace the bolometric behavior. Section 1.6.2 discusses this in more depth.

1.2.2 Optical Spectra

While light curves reveal much about the energy release, spectra afford a peak into the chemical make-up, which tells much about the explosion mechanism.

Early spectra reveal deep Si II absorption lines and those of other IME, indicating that burning does not reach nuclear statistical equilibrium (NSE) in outer layers (Branch, 1982). Figure 1.5 shows the early spectrum of three typical SNe Ia. All exhibit the tell-tale deep Si absorption lines (at 6150 Å) as well as other IME lines (e.g., Ca II at $\sim$ 8300 Å). Note how remarkably similar these spectra are.

As time progresses, and the photosphere receeds further into the ejecta, we see fewer IME and more iron-group elements. Figure 1.6 shows the progression of spectra for a typical SN Ia.

Note at early times, the Si II absorption at λ6355 Å is strong, but starts to weaken after 2 weeks ($t \geq 14$ days). Also at 2 weeks, Fe II emission ($\lambda \sim 6500$ Å) and absorption

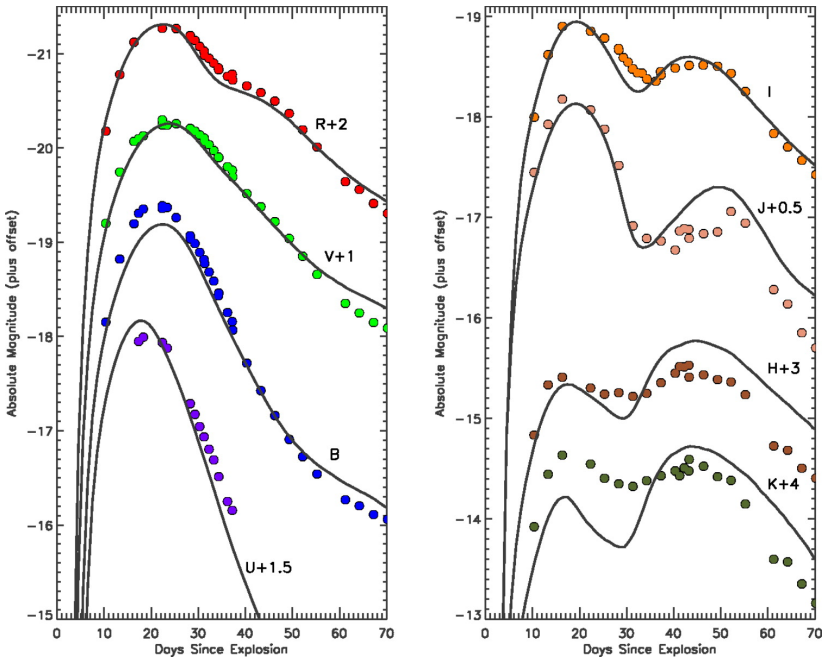

Figure 1.4 Taken from Kasen (2006), the light curves of the normally luminous SN Ia SN2001el (circles) plotted with models for U,B,V,R,I,J,H,K bands. Note the different timing of maximum light and disimilar shapes for each band — particularly, the secondary maximum in the NIR

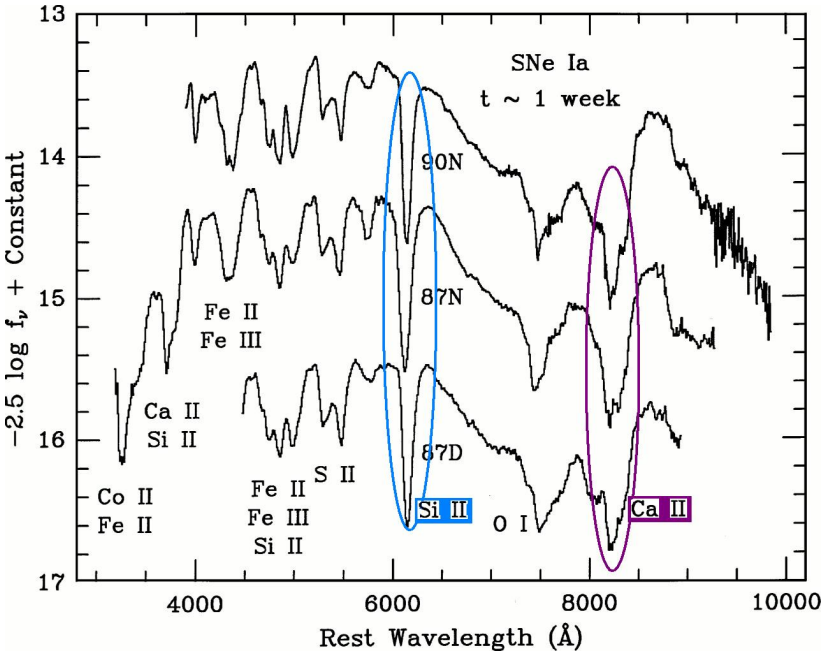

Figure 1.5 From Filippenko (1997), the optical spectra of SNe Ia (from top to bottom: SN1990N, SN1987N, SN1987D) arbitrarily offset vertically for better viewing. The deep Si II trough at 6150 Å is from blue-shifted Si II 6347 Å and 6371 Å lines — collectively called λ6355 Å. The early Si signature indicates incomplete nuclear burning in the outer layers of SNe Ia. The homogeneity of SNe Ia is evident in the notches present in each spectra (e.g., near 4550 Å, 4650 Å, and 5150 Å)

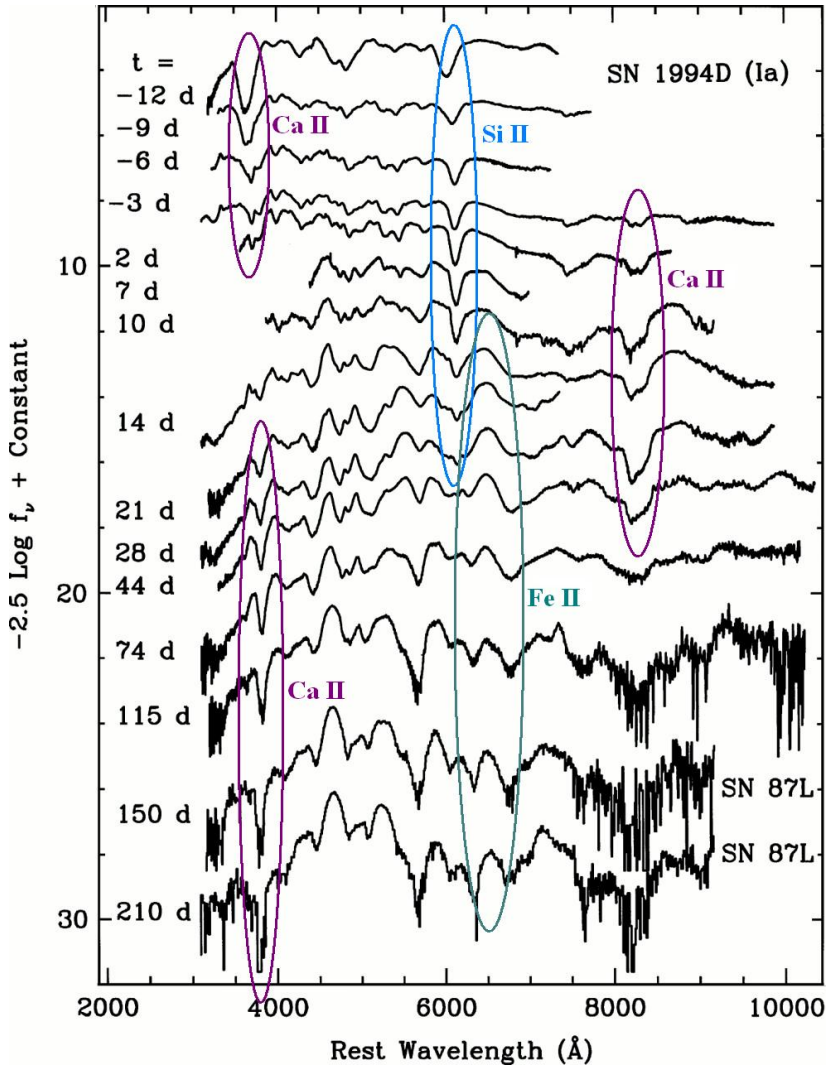

Figure 1.6 The progression of the optical spectra of normal SN Ia SN1994D from Filippenko (1997). Time is labeled on the left with $t = 0$ occuring at maximum light. See text for qualitative explanation. The last two spectra are of the similar SN1987L.

emerges, which is a hint that we're beginning to see the iron-rich core. There are still Ca II lines visible ($\lambda \sim 3800$ Å), but Co lines dominate and dozens of forbidden Fe emission lines can be seen. The decrease of Co lines is at a rate consistent with radioactive decay of ^{56}Co.

The single-degenerate Chandrasekhar-mass deflagration models seem to agree very well with the light curves and spectra seen in Figures 1.2 through 1.6. However, as observations increase, it becomes apparent that SNe Ia are not as homogeneous as previously assumed. Some SNe Ia appear much brighter (superluminous — see Section 1.3), and some much dimmer (subluminous — see Section 1.4), each accompanied by spectra that deviate from the typical (normally luminous) SNe Ia. The anomalous spectra and light curves might indicate different explosion mechanisms. These are discussed in the respective sections (1.3.3 & 1.4.3) relating to the luminosity class they describe. Though these peculiar SNe Ia have been observed in increasing numbers (e.g. Appendix C), "normal" SNe account for 64% of observed SNe Ia according to Li et al. (2001b). Only 20% of observed SNe Ia are superluminous and 16% are subluminous (See also Figure 1.13).

1.3 Superluminous SNe Ia

SN1991T, discovered April 13, 1991 4:05 UT by Stephen Knight well before maximum light, exhibited an unusual early-time spectrum and bright maximum light.

1.3.1 Superluminous Light Curves

The peak brightness of the light curve of SN1991T exceeds that of "normally-luminous" SNe by at least 0.6 magnitudes at visual wavelengths (Filippenko et al., 1992). It also shows a slower rise and decline rate, creating the longer, broader light curve shown in Figure 1.7 from Filippenko et al. (1992). The decline rate in V was 0.052 ± 0.002 mag/day (Phillips et al., 1992), as compared to a normal decay of about 0.06 mag/day (Filippenko, 1997).

In fact, it turns out that all SNe Ia exhibit this relationship between peak magnitude and steepness of decline. Phillips (1993) suggested this be quantified in the term $\Delta m_{15}(B)$, which measures the "total amount in magnitudes that the light curve decays from its peak brightness" during 15 days. SN1991T has a $\Delta m_{15}(B) = 0.94 \pm 0.07$ (Phillips, 1993), whereas

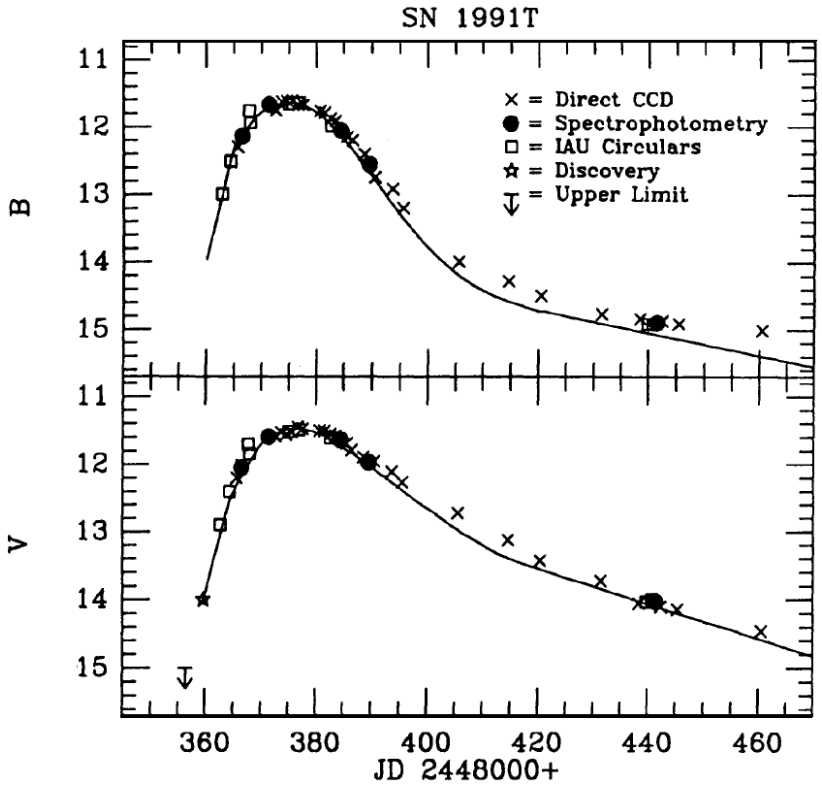

Figure 1.7 Taken from Phillips et al. (1992), the B and V light curves of superluminous SN Ia 1991T (symbols as marked) compared with normal SNe Ia templates (lines) from Leibundgut (1988). The templates are arbitrarily placed. SN1991T exhibits a broader light curve than normal SNe Ia, and (when plotted in terms of absolute magnitudes) is also much brighter.

normal SNe Ia typically have $1.1 \leq \Delta m_{15}(B) \leq 1.68$ (Mazzali et al., 2001; Lair et al., 2006). Woosley et al. (2007, for example) found that maximum luminosity is related to the amount of ^{56}Ni produced in the explosion. It looks as if SN1991T produced a mass of $1.0M_{\odot} \leq M \leq 1.4M_{\odot}$ of ^{56}Ni (Filippenko et al., 1992) as opposed to the normal $0.6M_{\odot} \leq M \leq 0.8M_{\odot}$ (Hoeflich and Khokhlov, 1996).

1.3.2 Superluminous Spectra

Early spectra of SN1991T show Fe lines (atypical of SNe Ia), and a lack of the typical IME absorption. They also indicate a higher expansion velocity than that of normal SNe Ia. Figure 1.8 compares the spectrum of SN1991T with those of two other normal SNe Ia taken at roughly a week before maximum light (Filippenko, 1997).

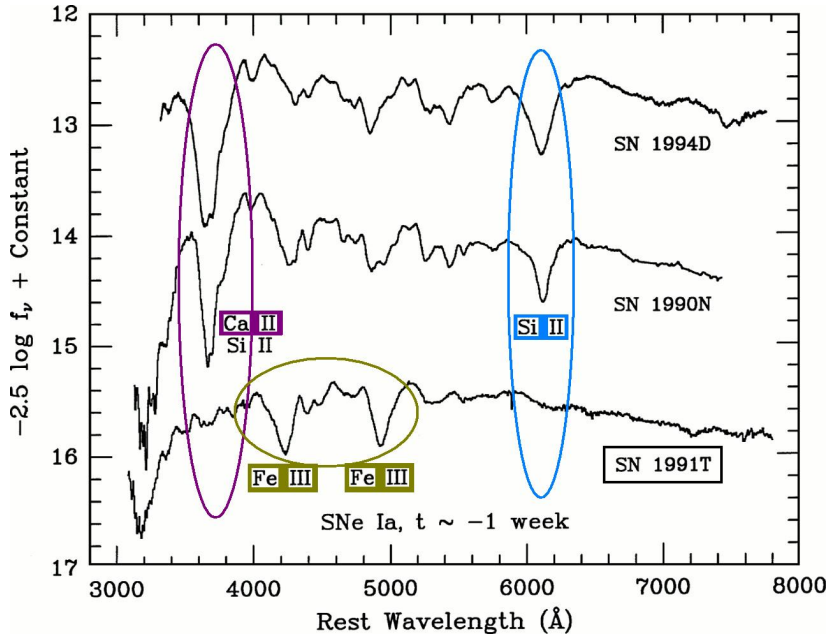

Figure 1.8 Reproduced from Filippenko (1997), the early spectra of SN1991T is compared against that of two SNe Ia (SN1994D & SN1990N). The Si and Ca lines, so pronounced in the top spectra, are missing in the SN1991T spectrum. Instead, Fe lines are prominent.

It is not until $t = 2$ days that the Si II lines (that phenomenologically define the SN as Type Ia) appear. Subsequent spectral comparisons, as in Figure 1.9 one week after maximum light, show IME lines developing (though weak). However, now the expansion velocity is the same as in normal spectra.

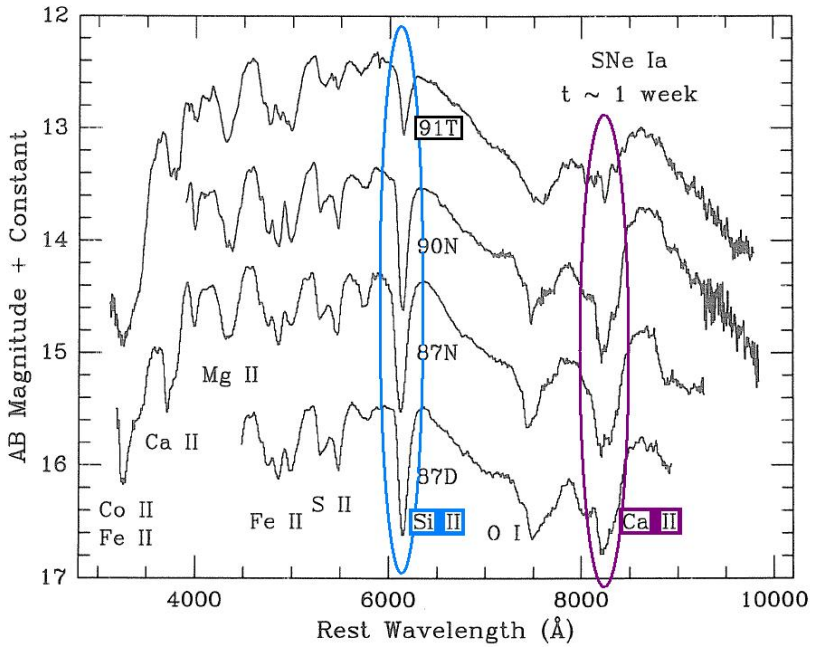

Figure 1.9 From Filippenko et al. (1992), a comparison of SN1991T with the SNe SN1990N, SN1987N, and SN1987D at a week past maximum light. IME lines appear, but aren't as strong as normal.

After 20 days, the spectrum is even closer to that of normal SNe Ia, but forbidden lines are emerging — indicating it has reached the nebular phase early. At 50 days, the spectra are practically identical, and now the Fe II lines dominate. These epochs are shown in Figure 1.10 from Filippenko et al. (1992).

Because spectra reveal the composition of deeper layers of the ejecta as time progresses, SN1991T's early spectrum indicates that iron peak elements are present in its outer

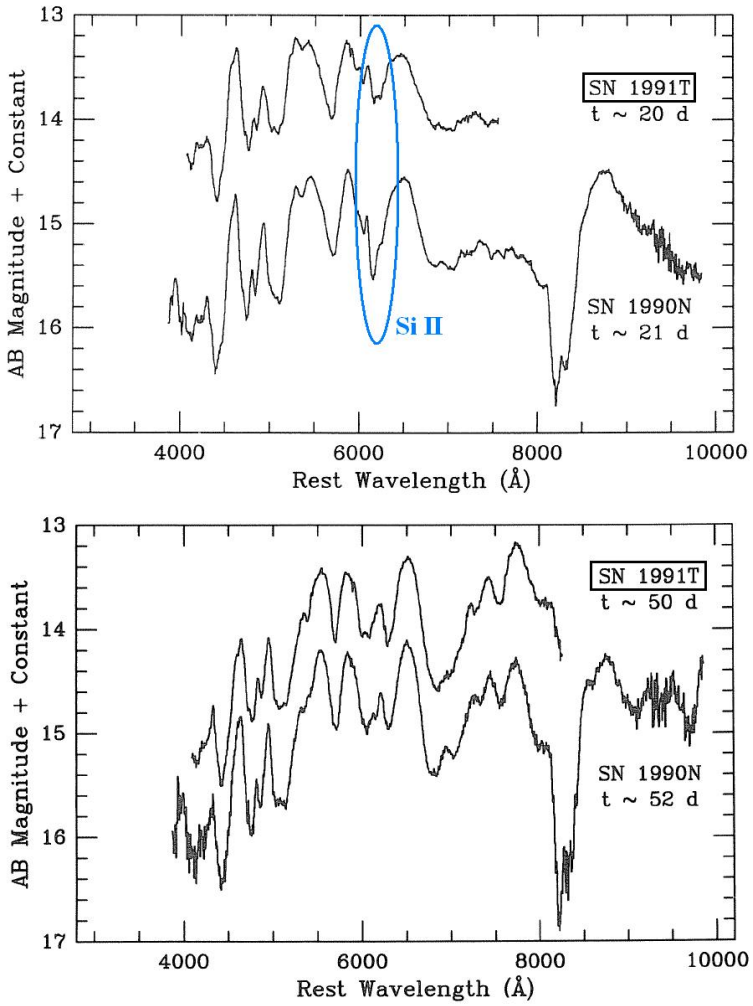

Figure 1.10 Reproduced from Filippenko et al. (1992), the spectra of SN1991T and more normal SN1990N at $t \sim 20$ days (top) and $t \sim 50$ days (bottom) after maximum light. At 20 days, the IME absorption features are present but not as strong, but at 50 days the spectrum from the two SNe are indistinguishable.

layers. The intermediate layers contain Si, S, and Ca, but deeper in the ejecta, the composition is again iron peak elements, indicating that while the central regions burned to complete NSE, the medial portions did not.

1.3.3 Possible Super-luminous Explosion Scenarios

Other SNe Ia were soon discovered that had the same characteristic broad light curves and unusual early spectra. It appears that there exists a (so-called "superluminous") subclass of SNe Ia stemming from a different explosion mechanism than that of the normally luminous SNe Ia.

One idea is that superluminous SNe undergo delayed detonation. An accreting WD ignites carbon at its center. The burning front propogates outward slowly, increasing in speed, but giving the ejecta time to expand. This is called a deflagration. As it reaches the density drop at outer layers, the burning front turns supersonic — transitioning into a detonation — and burns the surface C & O to heavy elements (Khokhlov, 1991).

This scenario synthesizes more ^{56}Ni than the single-degenerate Chandrasekhar-mass explosion model (Section 1.2) and also explains the production of iron peak elements in the core and surface, with IME in between. Thus it accounts for both the unusual brightness and chemical composition of superluminous SNe. However, if ^{56}Ni is synthesized in the outer layers, one might expect to see a different light curve shape. If the gamma rays from the decaying ^{56}Ni are deposited closer to the surface, the subsequent optical photons should take less time to escape — giving rise to a faster light curve rise time. However, Sn1991T and other bright SNe Ia exhibit a slow rise time.

Another proposed explosion scenario is that of a WD-WD merger (also known as a "double degenerate" model). As the two WD's orbit each other, the less massive one is disrupted and forms an accretion disk around the more massive one. The massive WD accretes a carbon envelope and ignition can occur either in the core of the more massive star, or at the contact surface (Hillebrandt and Niemeyer, 2000, and references therein). This scenario ensures that no H is present and perhaps produces greater amounts of ^{56}Ni. But problems with gravitational stability and accretion rates indicate that accretion induced

collapse (as talked about in Section 1.4.3) rather than thermonuclear explosion is much more likely to occur (Hillebrandt and Niemeyer, 2000, and references therein).

It is possible that the perfect combination of deflagration and delayed detonation reproduces the observed luminosity and chemical composition. However, results in section 2.4.4 show that large amounts of ^{56}Ni in outer layers of the ejecta cause the light curve to have a quick rise and decline time, when in fact, the opposite is observed in superluminous SNe. Thus, matching both chemical composition and luminosity behavior with a given model is difficult. Inhomogeneity in SNe light curves and spectra could perhaps be explained by variations in burning front propagations due to differing density or C-O composition in the WD progenitor, but exactly how, is not understood. It is worth noting that SNe belonging to this bright subclass seem to be found in young stellar populations (e.g. Branch et al., 1996).

1.4 Subluminous SNe Ia

Just as SN1991T exemplifies the superluminous class of SNe, SN1991bg is a well-observed example for subluminous SNe Ia. It, and others in this subclass (e.g. SN1992K, SN1986G, SN1992bo), appear much dimmer and fade more quickly than normal SNe Ia. They tend to be redder at maximum, and their spectra show an abundance of intermediate mass elements.

1.4.1 Subluminous Light Curve

The light curve of SN1991bg, reproduced in Figure 1.11 from Turatto et al. (1996), is the converse of SN1991T. It exhibits a fast decline of 0.117 mag/day in V and 0.146 mag/day in B (Turatto et al., 1996). With a maximum light of $\sim$ 2.5 mag fainter than normal SNe, it has a $\Delta m_{15}(B) = 1.88 \pm 0.10$ (Phillips, 1993). This low luminosity indicates that a smaller amount of ^{56}Ni was produced in the explosion — roughly $0.07 M_{\odot}$ (Mazzali et al., 1997). Also, the R light curve curiously did not possess the secondary maximum of typical SNe Ia (e.g., Figure 1.4).

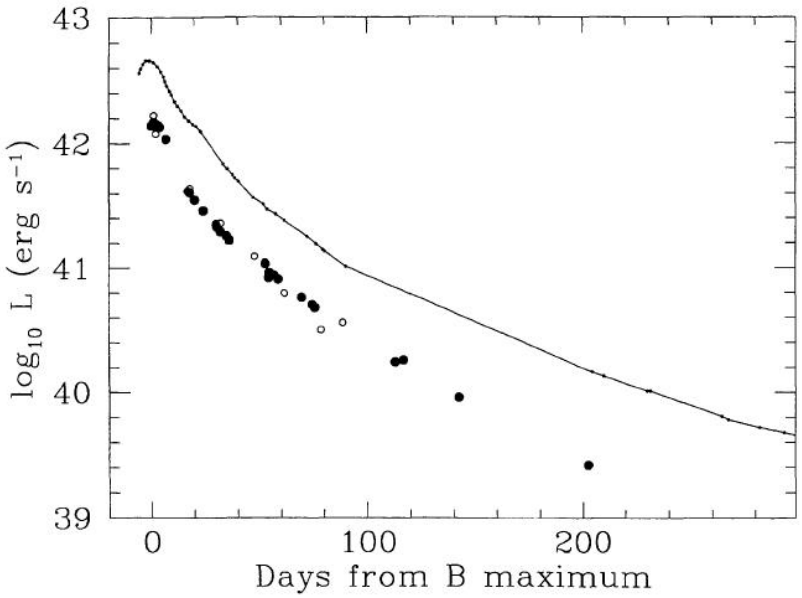

Figure 1.11 From Turatto et al. (1996), the bolometric (including *B, V, R, I* or flux calibrated spectra) light curve of SN1991bg (dots). The bolometric light curve of normally luminous SN1992A is plotted (solid line) for comparison. Note the dim maximum light, and steep decline of SN1991bg.

1.4.2 Subluminous Spectra

Figure 1.12 (from Turatto et al. (1996)) shows a progression of the spectrum of SN1991bg along with comparisons to normal SNe Ia. Early and late spectra are similar to those of normal SNe Ia, indicating that the photospheric and interior layers are under similar "normal" conditions. However, narrow absorption lines indicate a smaller expansion velocity than that of normal SNe Ia. At $t \sim 50$ days, the Ca II lines in SN 1991bg are much stronger than those seen in normal SNe spectra, showing incomplete NSE burning even in the intermediate layers. The evolution of Co III lines is again consistent with the idea that the decay chain of ^{56}Ni $\rightarrow$ ^{56}Co $\rightarrow$ ^{56}Fe powers the SN.

1.4.3 Possible Sub-luminous Explosion Scenarios

The smaller expansion velocity and lower production of ^{56}Ni may indicate the explosion occured before the accreting WD had a chance to reach the Chandrasekhar mass

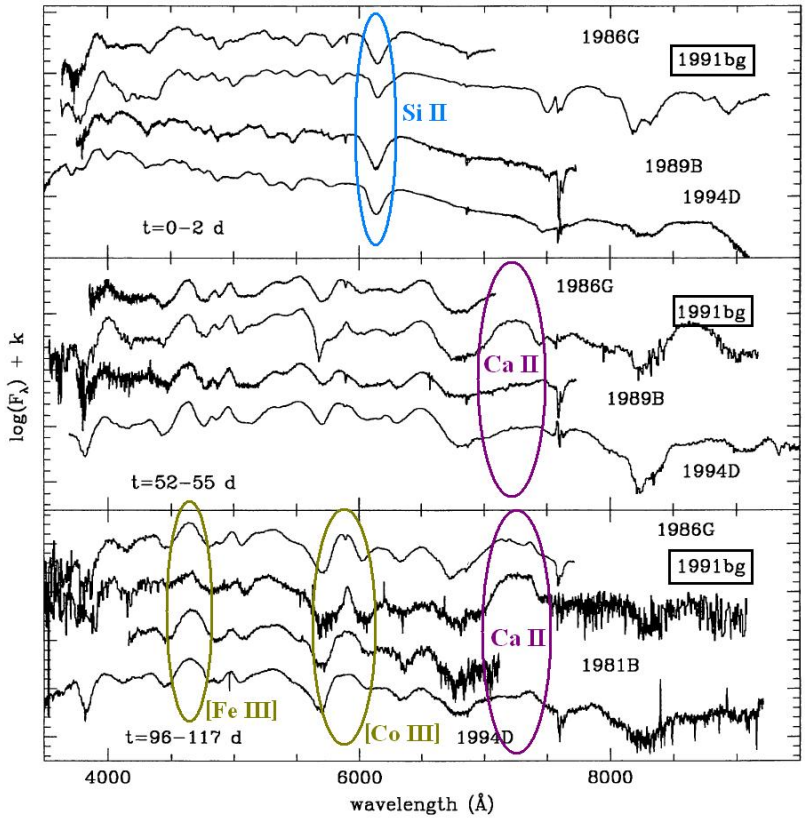

Figure 1.12 From Turatto et al. (1996), the progression of the spectrum of SN1991bg (second from the top in each frame) compared with normal SNe Ia SN1986G, SN1989B, & SN1994D. Both early and late spectra agree fairly well, but at $t \sim 50$ days, pronounced Ca II lines can be seen in SN1991bg.

limit. If its companion still has a helium/hydrogen shell, the WD will have accumulated an outer layer of helium. This layer can ignite and prompt a burning front that travels into the core, initiating thermonuclear explosion (Whelan and Iben, 1973). Possible problems with this route to explosion, based on accretion rates, can be found in Hillebrandt and Niemeyer (2000) and references therein. This "sub-Chandrasekhar-mass" scenario has progenitor mass varying from 0.65 to $1.1 M_{\odot}$ and produces an adequately small amount of ^{56}Ni. It seems to explain the observed characteristics of subluminous SN1991bg well, except for a predicted high-velocity outer layer of Ni and He, which is not seen in spectra (Nugent et al., 1997).

Another scenario that might explain subluminous SNe is not a thermonuclear explosion, but an "accretion induced collapse" of a WD. Instead of carbon core ignition, electron capture can lead to a collapse. Less mass is ejected and less ^{56}Ni is synthesized than in other scenarios.

1.5 Width-Luminosity Relation

It was the discovery of a phenomenological relationship between the peak light magnitude and luminosity decline rate in each SN that salvaged the use of SNe Ia as distance indicators. The relationship between the peak brightness and the width of the light curve around maximum can be parameterized by the decline rate (first introduced in Section 1.3.1), $\Delta m_{15}(B)$ as suggested by Phillips (1993), by a "stretch-factor" (Perlmutter et al., 1997), or by multi-parameter nonlinear fits (Riess et al., 1996). Plotted in the top frame of Figure 1.13 from Perlmutter (2003) are the light curves of nearby SNe. One can see an almost perfect sequence of nested progressively less luminous light curves. SN1991T is the most luminous and SN1991bg is the least. Simply by stretching the time scales by appropriate amounts, and renormalizing maximum light, these SNe fit the same light curve (bottom frame of Figure 1.13).

Now, as "standardizable candles," they continue to map out the fate of the universe. Their use, combined with results of the Wilkinson Microwave Anisotropy Probe (WMAP), led to a stunning realization — the universe is expanding at an accelerating rate. See Appendix A for more on the cosmological implications of SNe Ia. This profound conclusion

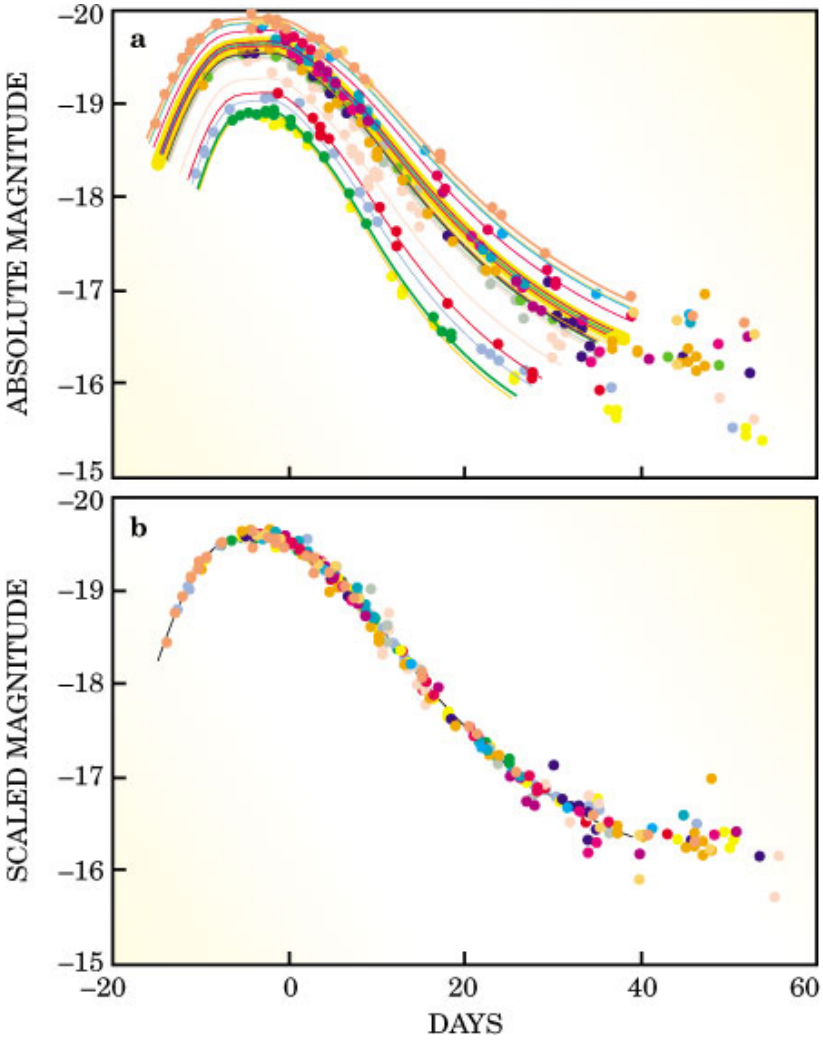

Figure 1.13 From Perlmutter (2003), the light curves of nearby SNe Ia. The top frame shows the nesting of light curves as each one has both a progressively decreasing luminosity, and decreasing width. The top light curve is that of SN1991T, while the bottom is that of SN1991bg. Most SNe Ia light curves fall neatly along the yellow band in the middle. By applying the appropriate stretch factor and renormalizing the point of maximum luminosity, each SNe can be made to fit the same light curve (bottom frame).

comes under the assumption that SNe Ia can be standardized and used as accurate distance indicators. In fact there are SNe Ia that do not follow the width-luminosity rule, e.g. SN2000cx (Li et al., 2001a) and SN2002cx (Li et al., 2003), showing that not all SNe are standardizable.

1.6 Late Times

Most observations of SNe Ia are made at early times or in the optical bands, where the SN is bright and easy to see. However, it is at late times, when the density of the ejecta is low enough that light from the center of the SN can escape.

1.6.1 Positron Deposition and Escape

At early times, all gamma rays from radioactive decays are deposited in the ejecta and their energies go towards powering the light curve. However, as the ejecta expands, more gamma rays escape. Though they deposit a minimal amount of energy on their way out, via compton scattering, most of their energy is lost. At later epochs, all gamma rays escape the ejecta, and it is only the deposition of the kinetic energy of positrons (from 3.5% of ^{56}Co decays) that powers the light curve. It is the nature of the magnetic field that determines how far positrons may travel before thermalizing or, at late times, what fraction of positrons escape the ejecta. Figure 1.14, reproduced from Milne et al. (2001), models the bolometric light curve of SNe Ia, showing the luminosity evolution for different assumptions of gamma ray and positron depositions. Note that beginning at $t \sim 500$ days, the light curve is steeper without positron deposition, because the energy that would be added to power the light curve instead escapes.

Magnetic Field Considerations

WDs (the progenitors of SNe Ia) have been observed to have magnetic fields of 3×10^5 to 10^9 G when alone or in non-interacting binary systems (Liebert, 1995). The magnetic fields of these WDs change very little over their lifetime. However, the magnetic field of an accreting WD may evolve if the accretion rate is larger than the rate of ohmic diffusion (the time scale during which the currents generating the magnetic field of a WD dissapate) (Cumming, 2004). An accretion rate greater than 1 to 5×10^{-10} $M_\odot$/yr may reduce the

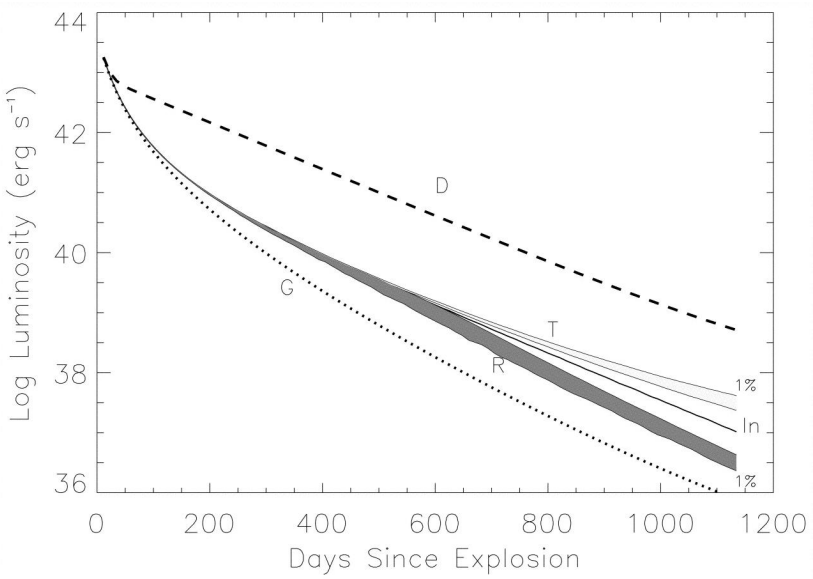

Figure 1.14 From Milne et al. (2001), predicted bolometric light curves assuming instantaneous deposition of all decay energy (dashed line D), gamma-ray deposition accounting for escape due to late-time diffuse ejecta (dotted line G), and gamma-ray deposition with varying degrees of positron deposition (middle lines R through T). The dark band (R) shows the range of curves for a radial field configuration, the light band (T) is the range for a trapping field, while the line in-between (labeled In)is the curve for instantaneous in-situ deposition of positron energy. Ranges correspond to different ionization fractions of the ejecta.

surface magnetic field. Also, accreting WDs have been observed to have magnetic fields of 7×10^6 to 3×10^8 G (Cumming, 2004). *Both* the non-interacting and accreting WDs usually have complex (non-dipolar) fields. In fact Reinsch et al. (2004) found that the field is more complex than a 5-component multipole expansion.

It is uncertain what effect the SN explosion has on the magnetic field lines. However, Ruiz-Lapuente and Spruit (1998) suggest 3 possible magnetic field configurations at late times. First, the field may not be strong enough to contain the positrons, in which case, the positrons travel in free trajectories (straight-lines), and some portion escape the now transparent ejecta. Second, the ejecta of a SN could drag the field lines (of any original dipole magnetic field — or perhaps even an aribitrarily complicated field)) along as it homologously expands, leaving the field radially-combed (Colgate et al., 1980). Positrons spiral along magnetic field lines while their pitch angle (the angle between the magnetic field lines and the particle's velocity) changes to encourage a radially outward trajectory and, thus, escape (Chan and Lingenfelter, 1993). Milne et al. (1999) discovered, through modeling, that positrons in the weak field and those in the radially-combed field travel the same mean path to freedom from the ejecta. In the third configuration, the magnetic field is strong and turbulently disordered with lines tangled, perhaps from the "violent explosion" of the SN (Axelrod, 1980). Here, the positron mirrors frequently, but does not leave the mass coordinate of its birth, and is trapped in the ejecta.

The positrons that do not escape the ejecta will likely thermalize (though not all trapped positrons do) and donate their energy to the SN luminosity. Milne et al. (2001) compared the light curves of SNe Ia with models of different magnetic field configurations. Shown in Figure 1.15 are the V-band light curves of 22 SNe Ia fitted to the model DD23C (a delayed-detonation Chandrasekhar-mass model). The gray band (R) is the bolometric light curve of the radially-combed magnetic field model (and equivalently of the weak magnetic field), where positrons escape radially. The darker band (T) is the bolometric light curve characterizing the turbulently disorded magnetic field scenario, where the positrons meander a bit, but are ultimately trapped). These scenarios are also plotted in Figure 1.14 but calculated for the model HED8.

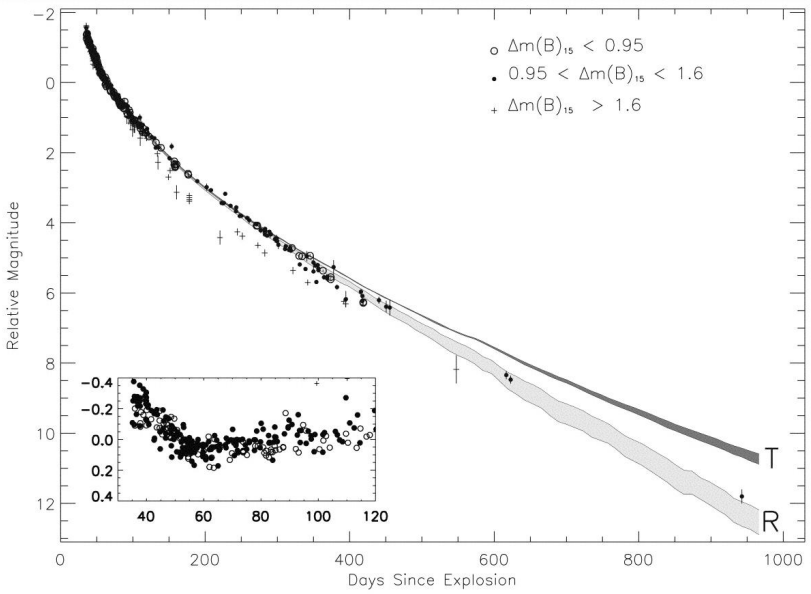

Figure 1.15 From Milne et al. (2001), V-band light curves of 22 SNe Ia (subluminous are open circles, normally luminous are filled circles, and subluminous are crosses) compared with delayed-detonation Chandrasekhar-mass model DD23C for trapped positrons (dark band T), and for radially escaping positrons (light band R).

The super-luminous (open circles) and normally luminous (filled circles) SNe light curves seem to evolve similarly at late times, and are better fitted by the radially escaping positron model. However, the sub-luminous SNe (crosses) are distinct in their evolution, and seem less energetic than the delayed-detonation Chandrasekhar-mass model even without positron deposition. It would appear that the positrons escape through either a radially-combed or weak magnetic field. We can also calculate the total number of positrons that escape from a SN Ia, as Milne et al. (1999) does, to be $8 \times 10^{52}\ e^{+}/SN$. These conclusions rest on the assumption that the V-band scales with the total luminosity, and there is little to no color evolution. Milne et al. (1999) argue from $BVRI$ observations of SNe that color evolution is minimal after 175 days.

1.6.2 The Importance of the Infrared

Axelrod (1980) suggests that at late epochs there may be a significant shift in emission to the *IR*. Because the rate of collisions in the ejecta is fast relative to radiative transitions, thermal emissions dominate. At early times, the thermal ejecta is hot and emissions are mainly in the optical bands, however at later times, the ejecta has cooled, and the emission in the *IR* becomes more important. At low temperatures, optical atomic levels aren't excited, and the fine structure transitions of iron dominate emission. Axelrod (1980) suggests that all emission will shift quickly to the far-IR, which cannot currently be observed. This instability is termed the infrared catastrophe. Though, late observations have not yet seen a *sudden* drop at visual magnitudes to suggest the infrared catastrophe occurs, one can see evidence that the emission shifts (if gradually) to longer wavelengths.

1.6.3 Previous Late Infrared Observations

While observing seven normally luminous and superluminous SNe Ia, Lair et al. (2006) found that while the B, V, and R bands declined at 1.4 mag per 100 days at epochs of 200-500 days, the I decline rate was shallower at 0.94 mag per 100 days. Only a handful of SNe Ia have been observed at late times in the near-*IR*. Sollerman et al. (2004) observed SN2000cx in the *UVOIR* up to 480 days past maximum. In observations between 360 and 480 days past maximum, the optical light curves continually declined by about 1.4 mag per 100 days, the I-band light curve only declined by .8 mag per 100 days, and the J,H-band light curves were actually increasing in magnitude! The light curve of combined *UVOIR* bands is shown in Figure 1.16.

The dot-dashed line is Sollerman et al. (2004)'s model for the contribution from deposited gamma rays, and the dashed line is the contribution from positrons. The light curve of SN2000cx (diamonds) seems to indicate that the positrons are trapped. The cause for the difference in positron deposition conclusions between Sollerman et al. (2004) and Milne et al. (2001) is the inclusion of the contribution of the increasingly important near-*IR*. The V-band follows the steeper slope consistent with positron escape, the bolometric light curve is shallower suggesting positron energy is deposited in the ejecta. It seems that the color evolution is such that it mimics the effect of positron escape in the *BVRI*.

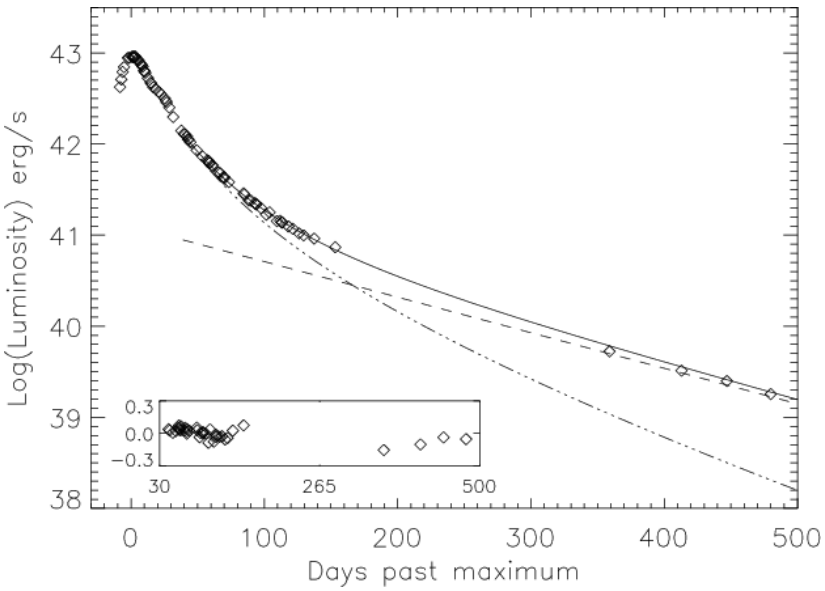

Figure 1.16 From Sollerman et al. (2004), the (*UVOIR*) light curve of SN2000cx (diamonds) plotted against a model of ^{56}Co decay (solid line). The dot-dashed line shows the contribution from gamma rays, and the dashed line is the contribution from the positrons assuming all energy is deposited in the ejecta. The fit of SN2000cx seems to indicate positron trapping is occurring.

SN2001el, a normal SN Ia, was also observed to have a significant contribution from the near-*IR* (Stritzinger and Sollerman, 2007). From 310 to 445 days, the percentage of flux from the *JHK* bands increased from 6% to 25%. The decline rate of Stritzinger and Sollerman (2007)'s *UVOIR* light curve indicates the majority of positrons are deposited in the ejecta, favoring a trapping magnetic field configuration. SN2004S exhibits practically identical characteristics to SN2001el, widening our pool of late *IR* observations. Though there has not yet been observed a significant decrease in the late *B*, *V* light curves indicating the beginning of the infrared catastrophe, there is no doubt that important energy information is contained in the near-*IR* at late times.

1.7 Unanswered Questions

Though these observations suggest a trapping magnetic field, it is not clear that this is the case. Models must be refined and more late *IR* observations increased before the

problem of positron escape can be addressed with certitude. There are also a number of other unanswered questions.

Observations of SN2000cx, SN2001el, and SN2004S agreed very well, but it appears they are all normal SNe. As seen in Figure 1.15, even the optical light curve of subluminous SNe Ia behave drastically differently than their normal and super-luminous counterparts. How do bolometric late light curves (ones that include at least B, V, R, I, J, H, K) of subluminous SNe stack up against the other subclasses? Perhaps there is a hint to the difference in progenitor for each class buried in late light curves (where, after all, the observed light is coming from the center of the ejecta).

We have also not seen the total evolution of the late *IR* luminosity. At what point does the increase stop, and start declining again. If the near-*IR* does not fall as the ^{56}Co decay, there must be another power source. Extensive studies of SNe Ia of different luminosity classes at late times in the *IR* must be done.

In this thesis we seek to understand the processes SNe Ia undergo to produce their perhaps "standardizable" luminosity.

CHAPTER 2

MODELING

SNe Ia are complex beasts, and though attempts to model a SN Ia have been undertaken at certain epochs (see Hillebrandt and Niemeyer, 2000, and references therein), no one has modeled a SN all the way from conception to very late times. In this thesis, we will model, in a very simple way, the early time physics of SNe Ia. The goal is to reproduce and understand the overall behavior of a light curve at this epoch, and contrast it with the late time behavior.

2.1 Nuclear Energy

As the WD undergoes nuclear burning, energy is released when carbon and oxygen are burned to IME or iron-peak elements. One can estimate the amount of energy by considering the chemical make-up of the white dwarf and of the ejecta. The nuclear energy released is the difference of the sum of the binding energy (BE) of all nucleons before (b) and after (a) the explosion:

$$\mathrm{E} = \sum_i N_i^b \mathrm{BE}_i - \sum_i N_i^a \mathrm{BE}_i, \tag{2.1}$$

where N_i is the number of nuclei of type i, and the sum is taken of each type of nuclei present. Most of the nuclear energy released comes from the transformation of C and O into IME like Si and S. For a 1.4 $M_\odot$ (Chandrasekhar) WD of equal parts carbon and oxygen, whose resulting ejecta is composed of .6 $M_\odot$ of ^{56}Ni, .3 $M_\odot$ of ^{28}Si, .25 $M_\odot$ of ^{12}C, and .25 $M_\odot$ of ^{16}O, the energy released is

$$\mathrm{E} = 1.324 \times 10^{51} \mathrm{ergs}. \tag{2.2}$$

Some of this energy goes into lifting the WD out of its own gravitational potential well — blowing apart the WD. Gravitational potential energy is

$$U = -\frac{G m_1 m_2}{r}, \tag{2.3}$$

where G is the gravitational constant, m_1 and m_2 are interacting masses, and r is the distance between them. Integrating over the whole WD in layers of concentric shells with m_1 as the mass of the shell $\left(4\pi r^2 \rho dr\right)$ and m_2 as the mass interior to the shell $\left(4/3\pi r^3 \rho\right)$ yields

$$U = -\int_0^R \frac{16}{3} G\pi^2 \rho^2 r^4 dr, \tag{2.4}$$

where ρ is the density of the material. Assuming ρ is constant with radius r,

$$U = -\frac{3GM^2}{5r}. \tag{2.5}$$

A Chandrasekhar WD, at 1.4 $M_\odot$, has a gravitational potential energy of

$$U = -3.104 \times 10^{50} \text{ergs}, \tag{2.6}$$

and a net energy ($E_{net} = E + U$) of

$$E_{net} = 1.013 \times 10^{51} \text{ergs} = 1.013 \text{ foes}. \tag{2.7}$$

Observations of the ejecta of SNe indicate a kinetic energy of ~ 1 foe, which, within uncertainties, accounts for the rest of the nuclear energy.

2.2 Decay

Thus, the energy needed for the prolonged luminosity must be generated elsewhere. It comes from the radioactive decay of ^{56}Ni, which was synthesized in the nuclear explosion. ^{56}Ni decays to ^{56}Co which then decays to ^{56}Fe. These produce gamma rays and positrons (as described in equations 1.5–1.9 and surrounding text), which may deposit their energy in the ejecta. Without this additional energy, the SN would fade as quickly as it brightened. One can determine the amount and evolution of the power generated from radioactive decay.

The numbers of atoms of ^{56}Ni, ^{56}Co, and ^{56}Fe over time are given by

$$N_{\rm Ni}(t) = N_{\rm Ni0} e^{-\frac{t}{\tau_{\rm Ni}}} \tag{2.8}$$

$$N_{\rm Co}(t) = N_{\rm Ni0} \frac{\tau_{\rm Co}}{\tau_{\rm Co} - \tau_{\rm Ni}} \left(e^{-\frac{t}{\tau_{\rm Co}}} - e^{-\frac{t}{\tau_{\rm Ni}}} \right) \tag{2.9}$$

$$N_{\rm Fe}(t) = N_{\rm Ni0} \left(1 + \frac{\tau_{\rm Ni}}{\tau_{\rm Co} - \tau_{\rm Ni}} e^{-\frac{t}{\tau_{\rm Ni}}} - \frac{\tau_{\rm Co}}{\tau_{\rm Co} - \tau_{\rm Ni}} e^{-\frac{t}{\tau_{\rm Co}}} \right), \tag{2.10}$$

and the rate of decays by

$$\frac{dN_{\rm Ni}}{dt}(t) = \frac{N_{\rm Ni0}}{\tau_{\rm Ni}} e^{-\frac{t}{\tau_{\rm Ni}}} \tag{2.11}$$

$$\frac{dN_{\rm Co}}{dt}(t) = \frac{N_{\rm Ni0}}{\tau_{\rm Co}} \frac{\tau_{\rm Co}}{\tau_{\rm Co} - \tau_{\rm Ni}} \left(e^{-\frac{t}{\tau_{\rm Co}}} - e^{-\frac{t}{\tau_{\rm Ni}}} \right), \tag{2.12}$$

where, $N_{\rm Ni0}$ is the initial number of ^{56}Ni atoms, $\tau_{\rm Ni} = 5.5$ days is the lifetime of ^{56}Ni, and $\tau_{\rm Co} = 111.3$ days is the lifetime of ^{56}Co (Nadyozhin, 1994).

For ejecta containing 0.6 $M_\odot$ of ^{56}Ni, the number of each element can be seen in Figure 2.1.

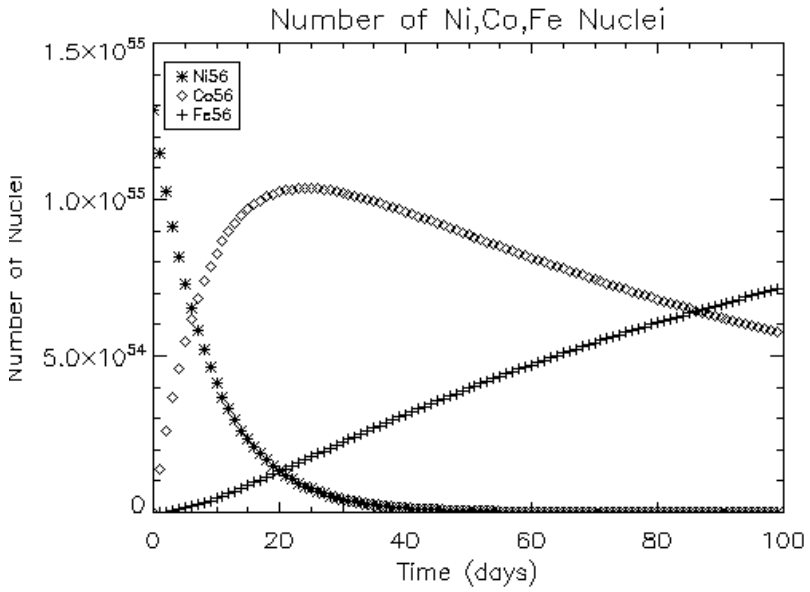

Figure 2.1 Number of nuclei of ^{56}Ni (star), ^{56}Co (diamonds), and ^{56}Fe (crosses) in the ejecta. Notice that the number of ^{56}Co increases as the number of ^{56}Ni decays, and as ^{56}Co decays, ^{56}Fe numbers increase.

Multiplying the rate of decay by the average total energy released in gamma rays and/or positron per decay gives the energy released at a certain time. The time evolution is plotted in Figure 2.2. Initially the dominant contribution of power comes from ^{56}Ni decay, but at 35 days, the total power begins to trace the ^{56}Co decay. Overall, the power

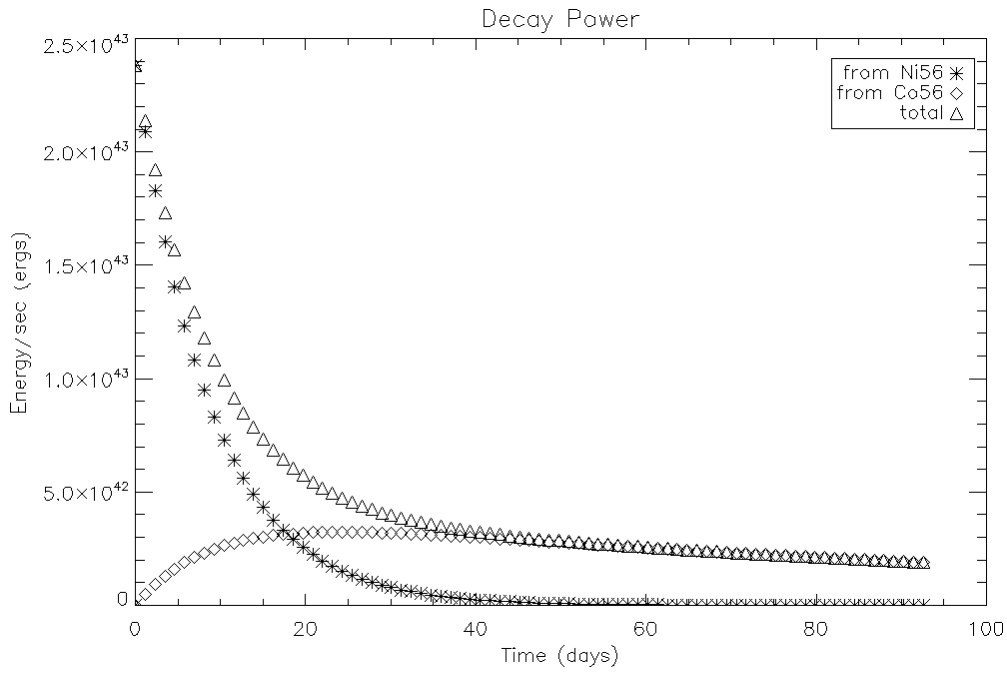

Figure 2.2 Energy from the decays of ^{56}Ni (star), ^{56}Co (diamonds), and total energy (triangles) at a given time. The total energy released from decays declines as there are fewer and fewer radioactive nuclei left to decay.

decreases, steeply at first, but much more gradually as the 111 day lifetime of ^{56}Co becomes important. Though Figure 2.2 shows the total power available to the ejecta, it does not have the familiar shape of the light curves of SNe Ia in Figures 1.2 and 1.4. This is because the energy takes some time to "diffuse" from its place of production to its escape from the ejecta. Among other factors, this diffusion time depends on where in the SN ^{56}Ni is produced, and how dense the ejecta is. As the ejecta expands, the density decreases, and the diffusion time is itself a function of time. A model is needed to see exactly how the light curve shapes up.

2.3 Expansion

Our model begins after the nuclear burning has occurred, so that the expanding ejecta already contain some radioactive ^{56}Ni. The ejecta are divided up into four spherical shells (shown in Figure 2.3), allowing one to assign different values of expansion velocity,

chemical make-up, and thus opacity to each shell according to depth. The initial radius to

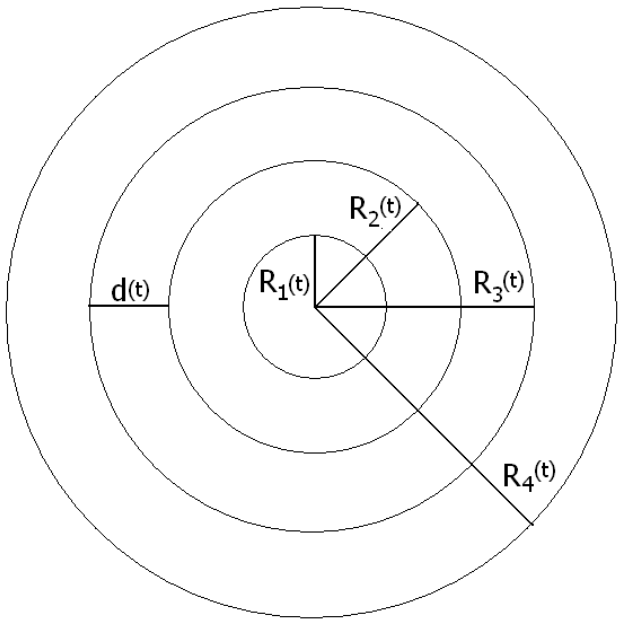

Figure 2.3 The model divides the ejecta into 4 concentric spherical shells each with a different radius and expansion velocity as well as its own chemical make-up. The distance between shells, $d(t)$, though a function of time, is the same for each shell. Shells are numbered so that 1 is the central sphere, and 4 is the outer shell.

the outer edge of each shell is

$$R_n(t=0) = \frac{n}{4} R_4(0), \tag{2.13}$$

where n is the number of the layer in question and $R_4(0) = 10^9$ cm is the inital radius of the outer shell. n ranges from from 1 to 4 — the smaller number indicating closer proximity to the center of the ejecta. The ejecta is expanding homologously, meaning the outer layers of the ejecta expand faster than the inner. To simulate this, each shell is assigned an expansion velocity,

$$V_n = \frac{n}{4} V_4, \tag{2.14}$$

where V_4, the velocity of the outer shell, is 10^9 cm/s. The outer radius of the expanding shell (shown in Figure 2.3) is thus

$$R_n(t) = \frac{n}{4}\left(R_4(0) + V_4 t\right), \tag{2.15}$$

and the distance from the inner edge of a shell to the outer edge is the same for each shell:

$$d_n(t) = \frac{R_4(0) + V_4 t}{4} = d(t), \tag{2.16}$$

where t is time in seconds. However, the volume still differs:

$$\mathrm{Vol}_n(t) = \frac{4\pi}{3}\left(\frac{R_4(0) + V_4 t}{4}\right)^3 \left[n^3 - (n-1)^3\right], \tag{2.17}$$

We assume there is no mass transport from shell to shell — only energy is transferred. Though the radius steadily increases, the mass remains constant and the density decreases.

2.4 Early Times

At early times, the ejecta is thick, and the gamma rays deposit their energy *in situ*. For this epoch, the model focuses on the diffusion of energy through the expanding shells. However, at later times, our assumptions of energy deposition and propogation become less accurate (see section 2.5.1), neccesitating a very different approach.

2.4.1 Diffusion Time

The time it takes for the energy to diffuse to an outer layer depends on the density of the nearby ejecta. The mean free path — how far a photon can travel before collision and a change in direction occurrs — can be found from the opacity and density as:

$$l = \frac{1}{\kappa\rho}. \tag{2.18}$$

If we assume all the energy begins at the back of the shell, the photon has to travel the distance $d(t)$ before it reaches the next shell. This distance can be quantified as the number of mean free paths, $d = \tau l$. However, in a random walk, it takes τ^2 steps to actually traverse this distance. So, the photon travels a total distance $\tau^2 l$ at the speed of light, c, in a time:

$$t^{\mathrm{diff}} = \frac{\tau^2 l}{c}. \tag{2.19}$$

We take this to be the diffusion time for a photon to escape from a goven shell to an outer one. In addition to being the number of mean free paths in the distance d, $\tau = d\kappa\rho$ is also known as the optical depth. Thus, for a given shell n,

$$t_n^{\text{diff}}(t) = \frac{d^2(t)\kappa_n(t)\rho_n(t)}{c}. \tag{2.20}$$

2.4.2 Opacity

At early times, all gamma rays are thermalized as described in section 2.5.1, thus we consider transport of thermal photons. While the true opacity is dependent on the spectrum of propagating photons and is a complicated function of absorption and re-emission in each wavelength, one may look at a frequency averaged $\langle\kappa\rangle$ to get an approximation.

The dominant source of opacity for thermal photons is free-free absorption (thermal bremsstrahlung). This occurs as an electron moving in the field of an ion absorbs a photon. From Clayton (1983), the free-free opacity is

$$\kappa_{ff}(\nu) = \sum_i \frac{X_i N_i}{A_i} \overline{\sigma}_{ff}(Z_i, \nu), \tag{2.21}$$

where the sum is taken over all elements present, X_i is the mass fraction of element i, A_i is the atomic mass, and the free-free cross section for photons of frequency ν is

$$\overline{\sigma}_{ff} = 3.69 \times 10^8 \frac{Z^2 n_e \overline{g}_{ff}}{T^{\frac{1}{2}}\nu^3} \text{ cm}^2. \tag{2.22}$$

n_e is the electron number density, T is temperature, and $\overline{g}_{ff}$ is the temperature averaged gaunt factor, which is unity for most astrophysical circumstances. Taking the Rosseland mean (a weighted average over frequency) of just the free-free opacity, yields

$$\langle\kappa_{ff}\rangle = 0.125 \frac{n_e}{T^{3.5}} \sum_i \frac{Z_i^2 X_i}{A_i} \text{ cm}^2/\text{g}. \tag{2.23}$$

Unfortunately, this evaluates to too small a value to generate the correct light curves. Instead of causing the early-generated-energy to build up and escape at some later timestep, the small opacity permits escape immediately after deposition. In the end, it was simpler to vary the opacity as a free parameter until the delay of escaping energy corresponded to

a light curve peak at ~ 20 days (see Figure 2.4). The suitable value was 0.2 cm^2/g and is taken to be constant across all shells and all times.

For perspective, the opacity of the central regions of the sun is 0.4 cm^2/g. This region of completely ionized hydrogen differs from a SN's mixture of singly ionized Fe, Ni, Co, Si, S, Ca, C, O. If the sun's opacity is predominantly due to free-free absorption,

$$\kappa_\odot \propto N_\odot^{free-e}, \tag{2.24}$$

where $N_\odot^{free-e} = N_A$ is the number of free electrons per gram, and $N_A = 6.022 \times 10^{23}$ is Avogadro's number. However, the number of free electrons per gram in the SN ejecta is

$$N_{SN}^{free-e} = \sum_i \frac{Z_i}{A_i} X_i f_i N_A, \tag{2.25}$$

where f_i is the ionization fraction (take singly ionized Si for an average: $f_{Si} = \frac{1}{14}$), and $\frac{Z_i}{A_i} \sim \frac{1}{2}$. Applied to the sun's opacity,

$$\kappa_{SN} \sim \frac{1}{14}\frac{1}{2}\kappa_\odot = 0.014. \tag{2.26}$$

The value chosen in our model is about that of completely ionized carbon and oxygen.

2.4.3 Energy

The energy over time is tracked for each shell. It may be altered by the deposit of energy from a ^{56}Ni or ^{56}Co decay, by the loss/escape of energy as photons propogate outward over some diffusion time, or by the addition of energy as photons arrive from an interior shell. Thus the equation for the change in energy for the n^{th} shell over one time step, Δt, is:

$$\Delta E_n(t) = \left(E_{Ni}\frac{dN_{Ni}}{dt}(t) + E_{Co}\frac{dN_{Co}}{dt}(t) - \frac{E_n(t)}{t_n^{\text{diff}}(t)} + \frac{E_{n-1}(t)}{t_{n-1}^{\text{diff}}(t)} \right) \Delta t, \tag{2.27}$$

where $\frac{dN_{Ni}}{dt}(t)$ and $\frac{dN_{Co}}{dt}(t)$ are the rates of decay of Ni and Co respectively at time t, $E_{Ni} = 1.75$ MeV and $E_{Co} = 3.73$ MeV are the respective average energies released (including gamma rays and positrons) per decay. $E_n(t)$ and $E_{n-1}(t)$ are the total energies contained in shell n and n-1 respectively at time t, while $t_n^{\text{diff}}(t)$ and $t_{n-1}^{\text{diff}}(t)$ are the respective diffusion times. In this model, the energy only propagates outward — there is no contribution from

exterior shells. The energy escaping from the fourth shell should portray the same behavior as an observed bolometric SNe Ia light curve.

2.4.4 Results

The generated light curve is shown in Figure 2.4, along with the power deposited by decay from Figure 2.2. The delay in escape is evident at early times, though at late times the escaping power converges with that deposited. This evolution is due to the decreasing diffusion time $t^{\rm diff}(t)$ which follows the decreasing density. By our assumption of instant and total deposition, all decay power goes into the light curve. Therefore, the area under each curve shold be equal.

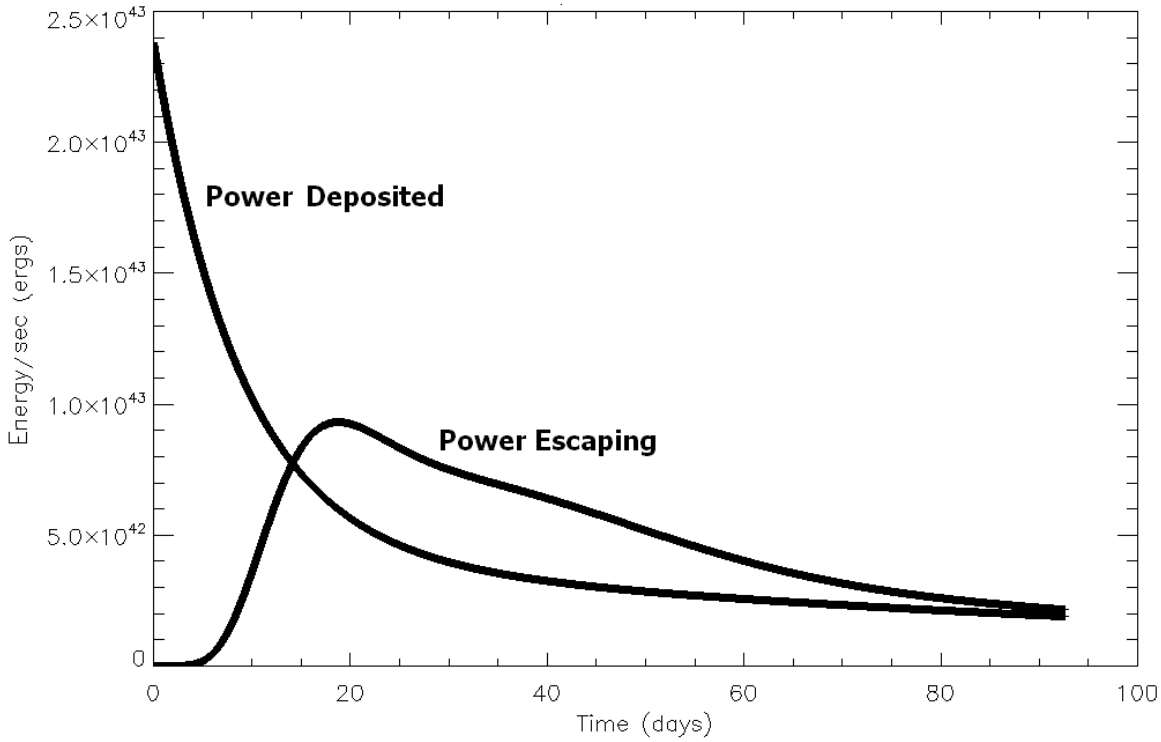

Figure 2.4 The light curve generated from our model of a SN ejecta plotted with the energy deposited by decay. The escape of the deposited energy is delayed at early times by the dense ejecta, but as the ejecta thins, more energy may escape in a small diffusion time $t^{\rm diff}(t)$. Notice that the light curve peaks at ~ 20 days as determined by our choice of κ.

There is an almost imperceptible bump in the light curve around 50 days. This is probably not a physical manifestation, but rather a result of the coarse resolution of the ejecta. It is likely caused by a sharp opacity decrease for an inner shell, releasing some built up power. With a higher resolution — a larger number of shells, the light curve should smooth out. Even with only four shells, our attempt to generate the features of a SN Ia is successful. Figure 2.5 compares our light curve with a number of observed "bolometric" light curves from Contardo et al. (2000). The model light curve has a generally similar

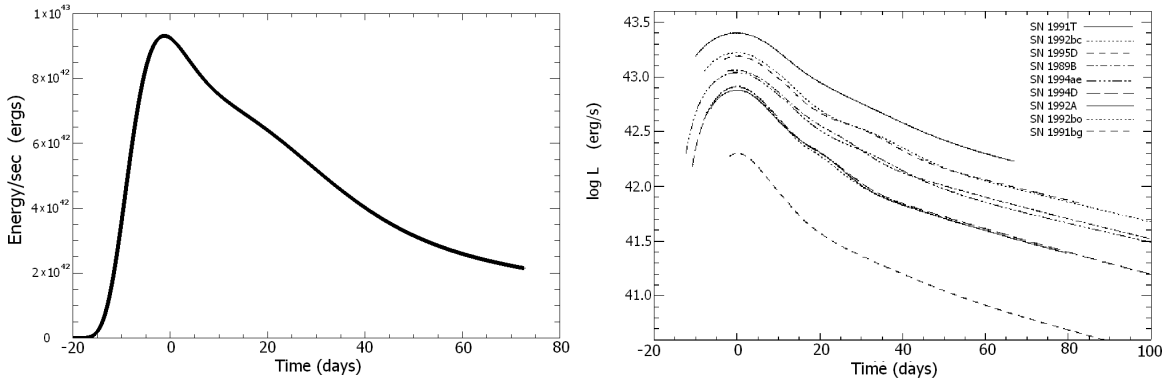

Figure 2.5 The light curve generated from our model (left) and the bolometric (U, B, V, R, I bands) light curves of a number of observed SNe Ia from Contardo et al. (2000) (right) plotted for comparison. The overall shapes are similar, though the observed light curves tend to be smoother. The peak shape tends to span about 20 days in both modeled and observed.

shape to the observations, although the bolometric SNe light curves seem more smooth and rounded. Perhaps this mismatch is again due to the low resolution of the simple model. The peak rise and decline time takes overall 20 days for the model, as well for the normally luminous SNe.

The simple model allows the initial chemical make-up of each shell to be specified so that the radioactive ^{56}Ni may be placed at different depths. This allows one to examine the effects of various product placements suggested by burning scenarios like those mentioned in sections 1.3.3 and 1.4.3. Figure 2.6 contrasts the light curve of a model with ^{56}Ni at the

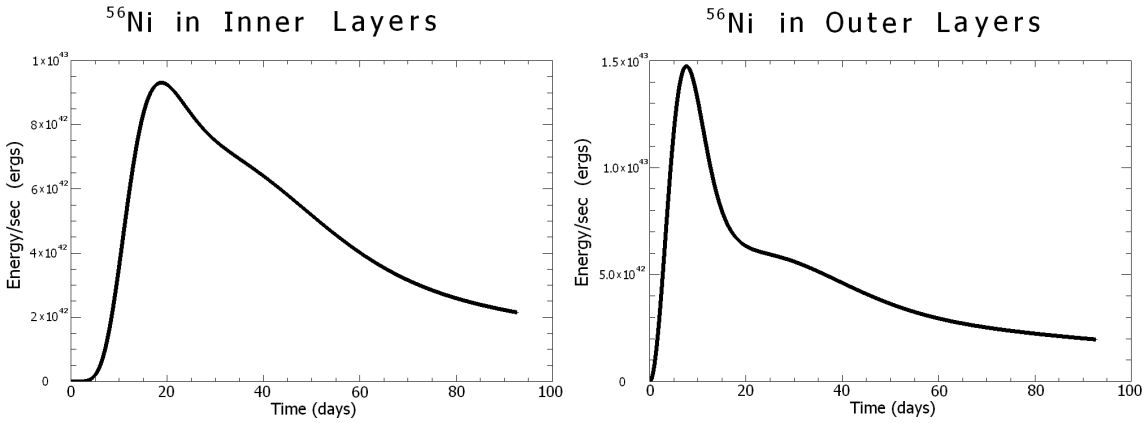

Figure 2.6 The light curve generated from a model with ^{56}Ni in the inner shell (left), and from a model with ^{56}Ni in both the inner and outer shells (right). Notice the light curve peaks sooner and at higher energies for the model with ^{56}Ni in the outer layer than that of the model with ^{56}Ni in only the inner shell, though at later times less energy is escaping.

center and of a model with ^{56}Ni in both the center and outer layers. The light curve peaks earlier (at $\sim$ 15 days) and at higher energies for the model with ^{56}Ni in the outer layers than does the light curve of ^{56}Ni in only the center, which peaks at $\sim$ 20 days. This is as one might expect. The deposited energy in the outer layers needs only diffuse through one layer (the least dense) in order to escape, while in the other scenario, the energy must traverse the entire ejecta. Consequently, more energy is able to escape more quickly in the former, building to an early and powerful peak light, However, because much of the energy escapes early, there is less left over for later times,causing the light curve to dim more steeply at 25 days than that of the other scenario. Light curves like the one on the left in Figure 2.6 are not observed — in fact, (as discussed in section 1.5) light curves of brighter peak light typically exhibit a slower decline than their dimmer counterparts.

The timing of maximum light and shape of the light curve depend on the placement of radioactivity, but these characteristics are also sensitive to the amount of ^{56}Ni present in the ejecta. This abundance is suggested to be the variable that determines whether a SN appears super or sub-luminous. We can test what effect varied amounts of ^{56}Ni have on the model light curve. Shown in Figure 2.7 is the light curve of a SN with 1 $M_\odot$ of ^{56}Ni — the

amount suggested to have been synthesized in SN1991T. Figure 2.8 shows a SN light curve with 0.07 $M_\odot$ which is the lowest amount of ^{56}Ni SN1991bg is suggested to have produced (Mazzali et al., 1997). The peak light occurs at an early 15 days and a $\sim 1.6 \times 10^{45}$ ergs/s

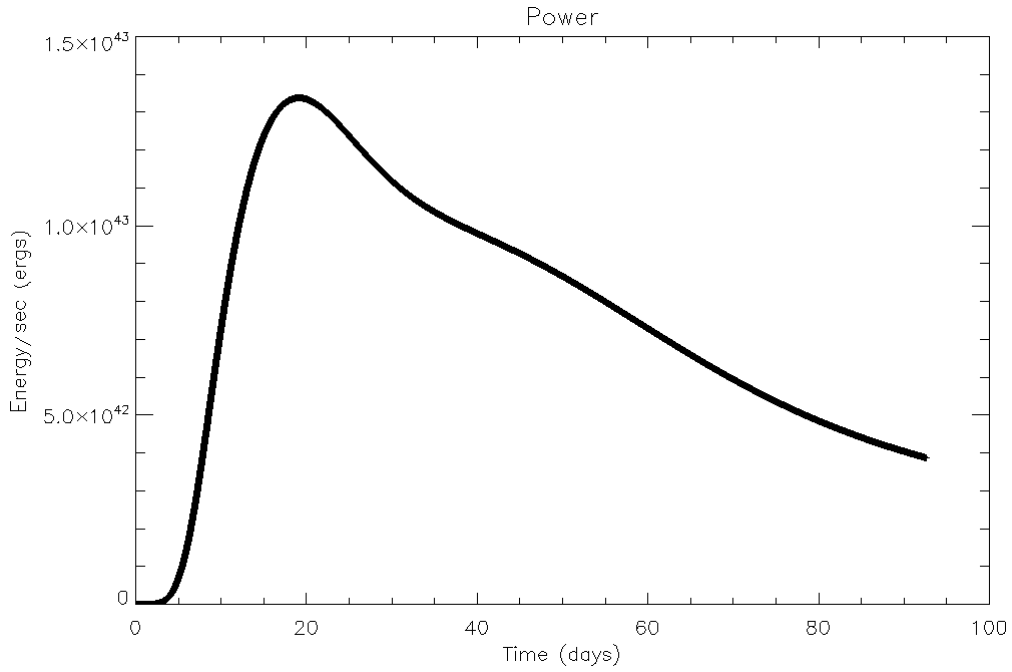

Figure 2.7 The light curve of a SN with 1 $M_\odot$ of ^{56}Ni generated from our simple model. The light curve portrays a higher and earlier peak light than that of the lesser amount of ^{56}Ni.

for 1 $M_\odot$ of ^{56}Ni. The overall power is much lower for the lesser amount of ^{56}Ni and is released over a longer period of time.

2.4.5 Assumptions

Though our model has proven it can reproduce the important characteristics of a SN Ia light curve, there are a number of key assumptions made that should be noted. Our first assumption is that the physics of the ejecta can be captured by modeling only four separate pieces. In actuality, the SN varies on much smaller scales. With a finer resolution, which would allow a finer tweaking of expansion parameters and chemical composition,

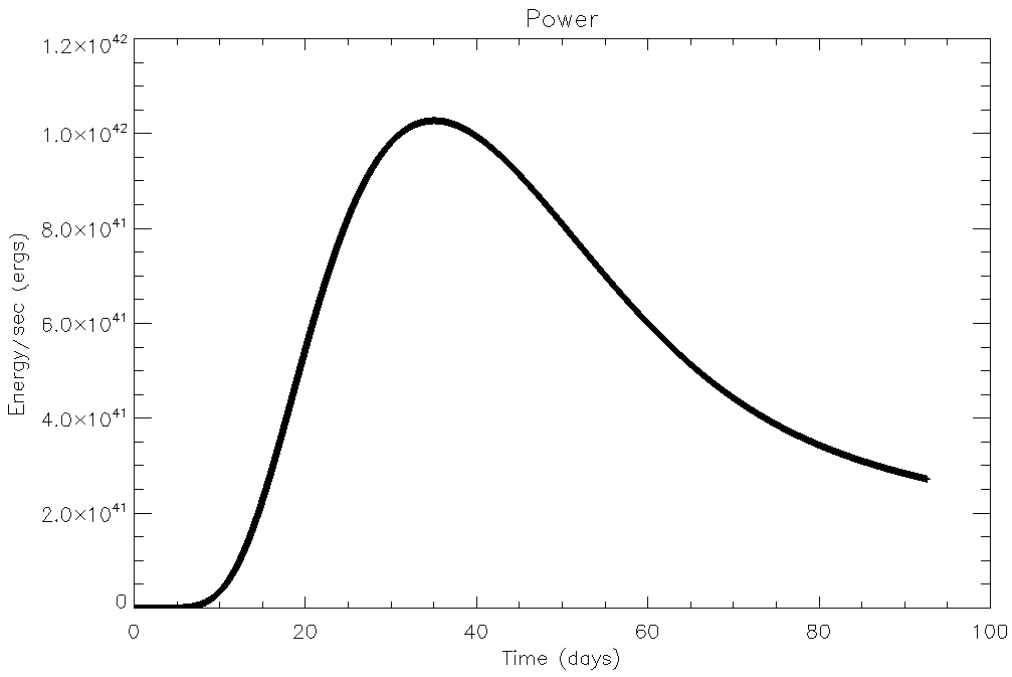

Figure 2.8 The light curve of a SN with 0.07 $M_{\odot}$ of ^{56}Ni generated from our simple model. The light curve exhibits a much lower peak light and much more broad/curved shape than that of the SN with more ^{56}Ni

the model light curve should better miimc the smooth shape of Contardo et al. (2000)'s bolometric observations. Also, our choice of a constant opacity throughout the ejecta over all times and frequencies is a very broad assumption. Although the model would benefit from a self-consistant, time-dependent opacity calculated from first principles, it would be notoriously complex to do so. Perhaps the next step would be to employ a monte carlo simulation of individual photons. Additionally, we assume that energy only propogates outward. However in a true random walk, there would be as much chance of backward motion as forward. It is possible that the density gradient that decreases with radius would encourage the forward propogation of photons. The backwards scattering of light would serve to prolong the light curve — pushing the escape of energy to later epochs.

Though each assumption mentioned above alters the apperance of the light curve, arguably the most imporant is the assumption of *in situ* deposition of gamma rays and

positrons. While this is an accurate assumption for early times, when the ejecta is dense, at some point the gamma rays are able to escape.

2.5 Late Times

At late times, the assumption of immediate deposition of decay energy is no longer valid. As the ejecta expand, the opacity decreases, and more gamma rays escape without depositing their energy. It is important to know when this transition between early and late epochs occurs so that assumptions are applied at only the epochs they characterize.

2.5.1 Gamma Ray Transport & Deposition

Gamma rays from radioactive decays lose their energy through compton scattering. This is illiustrated in Figure 2.9 where a photon scatters off an electron, transferring some of its energy in the process. Conservation of momentum leads to the expression for the

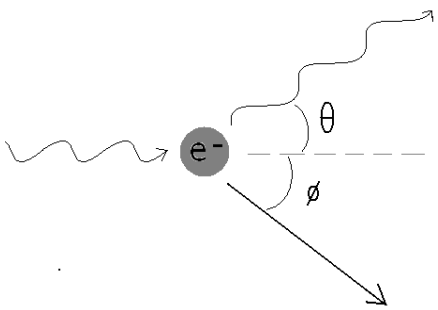

Figure 2.9 An incident photon hits an electron, transferring some energy, the photon leaves with a different energy at a scattering angle, θ while the electron leaves with some kinetic energy at an angle ϕ.

change in wavelength of the photon:

$$\Delta\lambda = \lambda_c(1 - cos\theta), \tag{2.28}$$

where θ is the scattering angle of the photon, and $\lambda_c \equiv \frac{h}{m_e c}$ is the Compton wavelength. The maximum change in energy occurs when the photon back scatters, $\theta = \pi$ and $\Delta\lambda = 2\lambda_c$. If

the original wavelength is some fraction of the Compton wavelength, $\lambda = \frac{\lambda_c}{n}$ (and energy $E = \frac{nhc}{\lambda_c}$), the photon after scattering leaves with wavelength,

$$\lambda' = \frac{2n+1}{n}\lambda_c = (2n+1)\lambda \tag{2.29}$$

and energy,

$$E' = \frac{E}{2n+1}. \tag{2.30}$$

Thus, the potential for energy loss scales with the initial photon energy. Multiple scatters quickly reduce the energy of gamma rays to thermal energies. The energized electron goes on to excite atomic transitions which de-excite, adding to the spectrum of escaping light.

However, as the ejecta expands, the density of electrons decreases, and compton scattering becomes infrequent. The ejecta becomes completely transparent to gamma rays when the compton scattering optical depth (τ_c) becomes less than one. At this point, a photon can traverse the entire medium without being absorbed. For a gamma ray undergoing compton scattering, the optical depth is

$$\tau_c = n_e \sigma_c d, \tag{2.31}$$

where n_e is the number density of all electrons (gamma rays don't discriminate between bound or free electrons), d is the distance across the medium, and the Compton scattering cross section is

$$\sigma_c = \sigma_T \frac{3}{4}\left[\frac{1+x}{x^3}\left(\frac{2x(1+x)}{1+2x} - \ln(1+2x)\right) + \frac{\ln(1+2x)}{2x} - \frac{1+3x}{(1+2x)^2}\right], \tag{2.32}$$

where σ_T is the Thompson cross section, and $x = h\nu/m_e c^2$. For a gamma ray of 1 MeV undergoing compton scattering within a Chandrasekhar mass SN ejecta with 0.6 $M_\odot$ of ^{56}Ni, tau was calculated for each shell. Figure 2.10 shows the total optical depth as a function of time.

After 67 days, $\tau_c = 1$ and all gamma rays escape from the ejecta without depositing any energy — even those from the very core of the SN. This marks the beginning of the nebular phase for gamma rays. However, some rays escape before this time. τ_c steadily decreases, which means that in the time leading up to the nebular phase, gamma rays escape

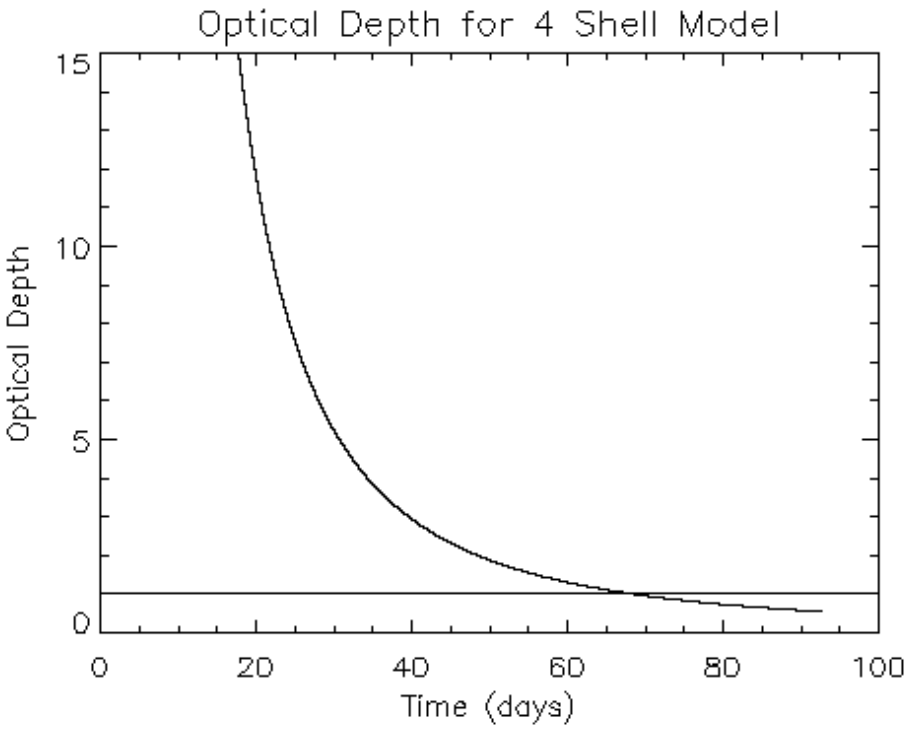

Figure 2.10 The optical depth for a 1 MeV gamma ray from the center shell to the outer edge of the ejecta as a function of time. Note that it goes to one (crosses the straight horizontal line) at 67 days, signifying the arrival of the nebular phase for gamma rays.

after fewer and fewer scatters, perhaps retaining a significant portion of their energy. Also, the optical depth reaches one sooner in the outer layers, so gamma rays escape earlier if produced there. For various energies of photons, the subtle transition from photospheric phase to nebular phase corresponds to the time from about 100 to 200 days. As the ejecta is deprived of more and more energy, the light curve dims more quickly than at earlier epochs.

It is apparent that for our model, the light curve in Figure 2.4 cannot be trusted after (and perhaps a short time before) 67 days. At this point, the model is overestimating the amount of power contributed to the light curve.

2.5.2 Positron Transport & Deposition

With the total escape of gamma rays, the light curve is now powered only by the deposited positron kinetic energy. Positrons are produced in ^{56}Co decays with kinetic energys ranging from 0 to 1.459 MeV, but with typical energies of 0.632 MeV (Nadyozhin, 1994). The deposition of a positron's kinetic energy occurs in the same way as that of the energetic electrons from Compton scatterings. Positrons may also annihilate with an electron to form two photons of 511 keV each, or three photons whose energies add up to 2×511 keV. However, at late times when the contribution to the luminosity might have been significant, the ejecta is transparent to these high energy photons, and their energy is lost. See section 1.6.1 for a discussion on whether positrons escape the ejecta at late enough times.

CHAPTER 3

OBSERVATIONS

Observations discussed in this chapter are of SN2007ax, SN2008D, and SN2006D. The two former SNe were observed with the Super-LOTIS 0.6m telescope in the optical, while SN2006D was observed with Super-LOTIS, the Kuiper 1.54m telescope, and the Mayall 4m telescope in both the optical and near-infrared.

3.1 Telescopes and Instruments

3.1.1 Super-LOTIS

Super-LOTIS (Livermore Optical Transient Imaging System) is a robotic telescope situated at Kitt Peak National Observatory (KPNO) near Tucson, AZ that nightly observes SNe, novae, and GRBs. It is currently supported by a collaboration that includes Steward Observatory, Lawrence Livermore National Laboratory, NASA GSFC, Clemson University, and UC Berkeley Space Sciences Laboratory. It has a 0.6m aperture, a 17' x 17' field of view, and can take about 250 60-second exposures each night. Observations obtained with Super-LOTIS were in B, V, R, I. However, since 2007, the telescope has only V, R, I and $H\alpha$ filters.

3.1.2 Kuiper Telescope

The Kuiper telescope, located on Mount Bigelow in the Catalina Mountains north of Tucson, AZ, is operated by Steward Observatory. It has a field of view of 7.25' in diameter and observes in B, V, R, I, J, H, K.

3.1.3 Mayall

KPNO is also home to the Mayall telescope, which has an aperture of 4m and can support a number of instruments. The two used in this study were MOSAIC and FLAMINGOS. The MOSAIC instrument, designed for wide-field optical imaging, is made of an array of 8 CCD chips with a field of view of 36'. FLAMINGOS is a wide-field IR

imager and multi-slit spectrometer. For imaging, it affords a field of view of 10' by 10' in filters: J, H, K, Ks. While the portion needed to observe SNe is small relative to both fields of view, the large field allows a SN field to be shifted without worry that it will be accidentally positioned off the CCD.

3.2 Observational Analysis Techniques

Our observations of SNe Ia are captured first as charge from incident photons, and then recorded as digital images. Understanding the science contained in these images depends on our comprehension of the physics that goes into the method of measurement. Thus, in this chapter we digress to examine the techniques needed to reduce and analyze SNe Ia photometric observations.

3.2.1 Reductions

The physics of charge-coupled devices (CCDs) drives our data reductions. Incident photons strike the mostly silicon CCD ejecting an electron via the photoelectric effect. The resultant charge is collected by each pixel, read out by an output amplifier, and converted to a digital number (Howell, 2000). The collection of digital numbers creates a digital image with higher numbers (or counts) standing in for higher photon incidence — indicating brighter objects. However, imperfections in the CCD and output processes introduce noise that does not directly relate to photon flux.

Read Noise

The spread of values that occurs when transforming the stored charge to digital counts, and the extra electrons generated by the electronics are both lumped under the umbrella of "read noise." In fact, the fluctuations due to each are inseparable in the output (Howell, 2000). To make sure the fluctuations never result in a negative value, a positive offset (the bias) is added to each image. One can calibrate the bias and noise in two ways.

After an image has been read-out, additional rows or columns of pseudo-pixels can be read-out and appended to the image. This is called an overscan strip, and it reveals what is recorded when there is nothing to record. Alternately, images called "zeros" or "bias

frames" are taken with a zero time exposure, indicating the bias level, but also betraying any 2-dimensional structure that might exist across the bias.

To "zero" one's image, one takes the mean value of the overscan region and subtracts this number from each pixel, producing a bias-corrected image. Or one can take the median of multiple zero images and do a pixel-by-pixel subtraction from all other images.

Dark Current

Dark current, the thermal generation of electrons in a silicon CCD, can also introduce fluctuations in measurements. In an effort to minimize thermal effects, most CCDs and surrounding equipment are cooled by liguid nitrogen, keeping the temperature at $\sim -100°$C. "Darks," images taken at the same exposure time as one's science images, but with the shutter closed, do well at measuring the dark current and approximating the rate of cosmic ray strikes. Darks can also sample defective pixels on the CCD which might not be as obvious in science images (Howell, 2000). Multiple darks can be averaged together into a resultant "master dark," which can be subtracted from the science images.

Flat-Fielding

Ideally the reduced images are now artificial-fluctuation-free, and have uniform illumination across the background. But, as Mackay (1986) says, "The only uniform CCD is a dead CCD." Unfortunately, there still exist pixel-to-pixel variations, and one needs to obtain a flat image with which to flatten science images. The technique for doing so is different if one is observing in the optical or near-infrared (NIR) energy regimes.

Optical Flats

Many telescopes have a flat screen mounted within the dome that are illuminated as uniformly as possible by a light source. One can point the telescope at the screen and take "flats." Alternatively one can observe the twilight sky which acts as a fairly flat field. Because pixels respond differently to different colors of light, flats need to be taken in each filter used in observations (Howell, 2000). Multiple flats can be averaged together to form one master flat per filter. Then observation images can be divided by the master flat in that filter.

Near-Infrared Flats

Both the twilight sky and illuminated flat screen are too bright in the NIR to be used for flats. So instead, one can create flats from the observation images.

For this to work, observations need to have been dithered. This means that after each image is taken, the telescope moves slightly, placing the object at a different spot on the CCD before another image is taken. The dithering is usually done in a pattern, repeating after a set number of times. For a given image in a series, one can take a number of its neighbors and combine them into a single flat image, slecting the median value pixel-by-pixel. This is another form of sky flats, but here, there is a separate flat for each observation image. Only the neighbors are used in case there is any time-variation in counts in the sky background.

Image Reductions

Optical and NIR images were reduced using the Image Reduction and Analysis Facility (IRAF) software package.[1] Most of the tasks mentioned above were done with programs in the CCDRED package. Images were overscan strip corrected and cropped with CCDPROC. Bias frames were combined using ZEROCOMBINE, and subtracted from all images using CCDPROC. Darks were combined with DARKCOMBINE and subtracted from flats and object images according to exposure time (and if necessary scaled to the appropriate time) using CCDPROC. For optical images, dome flats were median-combined into master flats according to filter with FLATCOMBINE. Sky flats for NIR images were created in the manner described above using COMBINE. Then each science image was divided by the appropriate master flat.

3.2.2 Photometry

With the images appropriately reduced, one can measure the brightness of an object using photometry. Photometry involves translating the value of counts of an object to an

[1] IRAF is distributed by the National Optical Astronomy Observatories, which are operated by the Association of Universities for Research in Astronomy, Inc., under cooperative agreement with the National Science Foundation, http://iraf.noao.edu

actual apparent magnitude. We seek to measure the magnitude of a SN Ia, but the same methods can be applied to almost any point source.

Aperture photometry is generally done by recording the total counts in a small aperture about the point source. The size of the aperture should be such that most of the source photons are included, but small enough that not too much of the background is enclosed. The sky background in counts is also sampled from a larger ring known as the sky annulus as is shown in Figure 3.1. The background is then subtracted from the source

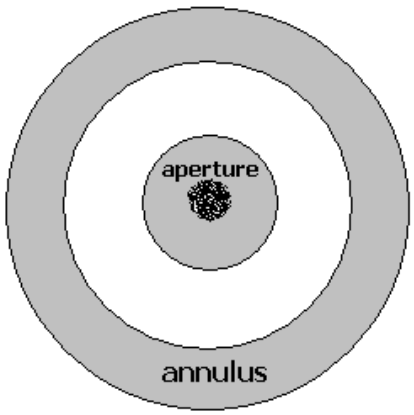

Figure 3.1 In photometry, an aperture is placed around an object (black dot) and the annulus, used to sample background counts is placed in a ring further out from the source.

to determine the flux of the star. For times when the SN was faint, a small aperture was chosen, and was then aperture corrected using the task MKAPFILE. This examines how the magnitudes change for different sized apertures (curve of growth) for other, brighter, objects, and corrects for the smaller sized aperture about the SN. In this way, the SN and any other stars measured (field stars) are assigned an instrumental magnitude.

The instrumental magnitudes can be translated into actual apparent magnitudes through calibration by standard stars — stars whose apparent magnitudes are well known in multiple filters. Observations are taken of the SN field, and also of standard star fields. A

catalog of known apparent magnitudes is created using MKCATALOG. The differences between actual and instrumental magnitudes of stars depend on the color response of the filter observed in, the amount of airmass through which the field was observed, and differences in instrument characteristics. Thus, the transformation equations look like:

$$mB = (BV + V) + b1 + b2 * XB + b3 * BV + b4 * BV * XB \quad (3.1)$$

$$mV = V + v1 + v2 * XV + v3 * BV + v4 * BV * XV \quad (3.2)$$

$$mR = (V - VR) + r1 + r2 * XR + r3 * VR + r4 * VR * XR \quad (3.3)$$

$$mI = (V - VI) + i1 + i2 * XI + i3 * VI + i4 * VI * XI, \quad (3.4)$$

where mB, mV, mR, and mI are the instrumental magnitudes. BV, VR and VI are the colors $B - V$, $V - R$, and $V - I$ respectively, where B, V, R, I are the actual magnitudes in each filter. $b1, v1, r1, i1$ are offsets in magnitude, XB, XV, XR, XI are the airmass values (how much of the Earth's atmosphere is between the telescope and observation field) with associated coefficients $b2, v2, r2, i2$. $b3, v3, r3, i3$ are the coefficients for the color terms. The task FITPARAMS begins with initial guesses of coefficients, and then iterates until the fit converges, or a maximum number of iterations is reached. If not all filters are observed, the color terms in the above equations may be altered to reflect the filters one has. In order to calculate the airmass coefficient, standard fields at different airmasses need to be observed.

The INVERTFIT task applies these recently calculated coefficents for standard stars to the instrumental magnitudes of the SN and field stars, yielding (if all has gone well) the coveted actual apparent magnitude of the SN. IRAF tasks compute uncertainties at each step, which are reported with the apparent magnitudes.

Multiple images of the SN in each band are taken each night to increase the signal-to-noise of the observations. One can calculate the apparent magnitude for each image and then take the average value. Alternatively, one could first align and then combine ("stack") the images together to form a master object image per filter before calculating the actual magnitude of the SN. Super-LOTIS observations were done in the latter manner. All other observations were done both ways, but there was very little difference in the final magnitudes.

The process of observing zeros, darks, and flats should be done each night. It is desirable to also observe multiple standard star fields each night, but if a night occurs in which standard stars cannot be observed, one can use the field stars, calibrated from a previous night, to solve for the parameters of the fit equation. This is known as relative photometry.

3.3 SN2007ax

Supernova 2007ax was discovered on March 21, 2007 by Arbour (2007) in NGC 2577 at $\alpha = 08h22m43s.23$, and $\delta = +22°33'16''.9$. Spectra were obtained on March 27 by Blondin et al. (2007) and Morrell and Folatelli (2007) which indicated it was a SN Ia at maximum light with characteristics similar to SN1991bg. It was added to the Super-LOTIS queue on April 17, 2007 and was observed almost nightly until June 4.

Super-LOTIS scripts automatically reduce the SN images and attempt to stack each band of observations at the end of the night. However, the stacked images are poorly aligned and often contain blurry or streaked images. I performed quality control, cropped, and aligned every image before median-combining them to make master object images in each filter. In the process I refined some Super-LOTIS scripts and wrote one of my own called slotis_imcrop.

On February 14, 2008 another observation of the SN2007ax field was made with Super-LOTIS. Images acquired this late no longer show a SN and were used as subtraction images. By subtracting the SN-free field from the science image, any extra light from the nearby galaxy that might have contaminated SN magnitudes should have been removed. Then photometry was done in a similar manner to that described in section 3.2.2.

Combining the Super-LOTIS data with observations at earlier times and in other filters, a bigger story about this SN is revealed. Figure 3.2 shows the light curve modified from Kasliwal et al. (2008). It is difficult to accurately gauge the $\Delta m_{15}(B)$ because a change in slope occurs $\sim$ 10 days after max — before the parameter can be measured. Kasliwal et al. (2008) choose to classify subluminous SNe Ia by the time (t_b) after maximum light that this change in slope occurs. Out of a sample of 6 subluminous SNe, SN2007ax's $t_b = 10.3$ days is the shortest by 4.5 days.

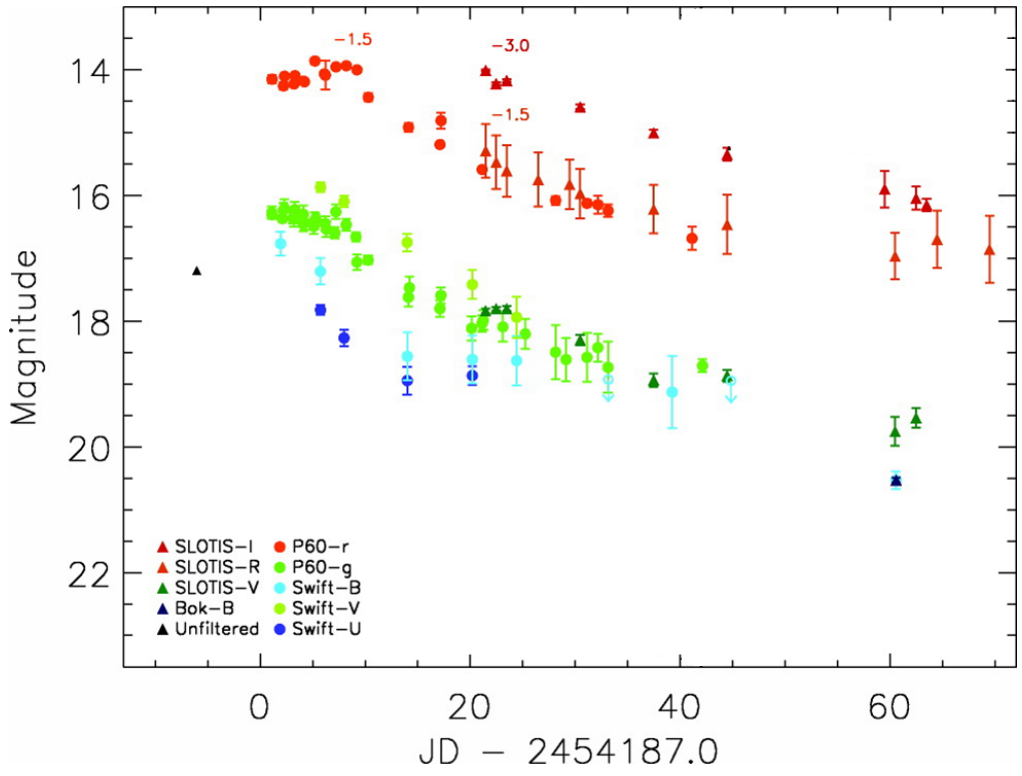

Figure 3.2 The light curve of SN2007ax in multiple bands. Observations were made as indicated in the key, by Swift UVOT, the Palomar 60' telescope, the Bok 2.3m telescope, and the Keck II Near Infra Red Camera 2. The R/r and I bands are offset as indicated for clarity.

At an absolute magnitude of $M_B = -15.9$, SN2007ax is the dimmest SN observed. It is also the reddest with a $B - V = 1.2$ at maximum B light. Figure 3.3 compares the SN2007ax light curve to the light curve of the archetype subluminous SN1991bg, and another subluminous SN1991by from Garnavich et al. (2004). The light curve in B is similar to SN1991bg, but seems to decline a bit faster. Other lines appear relatively similar.

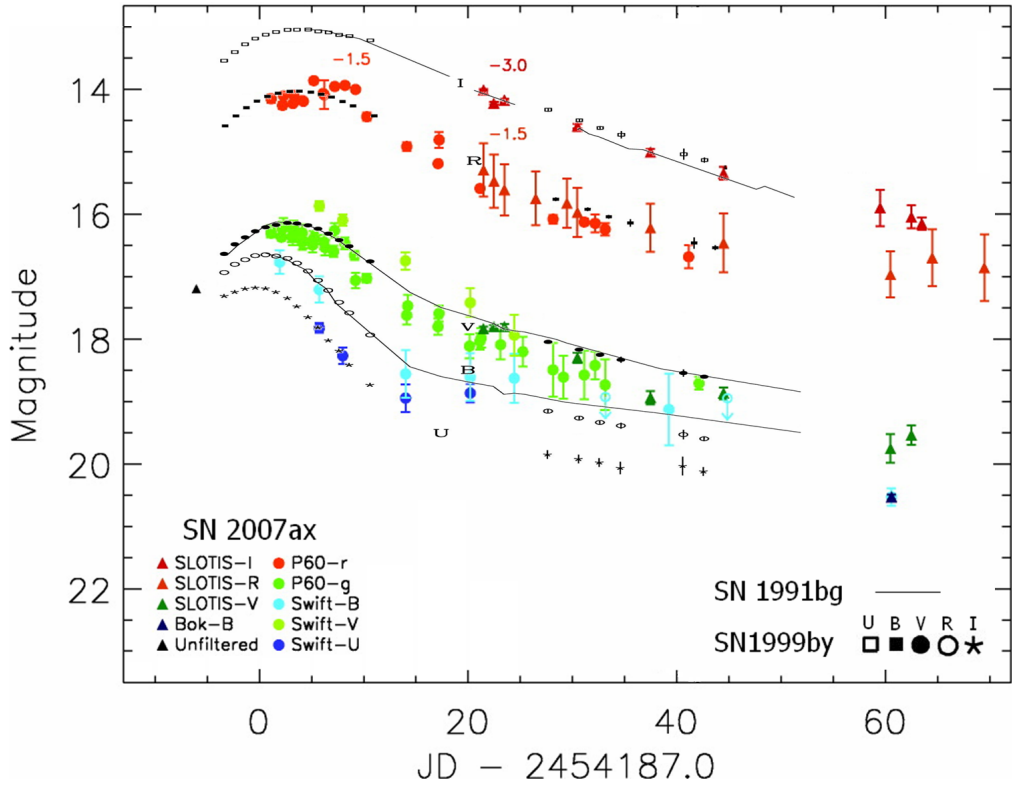

Figure 3.3 The light curve of SN2007ax (color) from Kasliwal et al. (2008), overlaid with those of SN1991bg (labeled lines), and SN1999by (black symbols) from Garnavich et al. (2004). The U, R, and I light curves of SN1991bg and SN1999by are offset in magnitude (by eye) to match those of SN2007ax.

It has been suggested that the number of subluminous SNe Ia is underestimated because dimmer objects are less likely to be seen. However, an observation of a SN this dim indicates that the technology is in place to observe these subluminous phenomena. There may be a continuum of SNe of decreasing magnitude, perhaps correlated with explosions

that produce less and less ^{56}Ni. It is unkown just how far it extends. Observations, like this of SN2007ax, expand the known limits of SNe Ia. Once thought to be a homogeneous group, SNe Ia are delevoping a higher degree of diversity as observations increase. For more on SN2007ax, see Appendix C.

3.4 SN2008D

On January 9, 2008 while observing SN2007uy in the galaxy NGC 2770 with the Swift X-ray Telescope, Berger and Soderberg (2008) witnessed a bright x-ray outburst at $\alpha = 09h9m30s.65$, $\delta = +33°08'20''.3$ (See Figure 3.4). 1.4 hours later, the Ultraviolet/Optical Telescope (UVOT) on Swift revealed a UV-optical counterpart.

Spectra taken 1.74 days later (Soderberg et al., 2008), and subsequent spectra by Page et al. (2008) and Li and Filippenko (2008) revealed that this was a type Ibc SN2008D — a core-collapse SN the displays a lack of H and Si, like those discussed in section 1.1. It is likely the X-ray outburst had its origins in the break-out of the SN shockwave (Soderberg et al., 2008). This is when the outflow decreases in density enough that the optical depth becomes one, and optical and x-ray light are able to escape. These emerging photons are then upscattered (comptonized) by the surrounding dense material left by stellar winds. It is likely that this intense X-ray outburst occurs before every core-collapse SN.

Because SN2008D was discovered well before maximum light, observations in multiple wavelengths were able to map a full light curve. Super-LOTIS was already observing the field to monitor SN2007uy when SN2008D was discovered, and would have had excellent early data were it not for some untimely maintenance. Observations by Super-LOTIS were reduced in the same fashion as those of SN2007ax. The multi-band light curve constructed from observations by Super-LOTIS and other telescopes is seen in Figure 3.5. See Appendix D for more on SN2008D.

3.5 SN2006D

SN2006D was discovered January 11, 2006 by Colesanti et al. (2006) of the Brazilian Supernovae Search (BRASS). It was located at $\alpha = 12°52'34.7''$ and $\delta = -09°46'36''$ in the galaxy MCG-01-33-034, at $\sim$ 36.5 Mpc away. On January 14, Aldering et al. (2006)

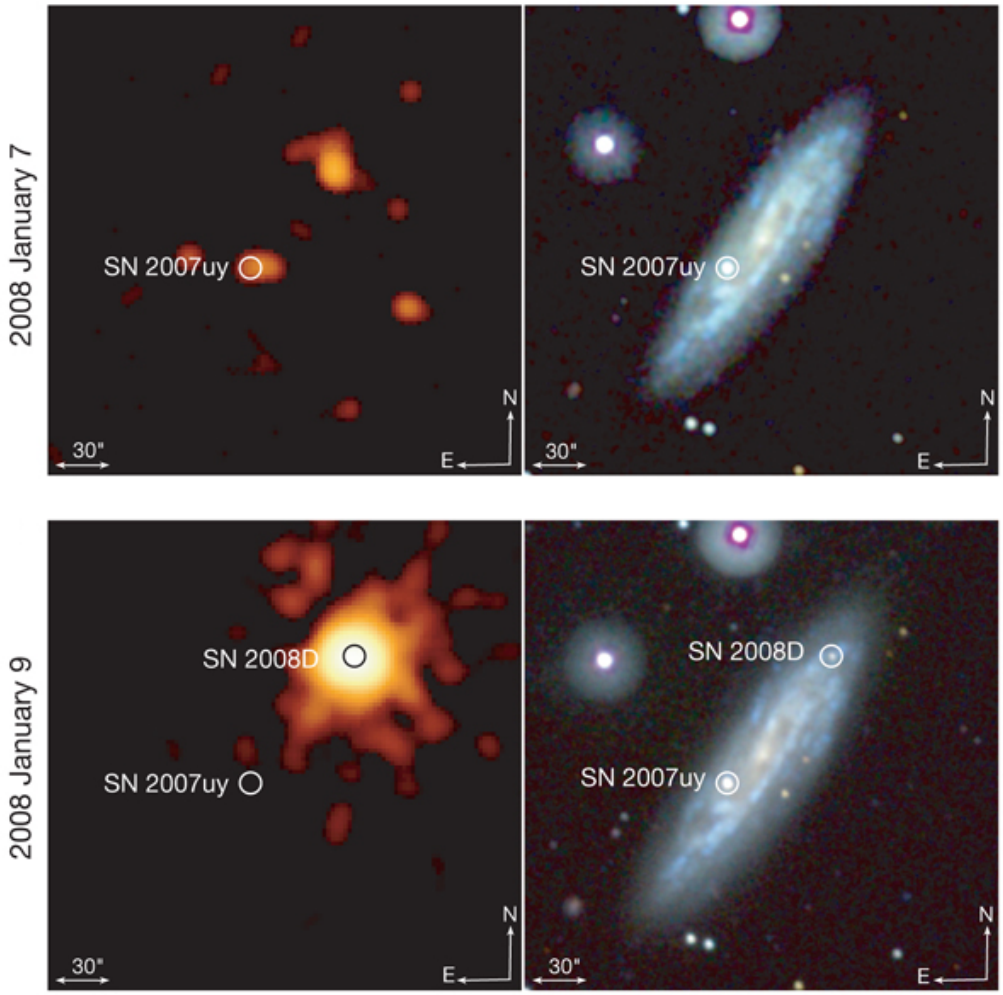

Figure 3.4 X-ray (left) and ultraviolet (right) images of NGC 2770, showing the x-ray out burst and UV component of SN2008D which occurred during observations of SN2007uy.

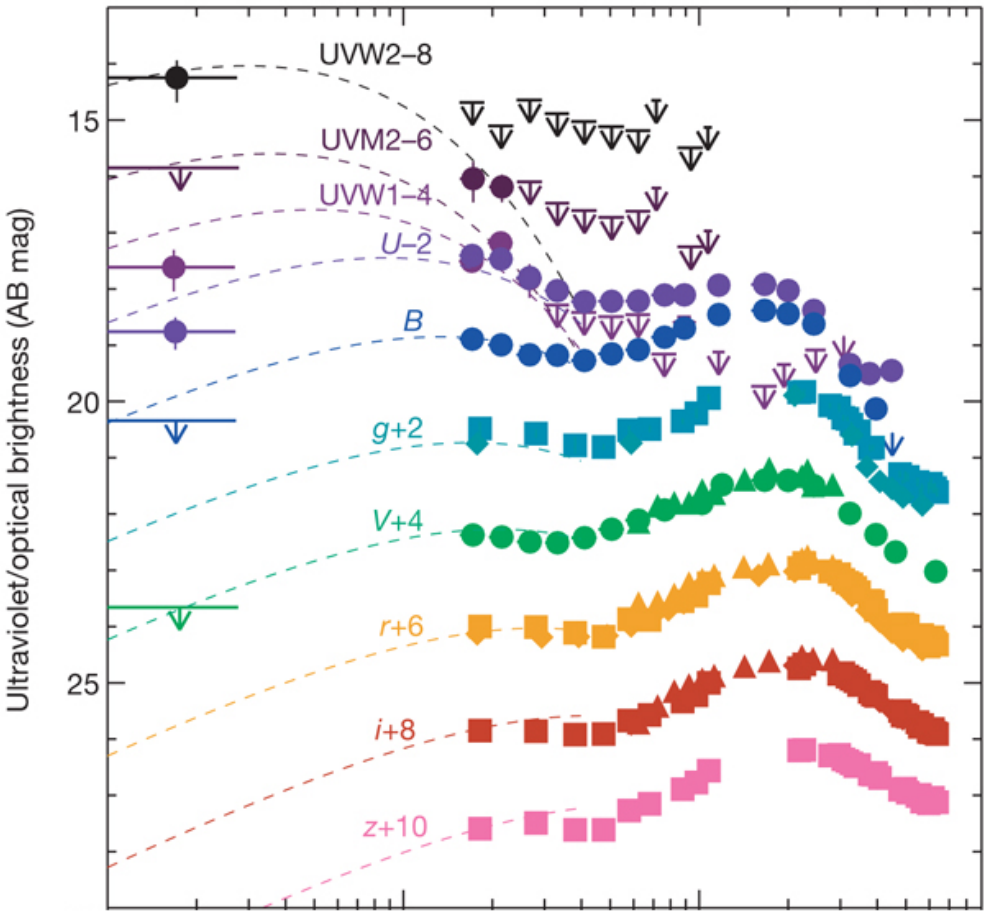

Figure 3.5 Light curve of SN2008D in multiple bands. Data were obtained with Swift UVOT (circles), the Palomar 60-inch telescope (squares), Gemini/GMOS (diamonds), and Super-LOTIS (triangles), and have been offset arbitratily in bands for clarity.

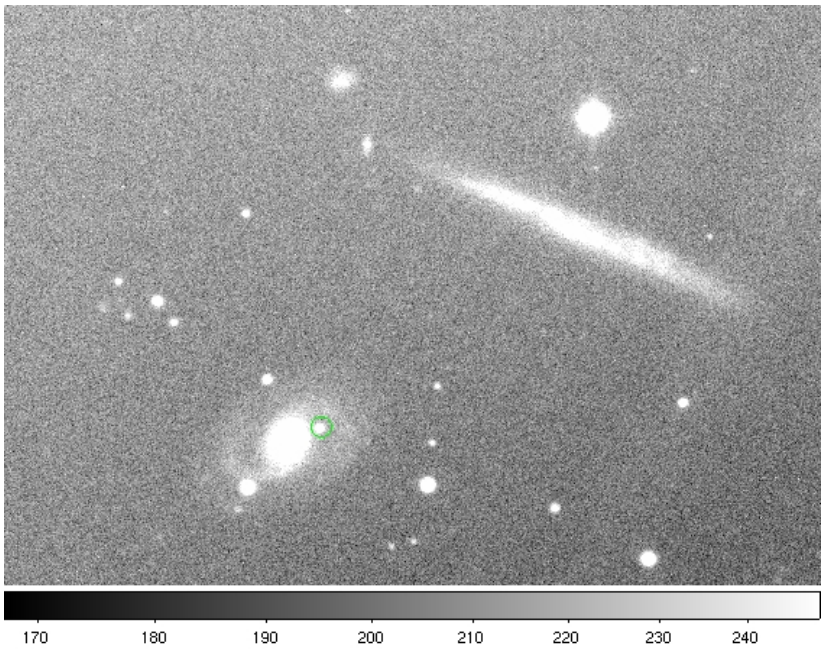

Figure 3.6 A Super-LOTIS image observed in the V band. SN2006D is circled in green and is just the right of its host galaxy, nestled in a spiral arm. Another galaxy, edge-on can be seen as a thick line in the upper right corner, just below a bright star. The color bar on the bottom indicates the contrast in brightness in counts.

obtained spectra and classified SN2006D as a SN Ia about one week prior to maximum with an unusually strong carbon feature.

3.5.1 Early Times

Super-LOTIS started nightly observations of SN2006D in B, V, R, I on January 22 and continued until May 25, 2006. From April 19 to May 12, 4 nights of observations were made with the Kuiper telescope in B, V, R, I and one night in H, J. Unfortunately, the dithering was minimal for the H, J observations, and a flat could not be made. Thus, photometry could not be reliably done. An observation of the SN2006D field was also made with the Bok 2.3m telescope in R, but the quality was too poor to make out the SN.

The Super-LOTIS images were reduced in a manner similar to 2007ax, however, image subtraction has not yet been done. Kuiper images were reduced and magnitudes calculated in the fashion described in sections 3.2.2 and 3.2.1. The composite light curves in B, V, R, I from these telescopes are shown in Figure 3.7. The B, V, I light curves are

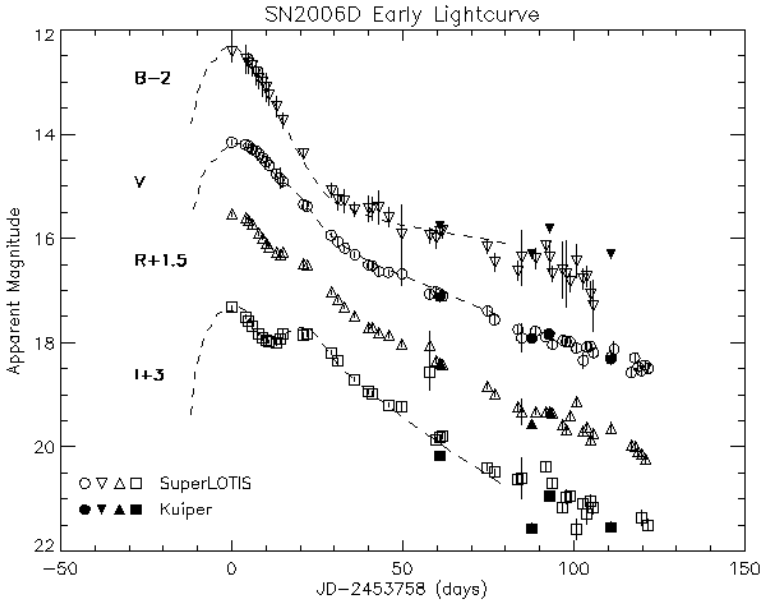

Figure 3.7 Early observations of SN2006D from Super-LOTIS (open symbols) and Kuiper (filled symbols) telescopes in B, V, R, I. The light curves are offset arbitrarily and fitted with B, V, I templates based on SN1992A from Hamuy et al. (1996). SN1992A is characterized as having a $\Delta m_{15}(B) = 1.47$mag.

fitted with templates from Hamuy et al. (1996). These particular templates are based on the observed light curve of normal SN1992A which had a $\Delta m_{15}(B) = 1.47$mag. Indeed, the shape of the light curves match those of the normal SNe seen in Figures 1.2 and 1.4. Around 100 days, the Kuiper B magnitudes are slightly higher than those of Super-LOTIS. A color correction term of $-0.2 \times (B - V)$ is not included in the data. The bluer edge of Super-LOTIS's filter cuts off, thus underestimating B magnitudes by as much as 0.3mag. Perhaps this is the cause of the mismatch between Kuiper and Super-Lotis data.

3.5.2 Late Times

May 24 and 25, 2007 afforded additional observations of the SN field in V, R with MOSAIC, and in H, J with FLAMINGOS. However, these late observations are severly influenced by contamination light from the galaxy. The location of SN2006D makes photometry exceptionally difficult (see Figure 3.6). When nestled in the crook of the galaxy spiral arm, counts from the SN are hard to differentiate from counts contributed by the host galaxy. The sky annulus, if placed around the SN (see Figure 3.1), would not estimate an accurate sky background. Thus, a subtraction image is necessary to remove the host galaxy before photometry can be done. Because they are taken at an impressive 490 days after maximum light, the H, J observations have enough contamination that the SN cannot be picked out. The SN can be seen in the MOSAIC images, but as Figure 3.8 reveals, the magnitudes are higher than expected, suggesting a large amount of contaminant light. Thus subtraction images are also needed in V, R. If the bright late magnitudes are approximately correct, it may indicate that SN2006D is a "Shallow R" SNe Ia like some observed by Lair et al. (2006). In Figure 3.8, the decline rate r1 is that of typical SNe Ia at 200+ days, but r2, which seems to fit better, is the decline rate observed by Lair et al. (2006). This possibility makes it even more imperative to acquire optical subtraction images.

Though the light curve of SN2006D looks somewhat sparse, there are plans to collaborate with other observers who acquired not only photometry, but also spectra (Thomas et al., 2007). Also, with subtraction images, and thus accurate photometry, reliable late

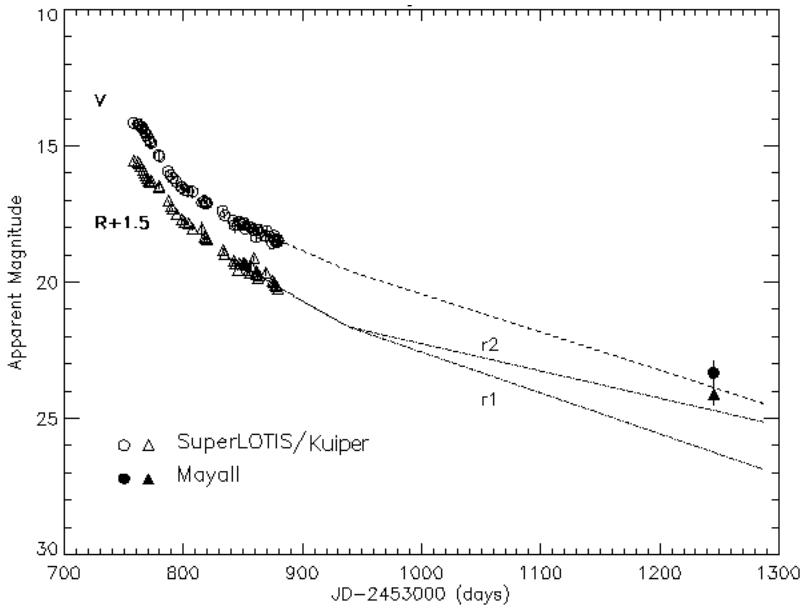

Figure 3.8 The late light curve of SN2006D in V, R combines early observations by Super-LOTIS and one late observation using MOSAIC on the Mayall telescope. The dotted lines are projected declination rates from 100-200 days, and greater than 200 days. The high magnitudes of the late observation may indicate host galaxy contamination. Of the two 200+ R decline rates, r1 is that of normal SNe Ia, while r2 is the observed slope of "shallow R" SNe as observed by Lair et al. (2006).

NIR and V, R magnitudes may shed more light on the late time behavior of SN2006D. Subtraction images have already been observed with Super-LOTIS and can be used, along with color correction, to refine the early light curve.

With more experience in observing, reducing, and analyzing SN images, future endeavors can only get better, and with it, an enhanced understanding of SNe Ia.

CHAPTER 4
CONCLUSIONS

4.1 Models and Observations

SNe Ia evolution can be characterized with two epochs: a photospheric phase and nebular phase. The physics occurring at these epochs is very different. Initially, the power is supplied by the almost instant deposition of energy from gamma rays and positrons. It takes time for this energy to diffuse through and escape from the thick ejecta. The energy that escapes per unit time increases as the ejecta density decreases. However, the decrease in power from decays causes the light curve to turn over, and begin decreasing. This observed peak in the light curve usually ocurrs around 18 days after explosion.

Through experimentations with a simple model of an expanding SN ejecta, it is obvious that the shape and timing of the light curve is sensitve to both the amount and placement of ^{56}Ni.

Eventually the ejecta become diffuse enough for gamma rays to escape without depositing all of their energy. This transition period corresponds to around 100-200 days, and the loss creates a faster decline rate in the light curve. When the optical depth for a gamma ray $<< 1$, the only power comes from the deposition of positron kinetic energy. It is not yet fully understood whether positrons eventually escape or are trapped by magnetic fields at late times. At this late epoch, low temperatures mean observations in the NIR and IR are better at tracing the escaping energy.

As observations of SNe increase, our understanding grows. Well-sampled light curves with spectra are becoming the norm (see Appendices D and C). These require observations from multiple telescopes in multiple bands and, often, multiple observers. Observations serve to confirm or constrain models. SN2007ax showed us that the continuum of SNe Ia extends even farther into the subluminous than previously thought, and challenges theory to construct models that explain the brightest to the dimmest SNe. The serendipitous

observation of the early SN2008D confirmed core-collapse SNe models and allowed for a well-sampled light curve even before maximum light. SN2006D has afforded me an opportunity to increase my skills in observing, image reduction and photometry in multiple wavelengths. With subtraction images and collaboration data, SN2006D may shed some light on late time physics — in particular, it may add to the sample of "shallow R" SNe Ia as seen in Lair et al. (2006).

4.2 Future Work

Subtraction images have been obtained by Super-LOTIS that can be used to correct early observations of SN2006D. Future scheduled observing runs on KPNO's Mayall telescope will include acquiring V, R, J, H subtraction images for late observations. Super-LOTIS continued to monitor SN2008D and complementary late images have already been taken with an infrared imager on the Mayall. This will be a great addition to the already well-sampled early light curve. More multi-wavelength, multi-epoch, multi-telescope observations of SNe are planned. Well-sampled LC's of each SNe subclass could lead to a better understanding of the characteristics of the explosion mechanism. Multi-band observations and bolometric reconstructions, especially at late times, are needed to decipher if positron escape occurs.

The simple model examined in this work revealed a great deal about the physics of SNe Ia. With increased resolution and refined energy transport, more can be learned about the light curve shape's dependence on ^{56}Ni abundance and placement. More explosion scenarios (specifically those of the luminous subclasses) can be tesed with comparisons of model-generated light curves to bolometric observations. The model should also be able to predict light curves seen in certain bands by keeping track of the temperature of the "photosphere" as it receeds in mass coordinates further into the ejecta. This would allow comparisons to observations of just one band — a considerably smaller, and easier to acquire, amount of data than a bolometric light curve.

As in any field, observations and theoretical models must work in tandem: models attempting to explain observations, and observations constraining models to the actual physics. A refinement in both will be needed to understand the nuances of SNe Ia — why

there seems to be a spectrum in magnitudes and decline rates, and why some SNe deviate from this. Ultimately, this will have an impact on cosmological conclusions as we determine just how standard these standard candles are.

APPENDICES

Appendix A

COSMOLOGICAL IMPLICATIONS

Type Ia supernovae have played a guiding role in our "Adventures in Cosmology.[1] " Slipher (1915)'s spectroscopic observations of distant "nebulae" — later determined to be galaxies — indicated they were receeding from Earth. Hubble (1929), using the world's most powerful telescope (which, in the 1920's, was the 100 inch telescope on Mt. Wilson), determined that there was a linear relationship between a galaxy's distance away and at what velocity it was receeding. Hubble (1929)'s plot of radial velocity vs distance for a number of galaxies is reproduced in Figure A.1. This relationship is characterized by the

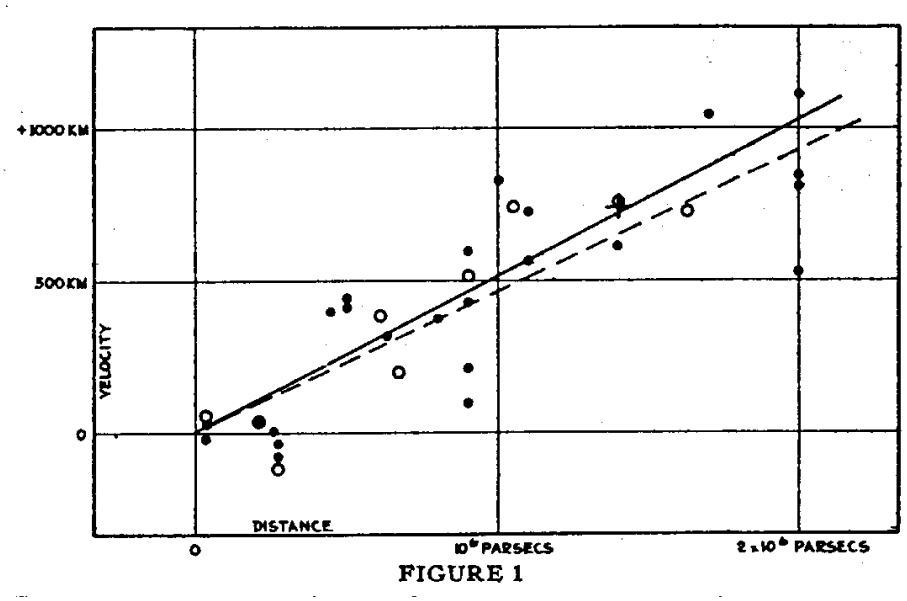

Figure A.1 From Hubble (1929), radial velocities of galaxies are plotted against distances from the Milky Way. The black discs represent individual galaxies, and the solid line is the best linear fit. The open circles are averages of groups of galaxies, while the dotted line is the fit for these. There appears to exist a linear relationship between distance and recession velocity of a galaxy.

[1] The title of a leaflet by Hubble (1938) on using distance measurements and redshifts to determine the state of the universe.

slope of the line, which is now called the Hubble constant. Hubble measured a slope of $H_0 = 464$ km/sec/Mpc.

Hubble's discovery, taken with the cosmological principle — that there is no preferred position nor direction in the universe — allowed one to conclude that everything was moving away from everything else. This was strong evidence that the universe was not static, but rather expanding, and it supported the idea of the "big bang."

Hubble's measurements of distance were derived from cepheid variable stars, but with some inaccuracies. He also did not account for peculiar velocities of galaxies (which can be several hundred km/s). Also, cepheid variable stars can measure distances up to only 16 Mpc. SNe Ia are a standard candle that allow more distant measurements of galaxies. Their uniformity and width-luminosity relation discussed in section 1.5 means their brightness can be determined from the shape of a light curve. Cepheids can be used to calibrate the distance to nearby SNe Ia, and distances out to ~ 400 Mpc can be accurately obtained. Measurements done in this way confirm the relationship observed by Hubble, but lead to a much smaller Hubble constant. Two groups using the Hubble telescope measured Hubble constants of $H_0 = 72 \pm 8$ km/sec/Mpc (Freedman et al., 2001) and $H_0 = 57 \pm 4$ km/sec/Mpc (Sandage et al., 2006).

If the rate of expansion has remained constant, we can use the Hubble law to determine how long ago everything was at the same place (i.e. when the big bang occurred). The Hubble law is:

$$V = \frac{dD}{dt} = H_0 * D, \tag{A.1}$$

where V is the recession velocity of a galaxy and D is the distance between the Milky Way and that galaxy. Thus the age of the universe would be $t = \frac{1}{H_0} = 13.2$ or 16.7 billion years old.

Intuition might suggest that gravity would have slowed down the outward rush from the big bang, but observations of distant SNe Ia at high redshift tell us a different story of how cosmic expansion has changed over time. Two groups, the High-z Supernova Search Team, and the Supernova Cosmology Project have observed dim SNe at unexpectedly great distances (see Figure A.2 from Riess et al. (1998)). These observations indicate that the

expansion of the universe has been accelerating. This surprising accelerated expansion suggests the existence of some force pulling the universe apart. We give this force a placeholder name of "dark energy."

Though Riess et al. (1998) have done their best to drive down systematic errors in their data, there are a number of uncertainties still remaining in the use of SNe Ia as standard candles. Inhomogeneity in SNe Ia light curves exists, threatening their status as standard candles. Also, it is unclear how their light curves and luminosity vary with redshift. Perhaps SNe Ia worked differently in the distant past. More observations and better models are needed to address these and perhaps other questions, to ensure our understanding of the expansion of the universe is accurate.

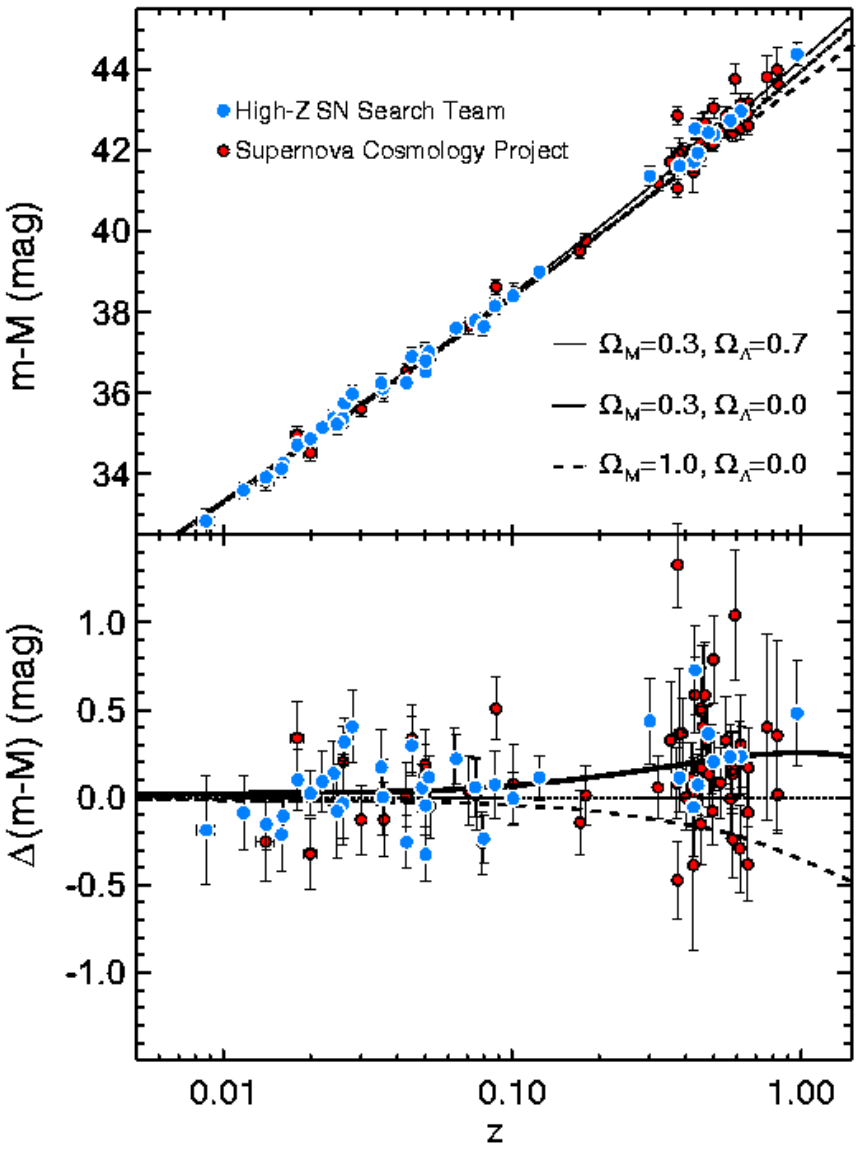

Figure A.2 From Riess et al. (1998). In the top panel, the distance moduli measured from SNe Ia by both the Supernova Cosmology Project (red) and the High-z Supernova Search Team (blue) plotted against redshift. The bottom panel shows the difference between the data and a model of cosmic expansion for a constantly accelerating universe. Also plotted are models for an accelerated expanding universe (solid line) and that of a decelerated expanding universe. Though at small redshifts, the difference in the models is indiscernible, at redshifts, the data seem to indicate the accelrated expansion model is correct.

Appendix B

WHITE DWARF

Type Ia supernovae are professed to be the result of a thermonuclear explosion of a white dwarf. Usually this white dwarf is thought to be in a binary with another star from which it continually accretes mass until it cannot support itself against the inward force of gravity. To understand the mechanics of a supernova, it behooves us to seek to understand a little more about its progenitor.

White dwarfs are the leftovers of stars of mass ranging from 1 solar mass to 8 or 9 solar masses. These post AGB stars eject their outer envelope and leave a still hot naked core of mostly Carbon and Oxygen. Most white dwarfs are around 0.6 solar masses and are about the size of the Earth. These very dense stars no longer have any fusion occurring, and are thus supported only by electron degeneracy pressure. Electron degeneracy occurs because of the immense gravitational pressure inwards. Each electron wants to occupy the lowest energy level, but, according to the Pauli-exclusion principle, no two fermions may occupy the same quantum state simultaneously. So each electron occupies the lowest unoccupied energy state, and a degeneracy pressure is built up. The star is stable as long as the electron degeneracy pressure is greater than the force of gravity.

Even though fusion no longer takes place in a white dwarf, these stars are still luminous for billions of years. The electron degeneracy lends itself to high thermal conductivity through electron conduction. Because of this, the star can be considered as isothermal except for a small outer convective envelope. In this envelope, the material is partially ionized and partially degenerate. The light that one sees is simply the slow cooling process of the white dwarf. The coolest white dwarfs are the oldest stars in our galaxy, and estimating the age of cool white dwarfs has led to an estimation of the age of the galaxy as being 9.3 $+/-$ 2 gigayears (Winget et al., 1987).

Appendix C

SN 2007ax: AN EXTREMELY FAINT TYPE Ia SUPERNOVA

The following was published in *The Astrophysical Journal* (2008, August 10)

The Astrophysical Journal, 683: L29–L32, 2008 August 10

SN 2007ax: AN EXTREMELY FAINT TYPE Ia SUPERNOVA

M. M. Kasliwal,[1,2] E. O. Ofek,[1] A. Gal-Yam,[1] A. Rau,[1] P. J. Brown,[3] S. B. Cenko,[4] P. B. Cameron,[1] R. Quimby,[1] S. R. Kulkarni,[1] L. Bildsten,[5] P. Milne,[6] and G. Bryngelson[7]

Received 2008 January 16; accepted 2008 July 3; published 2008 July 23

ABSTRACT

We present multiband photometric and optical spectroscopic observations of SN 2007ax, the faintest and reddest Type Ia supernova (SN Ia) yet observed. With $M_B = -15.9$ and $(B-V)_{\max} = 1.2$, this SN is over half a magnitude fainter at maximum light than any other SN Ia. Similar to subluminous SN 2005ke, SN 2007ax also appears to show excess in UV emission at late time. Traditionally, $\Delta m_{15}(B)$ has been used to parameterize the decline rate for SNe Ia. However, the *B*-band transition from fast to slow decline occurs sooner than 15 days for faint SNe Ia. Therefore we suggest that a more physically motivated parameter, the time of intersection of the two slopes, be used instead. Only by explaining the faintest (and the brightest) supernovae can we thoroughly understand the physics of thermonuclear explosions. We suggest that future surveys should carefully design their cadence, depth, pointings, and follow-up to find an unbiased sample of extremely faint members of this subclass of faint SNe Ia.

Subject headings: supernovae: individual (SN 2007ax, SN 1991bg, SN 1999by, SN 2005ke) — supernovae: general — ultraviolet: stars

Online material: color figure

1. INTRODUCTION

Inspired by the application as a standard cosmological candle, the progress in understanding Type Ia supernovae (SNe Ia) has grown in leaps and bounds. However, the understanding of their weakest subluminous cousins has been purposefully overlooked as their atypical light curve and atypical spectra make them contaminants for cosmological studies. We suggest here some characteristics that make the physics of the explosions of faint SNe Ia intriguing in their own right.

In this Letter, we present SN 2007ax which, with a peak absolute magnitude of $M_B = -15.9$ and $(B-V)_{\max} = 1.2$, is the faintest and reddest Type Ia supernova yet discovered. Although the class of SNe Ia is remarkably homogenous, subluminous SNe Ia show atypical spectral and light curve features (Garnavich et al. 2004; Taubenberger et al. 2008). Photometrically, not only do they fade much faster than predicted by the Phillips relation, they are also very red at maximum and (at least SN 2005ke and SN 2007ax) appear to show UV excess at late time. Spectroscopically, they have broad Ti II features and moderate expansion velocities.

SN 2007ax was discovered in NGC 2577, at $\alpha = 08^{\rm h}22^{\rm m}43.23^{\rm s}$, $\delta = 22°33'16.9''$, on UT 2007 March 21.978 by Arbour (2007) at an unfiltered magnitude of 17.2. Upper limits of >18.5 mag on March 17.636 and >19.0 mag on March 9.959 were also reported. Spectra obtained on March 26 by Blondin et al. (2007) and Morrell & Folatelli (2007) showed that it was a SN Ia near maximum light similar to SN 1991bg.

In this Letter, we present multiepoch, multiband imaging and spectroscopic follow-up of SN 2007ax including optical, ultraviolet, and near-infrared. We summarize our observations in § 2, present our analysis and comparison with other faint SNe Ia in § 3, and discuss possible scenarios for faint thermonuclear explosions in § 4. We conclude with how future surveys can systematically design their cadence, limiting magnitude, and pointings to search for more members belonging to this subclass of faint SNe Ia.

2. OBSERVATIONS AND DATA REDUCTION

The automated Palomar 60 inch (1.5 m) telescope (Cenko et al. 2006) started daily observations of SN 2007ax on UT 2007 March 29 in g' and r' bands. Data were reduced using custom routines. Aperture photometry was done after image subtraction using two custom modifications of the ISIS algorithm (Alard & Lupton 1998), `hotpants`[8] and `mkdifflc` (Gal-Yam et al. 2004, 2008). The two reductions gave consistent results. Errors were estimated by first placing artificial sources of the same brightness and at the same distance from the galaxy center as the SN and then measuring the scatter in measured magnitudes. Finally, the zero point was calibrated with reference magnitudes of stars from the Sloan Digital Sky Survey (Adelman-McCarthy et al. 2007).

We triggered Target of Opportunity observations to obtain spectra with the Double Beam Spectrograph (Oke & Gunn 1982) on the Hale 200 inch (5 m) telescope. Two spectra were obtained around maximum light (UT 2007 March 29 and March 30) and a third a fortnight later (April 13). Spectra were taken using the red grating 158/7500, blue grating 300/3990, and a dichroic to split the light at 5500 Å. This gave us a total wavelength coverage of 3800–9000 Å and dispersion of 4.9

[1] Astronomy Department, California Institute of Technology, 105-24, Pasadena, CA 91125; mansi@astro.caltech.edu.
[2] George Ellory Hale Fellow, Gordon and Betty Moore Foundation.
[3] Department of Astronomy and Astrophysics, Pennsylvania State University, 525 Davey Laboratory, University Park, PA 16802.
[4] Space Radiation Laboratory, California Institute of Technology, MS 220-47, Pasadena, CA 91125.
[5] Kavli Institute for Theoretical Physics and Department of Physics, Kohn Hall, University of California, Santa Barbara, CA 93106.
[6] Steward Observatory, 933 North Cherry Avenue, Tucson, AZ 85721.
[7] Department of Physics and Astronomy, Clemson University, 118 Kinard Laboratory, Clemson, SC 29634.

[8] See http://www.astro.washington.edu/becker/hotpants.html.

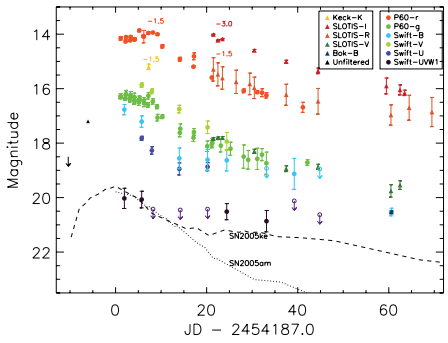

FIG. 1.—Multiband light curve of SN 2007ax based on data from P60, *Swift* UVOT, SLOTIS, Bok, and Keck II NIRC2. Unfiltered magnitudes from Arbour (2007). Note that similarly to subluminous SN 2005ke (*dashed line*), SN 2007ax also appears to show an excess in UV emission at $t > 20$ days while typical SNe Ia (SN 2005am; *dotted line*) continue to decline.

and 2.1 Å pixel^{-1} on the red and blue side, respectively. Data were reduced using the standard IRAF[9] package `apall`.

We triggered *Swift* Target of Opportunity observations for SN 2007ax starting UT 2007 March 29.84 and obtained eight epochs of roughly 5 ks each distributed between the *uvw*2, *uvm*2, *uvw*1, *u*, *b*, and *v* bands. We also obtained a reference image over 8 months after peak to subtract galaxy light. Aperture photometry was performed using a 3″ circular radius. To estimate the galaxy brightness at this location, a 3″ aperture at the supernova position in the reference image was used. Poole et al. (2008) photometric zero points were applied after appropriately scaling for aperture size. For consistency with calibration, a 5″ aperture was used in the computation of coincidence loss. The supernova is detected in *uvw*1 in four epochs, and not detected in the *uvw*2 and *uvm*2 filters. The *b*-band light curve was independently reduced using image subtraction with consistent results. We note that due to the faintness of the supernova and brightness of galaxy background, coincidence loss is dominated by the galaxy light and not a point source, possibly introducing a systematic error in the Swift *u*, *b*, and *v* bands.

Further late-time *BVRI* observations were obtained using the SLOTIS and Bok telescopes and light curves were obtained using image subtraction based on ISIS and IRAF routines. We also obtained near-infrared K' imaging using the Keck NIRC2 instrument with Natural Guide Star adaptive optics on UT 2007 April 4.

[9] IRAF is distributed by the National Optical Astronomy Observatories, which are operated by the Association of Universities for Research in Astronomy, Inc., under cooperative agreement with the National Science Foundation.

3. ANALYSIS

We present analysis of the optical and ultraviolet light curve and optical spectrum of SN 2007ax below. We also compare it to other subluminous SN Ia. We adopt a distance modulus of 32.2 (B. Tully 2007, private communication)[10] to NGC 2577.

3.1. *Optical Light Curve*

We plot the multiband light curve of SN 2007ax in Figure 1. The key characteristic of SN 2007ax is its rapid decline. Traditionally, Δm_{15} (the difference between the peak *B* magnitude and the *B* magnitude 15 days after the peak) has been used to parameterize the decline of the light curve. However, this parameter can be misleading when applied to the faint SNe Ia because the knee in their light curve (transition from fast initial decline to slow late-time decline) is sooner than 15 days from the peak. Therefore, we choose to compare the light curves of subluminous Ia using three parameters first introduced by Pskovskii (1984): initial slope (β), late-time slope (γ), and the time of intersection of the two slopes (t_b). This time of intersection parameter (defined from maximum in *B* magnitude) was also used by Hamuy et al. (1996) as t_2^B and shown to be empirically proportional to Δm_{15} for some SNe Ia.

For the subclass of faint SNe Ia, we find that t_b is better correlated with the peak absolute *B* magnitude than the β and γ slopes of the *B*-band light curve. We fit an empirical relation to the intersection time as a function of peak absolute magnitude and find that $M_B = -13.7(\pm 0.5) - 0.22(\pm 0.03) \times t_b$. Moreover, this transition to slower decline should represent the time at which the optical depth to thermalized radiation becomes thin. We report these three parameters for a sample of subluminous SNe Ia in Table 1 and show the linear fits in Figure 2.

Another crucial property of subluminous SNe Ia is that the fainter they are, the redder they are at maximum. We find that SN 2007ax is consistent within uncertainties of the empirical relation derived first by Garnavich et al. (2004): $M_B = -18.7 + (B - V)_{\max} \times 2.68(\pm 0.32)$. This relation predicts a color in the range of 1.0–1.3 mag and we observe 1.2 ± 0.1 mag. This color has been derived based on synthetic photometry of the spectra around maximum.

3.2. *Ultraviolet Light Curve*

In Figure 1, we compare the *Swift* UVOT light curve of SN 2007ax to another subluminous SN Ia 2005ke (Immler et al. 2006) and a typical SN Ia 2005am (Brown et al. 2005). The key similarity between SN 2005ke and SN 2007ax is that both

[10] Extragalactic Distance Database, http://edd.ifa.hawaii.edu/.

TABLE 1
COMPARISON OF FAINT SNe Ia

Supernova	Galaxy	DM	$M_{B,\max}$ (mag)	α (mag day^{-1})	β (mag day^{-1})	t_b (days)	$(B-V)_{\max}$ (mag)	Reference
SN 2007ax	NGC 2577	32.2	-15.9 ± 0.2	0.16	0.04	10.3	1.2	This Letter
SN 1991bg	NGC 4374	31.2	-16.6 ± 0.3	0.16	0.03	14.8	0.8	Leibundgut et al. (1993), Filippenko et al. (1992)
SN 1998de	NGC 252	34.3	-16.8 ± 0.2	0.18	0.03	14.5	0.7	Modjaz et al. (2001)
SN 2005ke	NGC 1371	31.8	-17.0 ± 0.2	0.15	0.02	14.9	0.7	Immler et al. (2006)
SN 2005bl	NGC 4070	35.1	-17.2 ± 0.2	0.18	0.03	14.0	0.6	Taubenberger et al. (2008)
SN 1999by	NGC 2841	30.9	-17.3 ± 0.2	0.18	0.02	16.0	0.5	Garnavich et al. (2004)

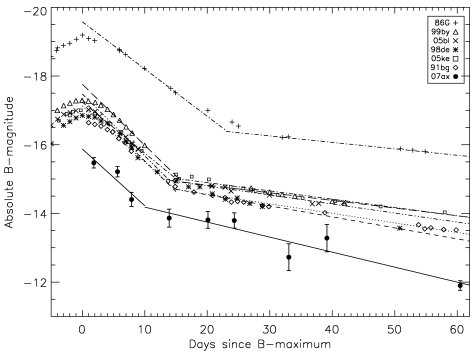

FIG. 2.—*B*-band light curve of SN 2007ax in comparison with other subluminous SNe Ia. The best linear fits are overplotted and give the early-time and late-time slopes. We note that the time of intersection t_b of the early-time and late-time slopes is more strongly correlated with the absolute magnitude than the slopes, α and β.

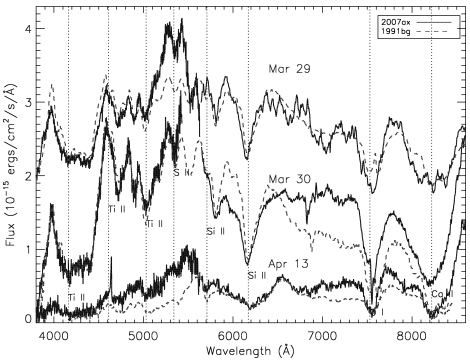

FIG. 3.—Three epochs of P200 DBSP spectra of SN 2007ax (with arbitrary vertical offsets for clarity). Overplotted is another subluminous Type Ia supernova, SN 1991bg, 1 day, 2 days, and 16 days after the peak (scaled by a multiplicative factor for comparison). [*See the electronic edition of the Journal for a color version of this figure.*]

show an excess in UV starting ≈20 days after the peak. Immler et al. (2006) propose that SN 2005ke showed a UV excess due to circumstellar interaction. Perhaps, subluminous supernovae are optically thin below 3800 Å simply due to lower production of iron-group elements. The question of whether UV excess is a more general property of faint SNe Ia merits further investigation with timely follow-up of a larger sample. With a larger sample, one could also consider whether the break in the UV light curve also depends on absolute magnitude.

3.3. *Spectral Evolution*

We compare optical spectra of SN 2007ax to SN 1991bg in Figure 3. The prominent absorption features are Ti II, O I, Si II, and Ca I. The presence of intermediate-mass elements like oxygen and titanium is indicative of the presence of unburned material or a low burning efficiency. The absorption features become broader as the supernova evolves. Comparing our spectra to SN 1991bg 1 day, 2 days, and 16 days after maximum in *B* band, we find that the spectra are very similar. In the first epoch, we see a hint of carbon in the small bump immediately redward of the Si II feature at 6150 Å. However, the signal-to-noise ratio in the spectrum is too low for any conclusive evidence.

Using the technique described by Nugent et al. (1995) we estimate the temperature diagnostic R(Si II)—the ratio of the depths of the two Si II features at 5800 and 6150 Å—to be 0.33. This is smaller than what is implied by the empirical relations derived by Garnavich et al. (2004) and Taubenberger et al. (2008).

We also measure the velocity of the Si II 6150 Å line in the two epochs around maximum and we obtain 9300 and 8800 km s^{-1}. This is consistent with lower velocities observed in other faint SNe Ia (Benetti et al. 2005).

3.4. *NIR Imaging and Extinction*

We measure a K' magnitude of 16.7 ± 0.1 on UT 2007 April 4. We determined the contribution of galaxy light at the supernova position by fitting a Sérsic profile to the galaxy using GALFIT (Peng et al. 2002). The best-fit parameters are a Sérsic index of 1.90, axis ratio of 0.60, effective radius of 4.98″, position angle of 105.6°, and diskiness of −0.14. We find no evidence of dust lanes in this image, suggesting that the host extinction is minimal. This is also consistent with the absence of the interstellar Na D line at 5893 Å. We compute an upper limit on the equivalent width as 0.1 Å. Using the relations derived in Turatto et al. (2003) we get an upper limit of $E(B-V) < 0.01$ mag on the extinction.

Based on the Galactic $l = 201.1°$, $b = 29.6°$, the extinction along the line of sight is $E(B-V) = 0.054$ mag (Schlegel et al. 1998). Therefore, we account for $A_B = 0.23$ and $A_v = 0.18$ in our calculations of absolute magnitude and luminosities.

3.5. *Bolometric Luminosity and* ^{56}Ni *Mass*

Arnett et al. (1985) gives an estimate of the ^{56}Ni mass in the ejecta using the peak bolometric luminosity and the rise time:

$$M_{\rm Ni} = L_{43}[6.31\exp(-t_r/8.8) + 1.43\exp(-t_r/111)]^{-1}.$$

For SN 2007ax, the extinction-corrected peak bolometric luminosity is 2.3×10^{42} ergs s^{-1}. We estimate this by using the photometric points to calibrate our spectrum near maximum light and integrating. The rise time is unknown and unfortunately the literature somewhat arbitrarily assumes 17 days for faint SNe Ia and 19.5 days for typical SNe Ia. Recently, Taubenberger et al. (2008) used SN 1999by early-time data to estimate a rise time of 14 days. The only observational constraint we have for SN 2007ax is that the rise time is longer than 6 days. Thus, for the range of rise times from 6 to 14 days, we find a ^{56}Ni mass of 0.05–0.09 $M_\odot$. This is consistent with other techniques for estimating ^{56}Ni of faint SNe Ia—for SN 1991bg, Cappellaro et al. (1997) model the *V*-band light curve and obtain a mass of 0.1 $M_\odot$, and Mazzali et al. (1997) model the photospheric and nebular-epoch spectra and obtain a ^{56}Ni mass of 0.07 $M_\odot$.

4. DISCUSSION

To summarize, the primary observational characteristics of subluminous SNe Ia (of which SN 2007ax is an extreme case) are small t_b in the optical *B*-band light curve, extremely red $B-V$ color at maximum, possible excess in UV emission at late time, presence of intermediate-mass elements in spectra,

medium ejecta velocities, low ^{56}Ni mass in ejecta, and short rise times.

Several theoretical models have been proposed to explain faint SNe Ia: complete detonation of a sub-Chandrashekhar-mass white dwarf, a delayed detonation model, a failed neutron star model, and a small-scale deflagration model. The detonation of a sub-Chandrashekhar C-O white dwarf (e.g., Livne 1990; Woosley & Weaver 1994) produces more ^{56}Ni than observed and is more blue at maximum than observed (Hoeflich & Khokhlov 1996). If we consider detonation of a sub-Chandrashekhar O-Ne-Mg white dwarf (Isern et al. 1991), the total nuclear energy is smaller and the predicted ejecta velocities are lower than observed (Filippenko et al. 1992). Mazzali et al. (2007) use detailed spectral modeling to show a common explosion mechanism for all SNe Ia, likely delayed detonation. The failed neutron star model (Nomoto & Iben 1985) suggests that if the accretion rate of carbon and oxygen from a companion onto a white dwarf is high enough, it may prematurely ignite CO on the white dwarf surface. Thus, instead of a neutron star, we may see a faint SNe Ia. Small-scale deflagration models suggest that either the burning is restricted to the outer layers or that it occurs slowly.

Another intriguing theoretical possibility recently proposed by Bildsten et al. (2007) is faint thermonuclear supernovae from ultracompact double degenerate AM CVn systems. This supernova is tantalizingly at the brightest end of their predictions ($M_V = -14$ to -16, timescale = 2–6 days, $M_{ej} < 0.1\ M_\odot$). However, the decay time predicted by these models is much shorter and the ^{56}Ni mass less than that observed in SN 2007ax. Also, the spectrum does not show any feature which suggests being powered by different radioactive material (^{48}Cr, ^{44}Ti, ^{52}Fe) produced by some of these models.

None of the above models convincingly explain all the observed characteristics of subluminous SNe Ia. SN 2007ax compels the question of what is the (and whether there is a) lower limit of ^{56}Ni mass in a thermonuclear explosion. Only if we can explain the extremely faint (and the extremely bright) supernovae will we thoroughly understand the limitations in physical processes involved in the thermonuclear explosion, in particular, the ^{56}Ni mass production.

Future supernova surveys which have a shorter cadence and a deeper limiting magnitude will provide invaluable clues to understanding the nature of subluminous SNe Ia. Follow-up of these supernovae with well-sampled UV light curves and well-calibrated multiepoch UV spectra would also be important to understand the apparent excess at late time.

We suggest how a near-future survey, for example, the Palomar Transient Factory,[11] can systematically search for faint SNe Ia. The parameters of the survey design are sky coverage, cadence, depth, filter, and choice of pointings. Howell (2001) shows that faint SNe Ia occur preferentially in early-type galaxies and Taubenberger et al. (2008) suggest that they occur in lower metallicity, old stellar mass populations. Since they decline by a magnitude in 5 days, the cadence of the search should be faster than 5 days so that the detection sample is complete. Since faint SNe Ia are extremely red at maximum, we should choose a red filter for the search. To maximize sky coverage, searching with a single red filter should suffice (with multiband follow-up). Since the local universe is clumpy (e.g., ≈25% of the total light at the distance of Virgo is in the Virgo supercluster), the sky coverage must include concentrations in stellar mass, such as the Virgo, Perseus, and Coma galaxy clusters. The rate of normal SNe Ia is 3 per $10^{11}\ L_\odot$ per century (Scannapieco & Bildsten 2005). Li et al. (2001) estimate a rate for subluminous SNe Ia to be 16% of the normal SNe Ia rate based on the LOSS and BAOSS surveys. To a depth of absolute magnitude of -15.5, and with a limiting magnitude of 20.5, the survey volume would be 1.5×10^7 Mpc^3. Using the 2MASS K-band luminosity function of $5.1 \times 10^8\ L_\odot$ Mpc^{-3} (Karachentsev & Kutkin 2005; Kochanek et al. 2001), we expect a rate of the faintest subluminous supernovae to be ≈370 all sky per year. The Palomar Transient Factory plans a 5 day cadence 2700 deg^2 experiment which would give ≈24 faint SNe Ia per year.

We thank Nick Scoville, Milan Bogoslavejic, and the *Swift* team for performing our Target of Opportunity observations flawlessly. We would like to thank Brent Tully for providing his catalog of nearby galaxies. L. B. acknowledges NSF grants PHY 05-51164 and AST 07-07633. Some of the data presented herein were obtained at the W. M. Keck Observatory, which is operated as a scientific partnership among the California Institute of Technology, the University of California, and the National Aeronautics and Space Administration. The Observatory was made possible by the generous financial support of the W. M. Keck Foundation.

Facilities: PO:1.5m, Hale (DBSP), Keck:I (LRIS), Keck:II (NIRC2), Swift (UVOT), Bok

[11] The Palomar Transient Factory is a dedicated time-domain astronomy project to come online on the Palomar 48 inch in 2008 November.

REFERENCES

Adelman-McCarthy, J. K., et al. 2007, ApJS, 172, 634
Alard, C., & Lupton, R. H. 1998, ApJ, 503, 325
Arbour, R. 2007, CBET, 904, 1
Arnett, W. D., Branch, D., & Wheeler, J. C. 1985, Nature, 314, 337
Benetti, S., et al. 2005, ApJ, 623, 1011
Bildsten, L., et al. 2007, ApJ, 662, L95
Blondin, S., et al. 2007, CBET, 907, 1
Brown, P. J., et al. 2005, ApJ, 635, 1192
Cappellaro, E., et al. 1997, A&A, 328, 203
Cenko, S. B., et al. 2006, PASP, 118, 1396
Filippenko, A. V., et al. 1992, AJ, 104, 1543
Gal-Yam, A., et al. 2004, ApJ, 609, L59
———. 2008, ApJ, 680, 550
Garnavich, P. M., et al. 2004, ApJ, 613, 1120
Hamuy, M., et al. 1996, AJ, 112, 2438
Hoeflich, P., & Khokhlov, A. 1996, ApJ, 457, 500
Howell, D. A. 2001, ApJ, 554, L193
Immler, S., et al. 2006, ApJ, 648, L119
Isern, J., Canal, R., & Labay, J. 1991, ApJ, 372, L83
Karachentsev, I. D., & Kutkin, A. M. 2005, Astron. Lett., 31, 299
Kochanek, C. S., et al. 2001, ApJ, 560, 566
Leibundgut, B., et al. 1993, AJ, 105, 301
Li, W., et al. 2001, ApJ, 546, 734
Livne, E. 1990, ApJ, 354, L53
Mazzali, P. A., et al. 1997, MNRAS, 284, 151
———. 2007, Science, 315, 825
Modjaz, M., et al. 2001, PASP, 113, 308
Morrell, N., & Folatelli, G. 2007, CBET, 908, 1
Nomoto, K., & Iben, I., Jr. 1985, ApJ, 297, 531
Nugent, P., et al. 1995, ApJ, 455, L147
Oke, J. B., & Gunn, J. E. 1982, PASP, 94, 586
Peng, C. Y., Ho, L. C., Impey, C. D., & Rix, H.-W. 2002, AJ, 124, 266
Poole, T. S., et al. 2008, MNRAS, 383, 627P
Pskovskii, Y. P. 1984, Soviet Astron., 28, 658
Scannapieco, E., & Bildsten, L. 2005, ApJ, 629, L85
Schlegel, D. J., Finkbeiner, D. P., & Davis, M. 1998, ApJ, 500, 525
Taubenberger, S., et al. 2008, MNRAS, 385, 75
Turatto, M., Benetti, S., & Cappellaro, E. 2003, in From Twilight to Highlight: The Physics of Supernovae, ed. W. Hillebrandt & B. Leibundgut (Berlin: Springer), 200
Woosley, S. E., & Weaver, T. A. 1994, ApJ, 423, 371

Appendix D

AN EXTREMELY LUMINOUS X-RAY OUTBURST AT THE BIRTH OF A SUPERNOVA

The following was published in *Nature* (2008, May 22)

Vol 453|22 May 2008|doi:10.1038/nature06997

ARTICLES

An extremely luminous X-ray outburst at the birth of a supernova

A. M. Soderberg[1,2], E. Berger[1,2], K. L. Page[3], P. Schady[4], J. Parrent[5], D. Pooley[6], X.-Y. Wang[7], E. O. Ofek[8], A. Cucchiara[9], A. Rau[8], E. Waxman[10], J. D. Simon[8], D. C.-J. Bock[11], P. A. Milne[12], M. J. Page[4], J. C. Barentine[13], S. D. Barthelmy[14], A. P. Beardmore[3], M. F. Bietenholz[15,16], P. Brown[9], A. Burrows[1], D. N. Burrows[9], G. Byrngelson[17], S. B. Cenko[18], P. Chandra[19], J. R. Cummings[20], D. B. Fox[9], A. Gal-Yam[10], N. Gehrels[20], S. Immler[20], M. Kasliwal[8], A. K. H. Kong[21], H. A. Krimm[20,22], S. R. Kulkarni[8], T. J. Maccarone[23], P. Mészáros[9], E. Nakar[24], P. T. O'Brien[3], R. A. Overzier[25], M. de Pasquale[4], J. Racusin[9], N. Rea[26] & D. G. York[27]

Massive stars end their short lives in spectacular explosions—supernovae—that synthesize new elements and drive galaxy evolution. Historically, supernovae were discovered mainly through their 'delayed' optical light (some days after the burst of neutrinos that marks the actual event), preventing observations in the first moments following the explosion. As a result, the progenitors of some supernovae and the events leading up to their violent demise remain intensely debated. Here we report the serendipitous discovery of a supernova at the time of the explosion, marked by an extremely luminous X-ray outburst. We attribute the outburst to the 'break-out' of the supernova shock wave from the progenitor star, and show that the inferred rate of such events agrees with that of all core-collapse supernovae. We predict that future wide-field X-ray surveys will catch each year hundreds of supernovae in the act of exploding.

Stars more massive than about eight times the mass of the Sun meet their death in cataclysmic explosions termed supernovae. These explosions give birth to the most extreme compact objects—neutron stars and black holes—and enrich their environments with heavy elements. It is generally accepted that supernovae are triggered when the stellar core runs out of fuel for nuclear burning and thus collapses under its own gravity (see ref. 1 and references therein). As the collapsing core rebounds, it generates a shock wave that propagates through, and explodes, the star.

The resulting explosion ejects several solar masses of stellar material with a mean velocity[2] of about 10^4 km s^{-1}, or a kinetic energy of about 10^{51} erg. Less than a solar mass of ^{56}Ni is synthesized in the explosion, but its subsequent radioactive decay powers[1] the luminous optical light observed to peak 1–3 weeks after the explosion. It is through this delayed signature that supernovae have been discovered both historically and in modern searches.

Although the general picture of core collapse has been recognized for many years, the details of the explosion remain unclear and most supernova simulations fail to produce an explosion. The gaps in our understanding are due to the absence of detailed observations in the first days after the explosion, and the related difficulty in detecting the weak neutrino[3] and gravitational wave signatures of the explosion. These signals offer a direct view of the explosion mechanism but require the discovery of supernovae at the time of explosion.

In this Article we describe our serendipitous discovery of an extremely luminous X-ray outburst that marks the birth of a supernova of type Ibc. Prompt bursts of X-ray and/or ultraviolet emission have been theorized[4,5] to accompany the break-out of the supernova shock wave through the stellar surface, but their short durations (just seconds to hours) and the lack of sensitive wide-field X-ray and ultraviolet searches have prevented their discovery until now.

Our detection enables an unprecedented early and detailed view of the supernova, allowing us to infer[6] the radius of the progenitor star, its mass loss in the final hours before the explosion, and the speed of the shock as it explodes the star. Drawing on optical, ultraviolet, radio and X-ray observations, we show that the progenitor was compact (radius $R_* \approx 10^{11}$ cm) and stripped of its outer hydrogen envelope by a strong and steady stellar wind. These properties are consistent[7] with those of Wolf-Rayet stars, the favoured[8] progenitors of type Ibc supernovae.

Wolf-Rayet stars are also argued[9] to give rise to γ-ray bursts (GRBs), a related but rare class of explosions characterized by highly collimated relativistic jets. Our observations, however, indicate an ordinary spherical and non-relativistic explosion and we firmly rule out a GRB connection.

[1]Department of Astrophysical Sciences, Princeton University, Ivy Lane, Princeton, New Jersey 08544, USA. [2]Carnegie Observatories, 813 Santa Barbara Street, Pasadena, California 91101, USA. [3]Department of Physics and Astronomy, University of Leicester, Leicester LE1 7RH, UK. [4]Mullard Space Science Laboratory, University College London, Holmbury St Mary, Dorking, Surrey RH5 6NT, UK. [5]Physics and Astronomy Department, Dartmouth College, Hanover, New Hampshire 03755, USA. [6]Astronomy Department, University of Wisconsin, 475 North Charter Street, Madison, Wisconsin 53706, USA. [7]Department of Astronomy, Nanjing University, Nanjing 210093, China. [8]Department of Astronomy, 105-24, California Institute of Technology, Pasadena, California 91125, USA. [9]Department of Astronomy and Astrophysics, Pennsylvania State University, University Park, Pennsylvania 16802, USA. [10]Faculty of Physics, Weizmann Institute of Science, Rehovot 76100, Israel. [11]Radio Astronomy Laboratory, University of California, Berkeley, California 94720, USA. [12]Steward Observatory, University of Arizona, 933 North Cherry Avenue, Tucson, Arizona 85721, USA. [13]Department of Astronomy, University of Texas at Austin, Austin, Texas 78712, USA. [14]NASA Goddard Space Flight Center, Greenbelt, Maryland 20771, USA. [15]Department of Physics and Astronomy, York University, Toronto, Ontario M3J 1P3, Canada. [16]Hartebeestehoek Radio Observatory, PO Box 443, Krugersdorp, 1740, South Africa. [17]Department of Physics and Astronomy, Clemson University, Clemson, South Carolina 29634, USA. [18]Space Radiation Laboratory, 220-47, California Institute of Technology, Pasadena, California 91125, USA. [19]Department of Astronomy, University of Virginia, PO Box 400325, Charlottesville, Virginia 22904, USA. [20]CRESST and NASA Goddard Space Flight Center, Greenbelt, Maryland 20771, USA. [21]Institute of Astronomy and Department of Physics, National Tsing Hua University, Hsinchu, Taiwan. [22]Universities Space Research Association, 10211 Wincopin Circle, #500, Columbia, Maryland 21044, USA. [23]School of Physics and Astronomy, University of Southampton, Southampton SO17 1BJ, UK. [24]Theoretical Astrophysics, 130-33, California Institute of Technology, Pasadena, California 91125, USA. [25]Max-Planck-Institut für Astrophysik, D-85748 Garching, Germany. [26]University of Amsterdam, Astronomical Institute 'Anton Pannekoek', Kruislaan 403, 1098SJ, Amsterdam, The Netherlands. [27]Department of Astronomy and Astrophysics, University of Chicago, 5640 S. Ellis Avenue, Chicago, Illinois 60637, USA.

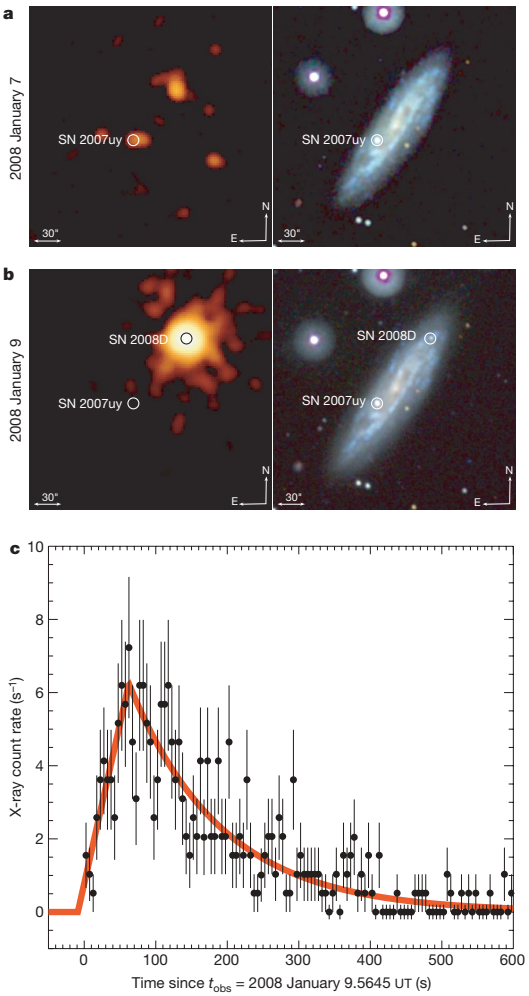

Figure 1 | Discovery image and X-ray light curve of XRO 080109/SN 2008D. a, X-ray (left) and ultraviolet (right) images of the field obtained on 2008 January 7 UT during Swift observations of the type Ibc supernova 2007uy. No source is detected at the position of SN 2008D to a limit of $\lesssim 10^{-3}$ counts s^{-1} in the X-ray band and $U \gtrsim 20.3$ mag. **b**, Repeated ultraviolet and X-ray observations of the field from January 9 UT during which we serendipitously discovered XRO 080109 and its ultraviolet counterpart. The position of XRO 080109 is right ascension $\alpha = 09\,\mathrm{h}\,09\,\mathrm{min}\,30.70\,\mathrm{s}$, declination $\delta = 33^\circ\,08'\,19.1''$ (J2000) ($\pm 3.5''$), about 9 kpc from the centre of NGC 2770. **c**, X-ray light curve of XRO 080109 in the 0.3–10 keV band. The data were accumulated in the photon counting mode and were processed using version 2.8 of the Swift software package, including the most recent calibration and exposure maps. The high count rate resulted in photon pile-up, which we correct for by fitting a King function profile to the point spread function (PSF) to determine the radial point at which the measured PSF deviates from the model. The counts were extracted using an annular aperture that excluded the affected 4 pixel core of the PSF, and the count rate was corrected according to the model. Error bars, $\pm 1\sigma$. Using a fast rise, exponential decay model (red curve), we determine the properties of the outburst, in particular its onset time, t_0, which corresponds to the explosion time of SN 2008D. The best-fit parameters are a peak time of 63 ± 7 s after the beginning of the observation, an e-folding time of 129 ± 6 s, and peak count rate of 6.2 ± 0.4 counts s^{-1} (90% confidence level using Cash statistics). The best-fit value of t_0 is January 9 13:32:40 UT (that is, 9 s before the start of the observation) with a 90% uncertainty range of 13:32:20 to 13:32:48 UT.

Most importantly, the inferred rate of X-ray outbursts indicates that all core-collapse supernovae produce detectable shock break-out emission. Thus, we predict that future wide-field X-ray surveys will uncover hundreds of supernovae each year at the time of explosion, providing the long-awaited temporal and positional triggers for neutrino and gravitational wave searches.

Discovery of the X-ray outburst

On 2008 January 9 at 13:32:49 UT, we serendipitously discovered an extremely bright X-ray transient during a scheduled Swift X-ray Telescope (XRT) observation of the galaxy NGC 2770 (distance $d = 27$ Mpc). Previous XRT observations of the field just two days earlier revealed no pre-existing source at this location. The transient, hereafter designated as X-ray outburst (XRO) 080109, lasted about 400 s, and was coincident with one of the galaxy's spiral arms (Fig. 1). From observations described below, we determine that XRO 080109 is indeed located in NGC 2770, and we thus adopt this association from here on.

The temporal evolution is characterized by a fast rise and exponential decay, often observed for a variety of X-ray flare phenomena (Fig. 1). We determine the onset of the X-ray emission to be 9^{+20}_{-8} s before the beginning of the observation, implying an outburst start time (t_0) of January 9.5644 UT. The X-ray spectrum is best fitted by a power law ($N(E) \propto E^{-\Gamma}$, where N and E are the photon number and energy, respectively) with a photon index of $\Gamma = 2.3 \pm 0.3$, and a hydrogen column density of $N_{\mathrm{H}} = 6.9^{+1.8}_{-1.5} \times 10^{21}$ cm^{-2}, in excess of the absorption within the Milky Way (see Supplementary Information). The inferred unabsorbed peak flux is $F_{\mathrm{X,p}} \approx 6.9 \times 10^{-10}$ erg cm^{-2} s^{-1} (0.3–10 keV). We also measure significant spectral softening during the outburst.

The XRO was in the field of view of the Swift Burst Alert Telescope (BAT; 15–150 keV) beginning 30 min before and continuing throughout the outburst, but no γ-ray counterpart was detected. Thus, the outburst was not a GRB (see also Supplementary Information). Integrating over the duration of the outburst, we place a limit on the γ-ray fluence of $f_\gamma \lesssim 8 \times 10^{-8}$ erg cm^{-2} (3σ), a factor of three times higher than an extrapolation of the X-ray spectrum to the BAT energy band.

The total energy of the outburst is thus $E_{\mathrm{X}} \approx 2 \times 10^{46}$ erg, at least three orders of magnitude lower[10] than GRBs. The peak luminosity is $L_{\mathrm{X,p}} \approx 6.1 \times 10^{43}$ erg s^{-1}, several orders of magnitude larger than the Eddington luminosity (the maximum luminosity for a spherically accreting source) of a solar mass object, outbursts from ultra-luminous X-ray sources and type I X-ray bursts. In summary, the properties of XRO 080109 are distinct from those of all known X-ray transients.

The birth of a supernova

Simultaneous observations of the field with the co-aligned Ultraviolet/Optical Telescope (UVOT) on board Swift showed no evidence for a contemporaneous counterpart. However, UVOT observations just 1.4 h after the outburst revealed[11] a brightening ultraviolet/optical counterpart. Subsequent ground-based optical observations also uncovered[11–13] a coincident source.

We promptly obtained optical spectroscopy of the counterpart with the Gemini North 8-m telescope beginning 1.74 d after the outburst (Fig. 2). The spectrum is characterized by a smooth continuum with narrow absorption lines of Na I (wavelengths 5,890 and 5,896 Å) at the redshift of NGC 2770. More importantly, we note broad absorption features near 5,200 and 5,700 Å and a drop-off beyond 7,000 Å, strongly suggestive of a young supernova. Subsequent observations confirmed these spectral characteristics[11,14], and the transient was classified[11,15] as type Ibc SN 2008D based on the lack of hydrogen and weak silicon features.

Thanks to the prompt X-ray discovery, the temporal coverage of our optical spectra exceeds those of most supernovae, rivalling even the best-studied GRB-associated supernovae, and SN 1987A (Fig. 2). We see a clear evolution from a mostly featureless continuum to broad absorption lines, and finally to strong absorption features with moderate widths. Moreover, our spectra reveal the emergence of

strong He I features within a few days of the outburst (see also ref. 16). Thus, SN 2008D is a He-rich type Ibc supernova, unlike[17] GRB-associated supernovae. Observations at high spectral resolution further reveal significant host galaxy extinction, with $A_V \approx 1.2$–2.5 mag (see Supplementary Information).

The well-sampled ultraviolet/optical light curves in ten broadband filters (2,000–10,000 Å) exhibit two distinct components (Fig. 3). First, an ultraviolet-dominated component that peaks about a day after the X-ray outburst, and which is similar to very early observations[18] of the GRB-associated SN 2006aj. The second component is significantly redder and peaks on a timescale of about 20 d, consistent with observations of all type Ibc supernovae. Accounting for an extinction of $A_V = 1.9$ mag (Fig. 3), the absolute peak brightness of the second component is $M_V \approx -16.7$ mag, at the low end of the distribution[19] for type Ibc supernovae and GRB-associated supernovae.

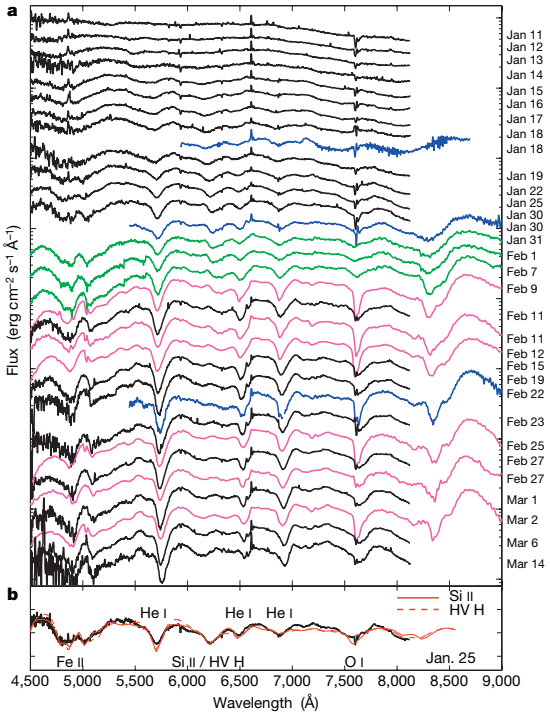

Figure 2 | Optical spectra of XRO 080109/SN 2008D, and model fit. a, The spectra are plotted logarithmically in flux units and shifted for clarity. **b**, A model fit to the January 25 UT spectrum using the spectral fitting code SYNOW. We identify several strong features attributed to He I, O I and Fe II, indicating a type Ibc classification. In addition, we find an absorption feature at 6,200 Å that can be identified as Si II or high velocity H I (HV H; see Supplementary Information for details). The observations were performed using the following facilities: The Gemini Multi-Object Spectrograph (GMOS) on the Gemini North 8-m telescope (black); the Dual Imaging Spectrograph (DIS) on the Apache Point 3.5-m telescope (blue); the Double Spectrograph (DBSP) on the Palomar Hale 200-inch telescope (green); and the Low Resolution Spectrograph (LRS) on the Hobby-Eberly 9.2-m telescope (magenta). The details of the observational set-up and the exposure times are provided in Supplementary Information. The data were reduced using the gemini package within the Image Reduction and Analysis Facility (IRAF) software for the GMOS data. All other observations were reduced using standard packages in IRAF. The supernova spectra were extracted from the two-dimensional data using a nearby background region to reduce the contamination from host galaxy emission. Absolute flux calibration was achieved using observations of the standard stars Feige 34 and G191B2B.

A shock break-out origin

As some type Ibc supernovae harbour GRBs, we investigate the possibility that the XRO is produced by a relativistic outflow. In this scenario, the X-ray flux and simultaneous upper limits in the ultraviolet/optical require the outflow to be ultra-relativistic with a bulk Lorentz factor $\gamma \approx 90$, but its radius to be only $R \approx 10^{10}$ cm; here $\gamma \equiv (1-\beta^2)^{-1/2}$ and $\beta \equiv v/c$, where v is the outflow velocity and c is the speed of light. However, given the observed duration of the outburst, we expect[20] $R \approx 4\gamma^2 ct \approx 10^{17}$ cm, indicating that the relativistic outflow scenario is not self-consistent (see Supplementary Information for details).

We are left with a trans- or non-relativistic origin for the outburst, and we consider supernova shock break-out as a natural scenario. The break-out is defined by the transition from a radiation-mediated to a collisional (or collisionless[21]) shock as the optical depth of the outflow decreases to unity. Such a transition has long been predicted[4,5] to produce strong, thermal ultraviolet/X-ray emission at

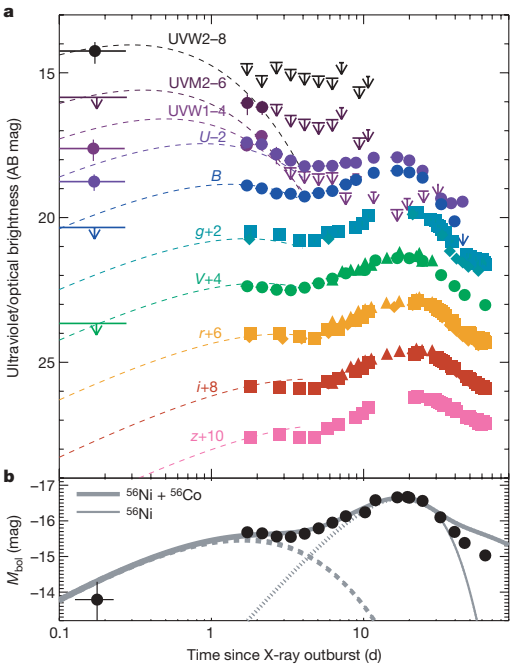

Figure 3 | Optical and ultraviolet light curves of XRO 080109/SN 2008D, and model fit. a, Optical and ultraviolet light curves. Data are from Swift UVOT (circles), Palomar 60-inch telescope (squares), Gemini/GMOS (diamonds), and the SLOTIS telescope (triangles). Tables summarizing the observations and data analysis are available in Supplementary Information. The data have not been corrected for host galaxy extinction and have been offset (as labelled) for clarity. We fit the data before 3 d with a cooling envelope blackbody emission model[6] (dashed lines) that accounts for host extinction (A_V). We find a reasonable fit to the data with $R_* \approx 10^{11}$ cm, $E_K \approx 2 \times 10^{51}$ erg, $M_{ej} \approx 5\,M_\odot$ and $A_V \approx 1.9$ mag, consistent with the constraints from the high-resolution optical spectrum. The radius and temperature of the photosphere at 1 d are $R_{ph} \approx 3 \times 10^{14}$ cm and $T_{ph} \approx 10^4$ K, respectively. Error bars are 1σ; down-pointing arrows are upper limits (3σ). **b**, The absolute bolometric magnitude light curve (corrected for host extinction). The dashed lines are the same cooling envelope model described above, while the short-dashed lines are models of supernova emission powered by radioactive decay. The solid lines are combined models taking into account the decay of ^{56}Ni (thin line) and ^{56}Ni+^{56}Co (thick line). The supernova models provide an independent measure of E_K and M_{ej}, as well as M_{Ni} (see Supplementary Information for a detailed discussion of the models). We find values that are consistent to within 30% with those inferred from the cooling envelope model.

the time of explosion. A non-thermal component at higher energies may be produced[22] by multiple scatterings of the photons between the ejecta and a dense circumstellar medium (bulk comptonization).

We attribute the observed non-thermal outburst to comptonized emission from shock break-out, indicating that the associated thermal component must lie below the XRT low energy cut-off, ~0.1 keV. With the reasonable assumption that the energy in the thermal ($E_{\rm th}$) and comptonized components is comparable, we constrain[6] the radius at which shock break-out occurs to $R_{\rm sbo} \gtrsim 7\times10^{11}(T)^{-4/7}(E_{\rm X})^{3/7}$ cm (here T is in units of 0.1 keV, and $E_{\rm X}$ in units of 2×10^{46} erg). This is consistent with a simple estimate derived from the rise time of the outburst, $R_{\rm sbo} = c\delta t \approx 10^{12}$ cm, and larger than the typical radii of Wolf-Rayet stars[23], ~10^{11} cm. We therefore attribute the delayed shock break-out to the presence of a dense stellar wind, similar[6,18] to the case of the GRB-associated supernova SN 2006aj.

The shock velocity at break-out is[6] $(\gamma\beta) \lesssim 1.1$ and the outflow is thus trans-relativistic, as expected[24] for a compact progenitor. Using these constraints, the inferred optical depth of the ejecta to thermal X-rays is $\tau_{\rm ej} \approx 1.5(E_{\rm X})(R_{\rm sbo})^{-2}(\gamma-1)^{-1} \approx 3$ (here $E_{\rm X}$ is normalized as above, and $R_{\rm sbo}$ is in units of 7×10^{11} cm), and comptonization is thus efficient, confirming our model. Equally important, as the ejecta expand outward the optical depth of the stellar wind decreases and the spectrum of the comptonized emission is expected[22] to soften, in agreement with the observed trend.

The shock break-out emission traces the wind mass-loss rate of the progenitor, $\dot{M}$, in the final hours leading up to the explosion. The inferred density indicates $\dot{M} \approx 4\pi v_{\rm w} R_{\rm sbo}/\kappa \approx 10^{-5}\ M_{\odot}\ {\rm yr}^{-1}$; here $\kappa \approx 0.4\ {\rm cm^2\ g^{-1}}$ is the Thomson opacity for an ionized hydrogen wind and $v_{\rm w} \approx 10^3\ {\rm cm\ s^{-1}}$ is the typical[7] wind velocity for Wolf-Rayet stars. The mass-loss rate is consistent[7] with the average values inferred for Galactic Wolf-Rayet stars, and, along with the inferred compact stellar radius and the lack of hydrogen features, leads us to conclude that the progenitor was a Wolf-Rayet star.

Two ultraviolet/optical emission components

The early ultraviolet/optical emission ($t \lesssim 3$ d, where t is time since t_0) appears to be a distinct component, based on its different temporal behaviour and bluer colours (Fig. 3). We attribute this early emission to cooling of the outer stellar envelope following the passage of the shock through the star and its subsequent break-out (marked by the X-ray outburst). The expected blackbody radiation is characterized[6] by the photospheric radius and temperature, which evolve with t respectively as $R_{\rm ph} \propto t^{0.8}$ and $T_{\rm ph} \propto t^{-0.5}$, and depend on the total ejecta kinetic energy ($E_{\rm K}$) and mass ($M_{\rm ej}$), and on the stellar radius before the explosion (R_*).

The model light curves provide a good fit to the early ultraviolet/optical data (Fig. 3). The implied stellar radius is $R_* \approx 7\times10^{10}$ cm, consistent with that expected[23] for a Wolf-Rayet progenitor. Moreover, this value is smaller than the shock break-out radius, confirming our earlier inference that the break-out occurs in the extended stellar wind.

The ratio of E_K and $M_{\rm ej}$ also determines the shape of the main supernova light curve (see, for example, ref. 25), and the mass of ^{56}Ni synthesized in the explosion ($M_{\rm Ni}$) determines[26] its peak optical luminosity. To break the degeneracy between $E_{\rm K}$ and $M_{\rm ej}$, we measure the photospheric velocity from the optical spectra at maximum light, $v_{\rm ph} = 0.3(E_{\rm K}/M_{\rm ej})^{1/2} \approx 11{,}500\ {\rm km\ s^{-1}}$; this is comparable to that of ordinary type Ibc supernovae, but somewhat slower[17] than GRB-associated supernovae (Fig. 2 and Supplementary Information). We find that both light curve components are self-consistently fitted with $E_{\rm K} \approx (2\text{–}4)\times10^{51}$ erg, $M_{\rm ej} \approx 3\text{–}5\ M_{\odot}$, and $M_{\rm Ni} \approx 0.05\text{–}0.1\ M_{\odot}$ (Fig. 3).

Long-lived X-ray and radio emission

Whereas ultraviolet/optical observations probe the bulk material, radio and X-ray emission trace fast ejecta. Our Swift follow-up observations of the XRO revealed fainter X-ray emission several hours after the explosion, with $L_{\rm X} \approx 2\times10^{40}\ {\rm erg\ s^{-1}}$ ($t \approx 0.2$ d). This emission exceeds the extrapolation of the outburst by many orders of magnitude, indicating that it is powered by a different mechanism. Using a high-angular-resolution observation from the Chandra X-ray Observatory on January 19.86 UT, we detect the supernova with a luminosity $L_{\rm X} = (1.0 \pm 0.3)\times10^{39}\ {\rm erg\ s^{-1}}$ (0.3–10 keV), and further resolve three nearby sources contained within the 18-arcsec resolution element of XRT. Correcting all XRT observations for these sources, we find that the long-lived X-ray emission decays steadily as $F_{\rm X} \propto t^{-0.7}$ (Supplementary Information).

Using the Very Large Array (VLA) on January 12.54 UT, we further discovered a new radio source at the position of the supernova that was not present on January 7 UT. Follow-up observations were obtained at multiple frequencies between 1.4 and 95 GHz using the VLA, the Combined Array for Research in Millimeter-wave Astronomy (CARMA) and the Very Long Baseline Array (VLBA).

The broadband radio emission on January 14 UT reveals a spectral peak, $\nu_{\rm p} \approx 43$ GHz, with a flux density, $F_{\nu,{\rm p}} \approx 4$ mJy, and a low frequency spectrum, $F_\nu \propto \nu^{2.5}$. Subsequent observations show that $\nu_{\rm p}$ cascades to lower frequencies, similar to the evolution observed in other type Ibc supernovae (see, for example, ref. 27). The passage of $\nu_{\rm p}$ through each frequency produces a light curve peak. We measure $F_\nu \propto t^{1.4}$ and $F_\nu \propto t^{-1.2}$ for the light curve rise and decline, respectively (Fig. 4).

We note that our X-ray and radio observations of SN 2008D are the earliest ever obtained for a normal type Ibc supernova. At $t \approx 10$ d, the X-ray and peak radio luminosities are several orders of magnitude lower[28,29] than those of GRB afterglows but comparable[30,31] to those of normal type Ibc supernovae.

The properties of the fast ejecta

Radio synchrotron emission is produced[32] by relativistic electrons accelerated in the supernova shock as they gyrate in the amplified magnetic field. Self-absorption suppresses the spectrum below the peak to $F_\nu \propto \nu^{2.5}$, in excellent agreement with our observations. In this context, we infer[33,34] the radius of the fast ejecta, using the measured $\nu_{\rm p}$ and $L_{\nu,{\rm p}}$, to be $R \approx 3\times10^{15}$ cm at $t \approx 5$ d. The implied mean velocity is $\beta \approx 0.25$, clearly ruling out relativistic ejecta.

With this conclusion there are two possibilities for the ejecta dynamics. First, the supernova may be in free expansion, $R \propto t$, consistent with observations of type Ibc supernovae (see, for example, ref. 27). Alternatively, the ejecta may have been relativistic at early time and then rapidly decelerated, leading to $R \propto t^{2/3}$. In the latter scenario, the dynamics are governed[35] by the Sedov-Taylor solution. As discussed in Supplementary Information, the temporal evolution of the radio light curves is clearly inconsistent with the Sedov-Taylor model, ruling out even early relativistic expansion.

Thus, the radio emission is produced by freely expanding ejecta, indicative of the broad velocity structure expected[24] for ordinary core-collapse supernovae. The standard formulation[27] provides an excellent fit to the data (Fig. 4) and indicates that the energy coupled to fast material is $E_{\rm K,R} \approx 10^{48}$ erg (here subscript K,R indicates kinetic energy probed by radio observations), just 0.1% of the total kinetic energy. Moreover, the inferred density profile is $\rho(r) \propto r^{-2}$ (where r is the radius from the explosion site), as expected for a steady stellar wind. The inferred mass-loss rate, $\dot{M} \approx 7\times10^{-6}\ M_{\odot}\ {\rm yr^{-1}}$, is in agreement with our shock break-out value, indicating a stable mass loss rate in the final ~3 yr to ~3 h of the progenitor's life.

The radio-emitting electrons also account for the late X-ray emission through their inverse Compton (IC) upscattering of the supernova optical photons (with a luminosity $L_{\rm opt}$). The expected[6] X-ray luminosity is $L_{\rm IC} \approx 3\times10^{39}\ (E_{\rm K,R})(L_{\rm opt})(t)^{-2/3}\ {\rm erg\ s^{-1}}$ (where $E_{\rm K,R}$ is units of 10^{48} erg, $L_{\rm opt}$ in $10^{42}\ {\rm erg\ s^{-1}}$, and t in days), in excellent agreement with the observations by XRT and the Chandra X-ray Observatory. We note that the synchrotron contribution in the X-ray band is lower by at least two orders of magnitude.

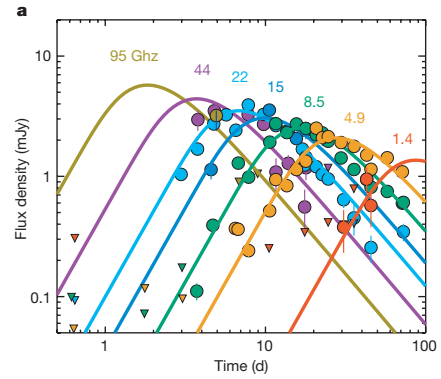

Figure 4 | Radio light curves, spectra and image of XRO 080109/SN 2008D. Radio data from 1.4 to 95 GHz were obtained with the VLA, CARMA and the VLBA (circles are detections and inverted triangles represent 3σ upper limits). Error bars are 1σ. The flux measurements and a description of the data analysis are provided in Supplementary Information. **a**, Radio light curves with a model of synchrotron self-absorbed emission arising[27] from shocked material surrounding the freely expanding supernova. We adopt a shock compression factor of $\eta = 4$ for the post-shock material and assume that the electrons and magnetic fields each contribute 10% to the total post-shock energy density. The best-fit model (solid lines) implies the following physical parameters and temporal evolution: $R \approx 3 \times 10^{15}(t)^{0.9}$ cm, $E_{K,R} \approx 10^{48}(t)^{0.8}$ erg and $B \approx 2.4(t)^{-1}$ G, where B is the magnetic field strength (here t is in units of 5 d). The implied density profile is $\rho(r) \propto r^{-2}$, as expected for the wind from a massive star. **b**, Broadband radio spectra. The spectral peak of the radio synchrotron emission cascades to lower frequencies over the course of our follow-up observations with $\nu_p \propto t^{-1}$. The low frequency turn-over is consistent with expectations for synchrotron self-absorption (grey lines). **c**, Radio image from a VLBA observation on February 8 UT. The colour scale goes from -0.2 mJy per beam (black) to 1.4 mJy per beam (white). We place an upper limit on the angular size of the ejecta of 1.2 mas (3σ), corresponding to a physical radius of $\lesssim 2.4 \times 10^{17}$ cm. This limit is a factor of 16 times larger than, and therefore consistent with, the radius derived from the radio supernova model. However, it places a limit of $(\gamma\beta) \lesssim 3$ on the expansion velocity.

Finally, we note that neither the late X-ray emission nor the radio emission show evidence for a rising component that could be attributed[36] to an off-axis GRB jet spreading into our line of sight. This conclusion is also supported by the unresolved size of the radio supernova from VLBA observations at $t \approx 1$ month, $R \lesssim 2.4 \times 10^{17}$ cm (3σ), which constrains the outflow velocity to be $\gamma\beta \lesssim 3$.

The rate of XROs

To estimate the rate of XROs, we find that the on-sky effective monitoring time of the XRT from the launch of Swift through to the end of January 2008, including only those exposures longer than 300 s, is about two years. Along with the XRT field of view (24 arcmin on a side), the number density of L_* galaxies ($\phi \approx 0.05\ L_*\ \mathrm{Mpc}^{-3}$), and the detectability limit of XRT for events like XRO 080109 ($d \lesssim 200$ Mpc), we infer an XRO rate of $\gtrsim 10^{-3}\ L_*^{-1}\ \mathrm{yr}^{-1}$ (95% confidence level, Fig. 5); here L_* is the characteristic luminosity of galaxies[37]. This rate is at least an order of magnitude larger than for GRBs[38,39]. On the other hand, with a core-collapse supernova rate[40] of $10^{-2}\ L_*\ \mathrm{yr}^{-1}$, the probability of detecting at least one XRO if all such supernovae produce an outburst is about 50%.

We find a similar agreement with the supernova rate using the sensitivity of the BAT. The estimated[39] peak photon flux of the outburst is 0.03 $\mathrm{cm}^{-2}\ \mathrm{s}^{-1}$ (1–1,000 keV), which for a 10^2 s image trigger[41] is detectable to about 20 Mpc. The BAT on-sky monitoring time of 3 yr and the 2 sr field of view thus yield an upper limit on the XRO rate of $\lesssim 10^5\ \mathrm{Gpc}^{-3}\ \mathrm{yr}^{-1}$, consistent with the core-collapse supernova rate[42] of $6 \times 10^4\ \mathrm{Gpc}^{-3}\ \mathrm{yr}^{-1}$.

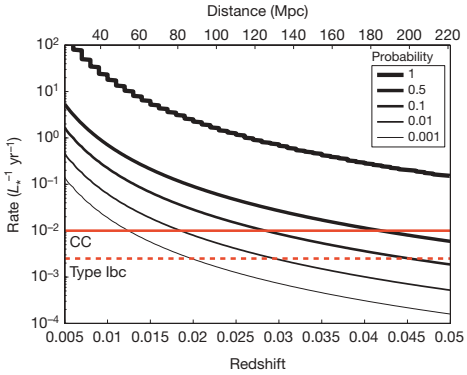

Figure 5 | Volumetric rate of X-ray outbursts similar to XRO 080109. We use all XRT observations longer than 300 s along with the field of view (24 arcmin on a side), the number density of L_* galaxies ($\phi \approx 0.05\ L_*\ \mathrm{Mpc}^{-3}$), and the detectability limit of XRT for events like XRO 080109 ($d \lesssim 200$ Mpc). The curves indicate the rate ($L_*^{-1}\ \mathrm{Mpc}^{-3}\ \mathrm{yr}^{-1}$) inferred from one detection in a total of about 2 yr of effective on-sky XRT observations as a function of the distance to which XROs can be detected. Also shown are the rates[40] of core-collapse supernovae (CC; solid horizontal line) and type Ibc supernovae (dashed horizontal line) as determined from optical supernova searches. The rate of events like XRO 080109 is consistent with the core-collapse rate at the 50% probability level.

Finally, we note that NGC 2770 hosted an unusually high rate of three type Ibc supernovae in the past 10 yr. However, the galaxy has a typical luminosity ($0.3\,L_*$) and a total star formation rate of only 0.5–1 $M_\odot\ \mathrm{yr}^{-1}$ (see Supplementary Information), two orders of magnitude lower than the extreme starburst galaxy Arp 220, which has[43] a supernova rate of $4 \pm 2\,\mathrm{yr}^{-1}$. The elevated supernova rate in NGC 2770, with a chance probability of $\sim 10^{-4}$, may simply be a statistical fluctuation, given the sample of $\sim 4 \times 10^3$ known supernova host galaxies. Alternatively, it may point to a recent episode of increased star formation activity, perhaps triggered by interaction with the companion galaxy NGC 2770B at a separation[44] of only 22 kpc.

Implications for supernova progenitors

Our observations probe the explosion ejecta over a wide range in velocity, $\sim$10,000–210,000 $\mathrm{km\,s}^{-1}$. Taken together, the material giving rise to the X-ray outburst, the radio emission, and the optical light traces an ejecta profile of $E_\mathrm{K} \propto (\gamma\beta)^{-4}$ up to trans-relativistic velocities. This profile is in good agreement with theoretical expectations[24] for a standard hydrodynamic spherical explosion of a compact star, but much steeper[39] than for relativistic GRB-associated supernovae.

On the other hand, we note the similarity between the shock break-out properties of the He-rich SN 2008D and the He-poor GRB-associated SN 2006aj, both suggestive of a dense stellar wind around a compact Wolf-Rayet progenitor. In the context of type Ibc supernovae and GRB progenitors, this provides evidence for continuity (and probably a single progenitor system) between He-rich and He-poor explosions, perhaps including GRBs.

Looking forward, our inference that every core-collapse supernova is marked by an XRO places the discovery and study of supernovae on the threshold of a major change. An all-sky X-ray satellite with a sensitivity similar to that of the Swift/XRT would detect and localize several hundred core-collapse supernovae per year, even if they are obscured by dust, at the time of explosion. As we have shown here, this would enable a clear mapping between the properties of the progenitors and those of the supernovae. Most important, however, X-ray outbursts will provide an unprecedented positional and temporal trigger for neutrino and gravitational wave detectors (such as IceCube and Advanced LIGO), which may ultimately hold the key to unlocking the mystery of the supernova explosion mechanism, and perhaps the identity of the compact remnants.

Received 11 February; accepted 4 April 2008.

1. Woosley, S. E. & Weaver, T. A. The physics of supernova explosions. *Annu. Rev. Astron. Astrophys.* **24,** 205–253 (1986).
2. Filippenko, A. V. Optical spectra of supernovae. *Annu. Rev. Astron. Astrophys.* **35,** 309–355 (1997).
3. Arnett, W. D., Bahcall, J. N., Kirshner, R. P. & Woosley, S. E. Supernova 1987A. *Annu. Rev. Astron. Astrophys.* **27,** 629–700 (1989).
4. Colgate, S. A. Early gamma rays from supernovae. *Astrophys. J.* **187,** 333–336 (1974).
5. Klein, R. I. & Chevalier, R. A. X-ray bursts from Type II supernovae. *Astrophys. J.* **223,** L109–L112 (1978).
6. Waxman, E., Mészáros, P. & Campana, S. GRB 060218: A relativistic supernova shock breakout. *Astrophys. J.* **667,** 351–357 (2007).
7. Cappa, C., Goss, W. M. & van der Hucht, K. A. A Very Large Array 3.6 centimeter continuum survey of galactic Wolf-Rayet stars. *Astrophys. J.* **127,** 2885–2897 (2004).
8. Woosley, S. E., Hegar, A. & Weaver, T. A. The evolution and explosion of massive stars. *Astrophys. J.* **74,** 1015–1071 (2002).
9. MacFadyen, A. I., Woosley, S. E. & Hegar, A. Supernovae, jets, and collapsars. *Astrophys. J.* **550,** 410–425 (2001).
10. Soderberg, A. M. *et al.* The sub-energetic γ-ray burst GRB 031203 as a cosmic analogue to the nearby GRB 980425. *Nature* **430,** 648–650 (2004).
11. Page, K. L. *et al.* Observations of an X-ray transient in NGC 2770. *GCN Rep.* 110 (2008).
12. Deng, J. & Zhu, Y. Bright X-ray transient (a XRF?) in NGC 2770 - a SN optical counterpart? *GCN Circ.* 7160 (2008).
13. Valenti, S., Turatto, M., Navasardyan, H., Benetti, S. & Cappellaro, E. Early OT detection of XRF in NGC 2770 in asiago frames. *GCN Circ.* 7163 (2008).
14. Malesani, D. *et al.* Transient in NGC 2770: Spectroscopic evidence for a SN. *GCN Circ.* 7169 (2008).
15. Li, W. & Filippenko, A. V. Supernova 2008D in NGC 2770. *Cent. Bur. Electron. Telegr.* 1202 (2008).
16. Modjaz, M. *et al.* Supernova 2008D in NGC 2770. *Cent. Bur. Electron. Telegr.* 1222 (2008).
17. Pian, E. *et al.* An optical supernova associated with the X-ray flash XRF 060218. *Nature* **442,** 1011–1013 (2006).
18. Campana, S. *et al.* The association of GRB 060218 with a supernova and the evolution of the shock wave. *Nature* **442,** 1008–1010 (2006).
19. Soderberg, A. M. *et al.* An HST study of the supernovae accompanying GRB 040924 and GRB 041006. *Astrophys. J.* **636,** 391–399 (2006).
20. Sari, R., Piran, T. & Narayan, R. Spectra and light curves of gamma-ray burst afterglows. *Astrophys. J.* **497,** 17–20 (1998).
21. Waxman, E. & Loeb, A. TeV neutrinos and GeV photons from shock breakout in supernovae. *Phys. Rev. Lett.* **87,** 071101 (2001).
22. Wang, X.-Y., Li, Z., Waxman, E. & Mészáros, P. Nonthermal gamma-ray/X-ray flashes from shock breakout in gamma-ray burst-associated supernovae. *Astrophys. J.* **664,** 1026–1032 (2007).
23. Moffat, A. F. J., Drissen, L. & Robert, C. in *Physics of Luminous Blue Variables* (eds Davidson, K., Moffat, A. F. J. & Lamers, H. J. G. L. M.) 229–237 (IAU Colloq. 113, Kluwer Academic, Dordrecht, 1989).
24. Matzner, C. D. & McKee, C. F. The expulsion of stellar envelopes in core-collapse supernovae. *Astrophys. J.* **510,** 379–403 (1999).
25. Valenti, S. *et al.* The broad-lined Type Ic supernova 2003jd. *Mon. Not. R. Astron. Soc.* **383,** 1485–1500 (2008).
26. Arnett, W. D. Type I supernovae. I – Analytic solutions for the early part of the light curve. *Astrophys. J.* **253,** 785–797 (1982).
27. Soderberg, A. M. *et al.* The radio and X-ray-luminous Type Ibc supernova 2003L. *Astrophys. J.* **621,** 908–920 (2005).
28. Berger, E., Kulkarni, S. R. & Frail, D. A. A standard kinetic energy reservoir in gamma-ray burst afterglows. *Astrophys. J.* **590,** 379–385 (2003).
29. Frail, D. A., Kulkarni, S. R., Berger, E. & Wieringa, M. H. A complete catalog of radio afterglows: The first five years. *Astron. J.* **125,** 2299–2306 (2003).
30. Berger, E., Kulkarni, S. R., Frail, D. A. & Soderberg, A. M. A radio survey of Type Ib and Ic supernovae: Searching for engine-driven supernovae. *Astrophys. J.* **599,** 408–418 (2003).
31. Kouveliotou, C. *et al.* Chandra observations of the X-ray environs of SN 1998bw/GRB 980425. *Astrophys. J.* **608,** 872–882 (2004).
32. Chevalier, R. A. Self-similar solutions for the interaction of stellar ejecta with an external medium. *Astrophys. J.* **258,** 790–797 (1982).
33. Readhead, A. C. S. Equipartition brightness temperature and the inverse Compton catastrophe. *Astrophys. J.* **426,** 51–59 (1994).
34. Kulkarni, S. R. *et al.* Radio emission from the unusual supernova 1998bw and its association with the γ-ray burst of 25 April 1998. *Nature* **395,** 663–669 (1998).
35. Waxman, E. The nature of GRB 980425 and the search for off-axis gamma-ray burst signatures in nearby Type Ib/c supernova emission. *Astrophys. J.* **602,** 886–891 (2004).
36. Soderberg, A. M., Nakar, E., Berger, E. & Kulkarni, S. R. Late-time radio observations of 68 Type Ibc supernovae: Strong constraints on off-axis gamma-ray bursts. *Astrophys. J.* **638,** 930–937 (2006).
37. Blanton, M. R. *et al.* The galaxy luminosity function and luminosity density at redshift $z = 0.1$. *Astrophys. J.* **592,** 819–838 (2003).
38. Schmidt, M. Luminosity function of gamma-ray bursts derived without benefit of redshifts. *Astrophys. J.* **552,** 36–41 (2001).
39. Soderberg, A. M. *et al.* Relativistic ejecta from X-ray flash XRF 060218 and the rate of cosmic explosions. *Nature* **442,** 1014–1017 (2006).
40. Cappellaro, E., Evans, R. & Turatto, M. A new determination of supernova rates and a comparison with indicators for galactic star formation. **351,** 459–466 (1999).
41. Band, D. L. Postlaunch analysis of Swift's gamma-ray burst detection sensitivity. *Astrophys. J.* **644,** 378–384 (2006).
42. Dahlen, T. *et al.* High-redshift supernova rates. *Astrophys. J.* **613,** 189–199 (2004).
43. Lonsdale, C. J., Diamond, P. J., Thrall, H., Smith, H. E. & Lonsdale, C. J. VLBI images of 49 radio supernovae in Arp 220. *Astrophys. J.* **647,** 185–193 (2006).
44. Fynbo, J. P. U., Malesani, D., Augusteijn, T. & Niemi, S.-M. NGC 2770B has the same redshift as NGC 2770. *GCN Circ.* 7186 (2008).

Supplementary Information is linked to the online version of the paper at www.nature.com/nature.

Acknowledgements This Article is based in part on observations obtained at the Gemini Observatory through the Director's Discretionary Time. Gemini is operated by the Association of Universities for Research in Astronomy, Inc., under a cooperative agreement with the NSF on behalf of the Gemini partnership: the NSF (US), the STFC (UK), the NRC (Canada), CONICYT (Chile), the ARC (Australia), CNPq (Brazil) and SECYT (Argentina). The VLA is operated by NRAO, a facility of the NSF operated under cooperative agreement by Associated Universities, Inc. Some of the data presented herein were obtained at the W. M. Keck Observatory, which is operated as a scientific partnership among the California Institute of Technology, the University of California and NASA. The Observatory was made possible by the financial support of the W. M. Keck Foundation. A.M.S. acknowledges support by NASA through a Hubble Fellowship.

Author Information Reprints and permissions information is available at www.nature.com/reprints. Correspondence and requests for materials should be addressed to A.M.S. (alicia@astro.princeton.edu).

CORRIGENDUM

doi:10.1038/nature07133

Neurophysiology: Sensing temperature without ion channels

Brandon R. Brown

Nature 421, 495 (2003)

My Brief Communication about thermoelectricity in shark gels neglected a systematic effect of surface electrochemistry: electrode potentials vary with temperature in electrolyte solutions. However, silver leads in sea water[1] and accepted values for likely electrode reactions[2] show a sign opposing the gel signals, making it unlikely that an artefactual signal is the origin. Our subsequent work[3] discussed artefacts and repeated the signal with platinum electrodes. Although another report[4] finds a zero signal using salt bridges, it ignores thermopower in gel-filled leads, which risks building a 'null thermocouple' from two similar materials (see ref. 5, for example). A temperature function of the electrosensors is not known, but the thermoelectric transduction hypothesis still stands.

1. Sanford, T. B. *Measurements and Interpretations of Motional Electric Fields in the Sea.* PhD thesis, Massachusetts Institute of Technology (1967).
2. Milazzo, G. & Caroli, S. *Tables of Standard Electrochemical Potentials* (John Wiley and Sons, New York, 1978).
3. Brown, B. R., Hughes, M. E. & Russo, C. Thermoelectricity in natural and synthetic hydrogels. *Phys. Rev. E* **70**, 031917 (2004).
4. Fields, R. D., Fields, K. D. & Fields, M. C. Semiconductor gel in shark sense organs? *Neurosci. Lett.* **426**, 166–170 (2007).
5. Kasap, S. O. *Principles of Electronic Materials and Devices* 278–284 (McGraw Hill, San Francisco, 2000).

CORRIGENDUM

doi:10.1038/nature07134

An extremely luminous X-ray outburst at the birth of a supernova

A. M. Soderberg, E. Berger, K. L. Page, P. Schady, J. Parrent, D. Pooley, X.-Y. Wang, E. O. Ofek, A. Cucchiara, A. Rau, E. Waxman, J. D. Simon, D. C.-J. Bock, P. A. Milne, M. J. Page, J. C. Barentine, S. D. Barthelmy, A. P. Beardmore, M. F. Bietenholz, P. Brown, A. Burrows, D. N. Burrows, G. Bryngelson, S. B. Cenko, P. Chandra, J. R. Cummings, D. B. Fox, A. Gal-Yam, N. Gehrels, S. Immler, M. Kasliwal, A. K. H. Kong, H. A. Krimm, S. R. Kulkarni, T. J. Maccarone, P. Mészáros, E. Nakar, P. T. O'Brien, R. A. Overzier, M. de Pasquale, J. Racusin, N. Rea & D. G. York

Nature 453, 469–474 (2008)

In this Article, the surname of co-author G. Bryngelson was misspelled as G. Byrngelson.

BIBLIOGRAPHY

Aldering, G., Bailey, S., Bongard, S., Kocevski, D., Lee, B. C., Loken, S., Nugent, P., Perlmutter, S., Scalzo, R., Thomas, R. C., Wang, L., Weaver, B. A., Blanc, N., Copin, Y., Gangler, E., Smadja, G., Antilogus, P., Gilles, S., Pain, R., Pereira, R., Pecontal, E., Rigaudier, G., Kessler, R., Baltay, C., Rabinowitz, D., and Bauer, A. 2006. Classification of SNe 2006D, a Premaximum Type Ia Supernova. *The Astronomer's Telegram 689*, 1–+.

Arbour, R. 2007. Supernova 2007ax in NGC 2577. *Central Bureau Electronic Telegrams 904*, 1–+.

Axelrod, T. S. 1980. Late time optical spectra from the Ni-56 model for Type 1 supernovae. Ph.D. thesis, AA(California Univ., Santa Cruz.).

Berger, E. and Soderberg, A. 2008. Extremely Bright X-ray Transient Likely in NGC 2770. *The Astronomer's Telegram 1353*, 1–+.

Blondin, S., Modjaz, M., Kirshner, R., Challis, P., Matheson, T., and Calkins, M. 2007. Supernova 2007ax in NGC 2577. *Central Bureau Electronic Telegrams 907*, 1–+.

Branch, D. 1982. Type I supernovae - Observational constraints. In *NATO ASIC Proc. 90: Supernovae: A Survey of Current Research*, V. L. Trimble, Ed. 267–279.

Branch, D., Romanishin, W., and Baron, E. 1996. Statistical Connections between the Properties of Type IA Supernovae and the B-V Colors of Their Parent Galaxies, and the Value of H 0. *Astrophys. J. 465*, 73–+.

Chan, K.-W. and Lingenfelter, R. E. 1993. Positrons from supernovae. *Astrophys. J. 405*, 614–636.

Clayton, D. D. 1983. *Principles of stellar evolution and nucleosynthesis*. Chicago: University of Chicago Press, 1983.

Colesanti, C., Jacques, C., Pimentel, E., and Napoleao, T. 2006. Supernova 2006D in MCG -01-33-34. *Central Bureau Electronic Telegrams 362*, 1–+.

Colgate, S. A. and McKee, C. 1969. Early Supernova Luminosity. *Astrophys. J. 157*, 623–+.

Colgate, S. A., Petschek, A. G., and Kriese, J. T. 1980. The luminosity of type I supernovae. *Astrophys. J. Lett. 237*, L81–L85.

Contardo, G., Leibundgut, B., and Vacca, W. D. 2000. Epochs of maximum light and bolometric light curves of type Ia supernovae. *A&A 359*, 876–886.

Cumming, A. 2004. REVIEW: Magnetic Field Evolution in Accreting White Dwarfs. In *IAU Colloq. 190: Magnetic Cataclysmic Variables*, S. Vrielmann and M. Cropper, Eds. Astronomical Society of the Pacific Conference Series, vol. 315. 58–+.

Filippenko, A. V. 1997. Optical Spectra of Supernovae. *ARA&A 35*, 309–355.

Filippenko, A. V., Richmond, M. W., Matheson, T., Shields, J. C., Burbidge, E. M., Cohen, R. D., Dickinson, M., Malkan, M. A., Nelson, B., Pietz, J., Schlegel, D., Schmeer, P., Spinrad, H., Steidel, C. C., Tran, H. D., and Wren, W. 1992. The peculiar Type IA SN 1991T - Detonation of a white dwarf? *Astrophys. J. Lett. 384*, L15–L18.

Freedman, W. L., Madore, B. F., Gibson, B. K., Ferrarese, L., Kelson, D. D., Sakai, S., Mould, J. R., Kennicutt, Jr., R. C., Ford, H. C., Graham, J. A., Huchra, J. P., Hughes, S. M. G., Illingworth, G. D., Macri, L. M., and Stetson, P. B. 2001. Final Results from the Hubble Space Telescope Key Project to Measure the Hubble Constant. *Astrophys. J. 553*, 47–72.

Garnavich, P. M., Bonanos, A. Z., Krisciunas, K., Jha, S., Kirshner, R. P., Schlegel, E. M., Challis, P., Macri, L. M., Hatano, K., Branch, D., Bothun, G. D., and Freedman, W. L. 2004. The Luminosity of SN 1999by in NGC 2841 and the Nature of "Peculiar" Type Ia Supernovae. *Astrophys. J. 613*, 1120–1132.

Hamuy, M., Phillips, M. M., Suntzeff, N. B., Schommer, R. A., Maza, J., Smith, R. C., Lira, P., and Aviles, R. 1996. The Morphology of Type IA Supernovae Light Curves. *Astronom. J. 112*, 2438–+.

Hillebrandt, W. and Niemeyer, J. C. 2000. Type IA Supernova Explosion Models. *ARA&A 38*, 191–230.

Hoeflich, P. and Khokhlov, A. 1996. Explosion Models for Type IA Supernovae: A Comparison with Observed Light Curves, Distances, H 0, and Q 0. *Astrophys. J. 457*, 500–+.

Howell, S. B. 2000. *Handbook of CCD Astronomy.* Handbook of CCD astronomy / Steve B. Howell. Cambridge, U.K. ; New York : Cambridge University Press, c2000. (Cambridge observing handbooks for research astronomers ; 2).

Hubble, E. 1929. A Relation between Distance and Radial Velocity among Extra-Galactic Nebulae. *Proceedings of the National Academy of Science 15*, 168–173.

Hubble, E. 1938. Adventures in Cosmology. *Leaflet of the Astronomical Society of the Pacific 3*, 120–+.

Kasen, D. 2006. Secondary Maximum in the Near-Infrared Light Curves of Type Ia Supernovae. *Astrophys. J. 649*, 939–953.

Kasliwal, M. M., Ofek, E. O., Gal-Yam, A., Rau, A., Brown, P. J., Cenko, S. B., Cameron, P. B., Quimby, R., Kulkarni, S. R., Bildsten, L., Milne, P., and Bryngelson, G. 2008. SN 2007ax: An Extremely Faint Type Ia Supernova. *Astrophys. J. Lett. 683*, L29–L32.

Khokhlov, A. M. 1991. Delayed detonation model for type IA supernovae. *A&A 245*, 114–128.

Kotake, K., Sato, K., and Takahashi, K. 2006. Explosion mechanism, neutrino burst and gravitational wave in core-collapse supernovae. *Reports of Progress in Physics 69*, 971–1143.

Lair, J. C., Leising, M. D., Milne, P. A., and Williams, G. G. 2006. Late Light Curves of Normal Type Ia Supernovae. *Astronom. J. 132*, 2024–2033.

Leibundgut, B. 1988. Light curves of supernovae type, I. Ph.D. thesis, PhD thesis. Univ. Basel.137 pp. , (1988).

Li, W. and Filippenko, A. V. 2008. Supernova 2008D in NGC 2770. *Central Bureau Electronic Telegrams 1202*, 3–+.

Li, W., Filippenko, A. V., Chornock, R., Berger, E., Berlind, P., Calkins, M. L., Challis, P., Fassnacht, C., Jha, S., Kirshner, R. P., Matheson, T., Sargent, W. L. W., Simcoe, R. A., Smith, G. H., and Squires, G. 2003. SN 2002cx: The Most Peculiar Known Type Ia Supernova. *PASP 115*, 453–473.

Li, W., Filippenko, A. V., Gates, E., Chornock, R., Gal-Yam, A., Ofek, E. O., Leonard, D. C., Modjaz, M., Rich, R. M., Riess, A. G., and Treffers, R. R. 2001a. The Unique Type Ia Supernova 2000cx in NGC 524. *PASP 113*, 1178–1204.

Li, W., Filippenko, A. V., Treffers, R. R., Riess, A. G., Hu, J., and Qiu, Y. 2001b. A High Intrinsic Peculiarity Rate among Type IA Supernovae. *Astrophys. J. 546*, 734–743.

Liebert, J. 1995. Isolated Magnetic White Dwarfs. In *Magnetic Cataclysmic Variables*, D. A. H. Buckley and B. Warner, Eds. Astronomical Society of the Pacific Conference Series, vol. 85. 59–+.

Mackay, C. D. 1986. Charge-coupled devices in astronomy. *ARA&A 24*, 255–283.

Mazzali, P. A., Chugai, N., Turatto, M., Lucy, L. B., Danziger, I. J., Cappellaro, E., della Valle, M., and Benetti, S. 1997. The properties of the peculiar type IA supernova 1991bg - II. The amount of ˆ56Ni and the total ejecta mass determined from spectrum synthesis and energetics considerations. *MNRAS 284*, 151–171.

Mazzali, P. A., Nomoto, K., Cappellaro, E., Nakamura, T., Umeda, H., and Iwamoto, K. 2001. Can Differences in the Nickel Abundance in Chandrasekhar-Mass Models Explain the Relation between the Brightness and Decline Rate of Normal Type IA Supernovae? *Astrophys. J. 547*, 988–994.

Milne, P. A., The, L.-S., and Leising, M. D. 1999. Positron Escape from Type IA Supernovae. *Astrophys. J. Suppl. 124*, 503–526.

Milne, P. A., The, L.-S., and Leising, M. D. 2001. Late Light Curves of Type Ia Supernovae. *Astrophys. J. 559*, 1019–1031.

Morrell, N. and Folatelli, G. 2007. Supernovae 2007aw, 2007ax, 2007ay. *Central Bureau Electronic Telegrams 908*, 1–+.

Nadyozhin, D. K. 1994. The properties of NI to CO to Fe decay. *Astrophys. J. Suppl. 92*, 527–531.

Nomoto, K., Thielemann, F.-K., and Yokoi, K. 1984. Accreting white dwarf models of Type I supernovae. III - Carbon deflagration supernovae. *Astrophys. J. 286*, 644–658.

Nugent, P., Baron, E., Branch, D., Fisher, A., and Hauschildt, P. H. 1997. Synthetic Spectra of Hydrodynamic Models of Type IA Supernovae. *Astrophys. J. 485*, 812–+.

Page, K. L., Immler, S., Beardmore, A. P., Burrows, D. N., Gehrels, N., Soderberg, A., and Berger, E. 2008. Observations of an X-ray transient in NGC 2770. *GCNR, 110, 1 (2008) 110*, 1–+.

Perlmutter, S. 2003. Supernovae, Dark Energy, and the Accelerating Universe. *Physics Today 56*, 53–60.

Perlmutter, S., Gabi, S., Goldhaber, G., Goobar, A., Groom, D. E., Hook, I. M., Kim, A. G., Kim, M. Y., Lee, J. C., Pain, R., Pennypacker, C. R., Small, I. A., Ellis, R. S., McMahon, R. G., Boyle, B. J., Bunclark, P. S., Carter, D., Irwin, M. J., Glazebrook, K., Newberg, H. J. M., Filippenko, A. V., Matheson, T., Dopita, M., Couch, W. J., and The Supernova Cosmology Project. 1997. Measurements of the Cosmological Parameters Omega and Lambda from the First Seven Supernovae at Z $\geq$ 0.35. *Astrophys. J. 483*, 565–+.

Phillips, M. M. 1993. The absolute magnitudes of Type IA supernovae. *Astrophys. J. Lett. 413*, L105–L108.

Phillips, M. M., Wells, L. A., Suntzeff, N. B., Hamuy, M., Leibundgut, B., Kirshner, R. P., and Foltz, C. B. 1992. SN 1991T - Further evidence of the heterogeneous nature of type IA supernovae. *Astronom. J. 103*, 1632–1637.

Pinto, P. A. and Eastman, R. G. 2000. The Physics of Type IA Supernova Light Curves. II. Opacity and Diffusion. *Astrophys. J. 530*, 757–776.

Reinsch, K., Euchner, F., Beuermann, K., and Jordan, S. 2004. Magnetic Field Topology of Accreting White Dwarfs. In *IAU Colloq. 190: Magnetic Cataclysmic Variables*, S. Vrielmann and M. Cropper, Eds. Astronomical Society of the Pacific Conference Series, vol. 315. 71–+.

Riess, A. G., Filippenko, A. V., Challis, P., Clocchiatti, A., Diercks, A., Garnavich, P. M., Gilliland, R. L., Hogan, C. J., Jha, S., Kirshner, R. P., Leibundgut, B., Phillips, M. M., Reiss, D., Schmidt, B. P., Schommer, R. A., Smith, R. C., Spyromilio, J., Stubbs, C., Suntzeff, N. B., and Tonry, J. 1998. Observational Evidence from Supernovae for an Accelerating Universe and a Cosmological Constant. *Astronom. J. 116*, 1009–1038.

Riess, A. G., Kirshner, R. P., Schmidt, B. P., Jha, S., Challis, P., Garnavich, P. M., Esin, A. A., Carpenter, C., Grashius, R., Schild, R. E., Berlind, P. L., Huchra, J. P., Prosser, C. F., Falco, E. E., Benson, P. J., Briceño, C., Brown, W. R., Caldwell, N., dell'Antonio, I. P., Filippenko, A. V., Goodman, A. A., Grogin, N. A., Groner, T., Hughes, J. P., Green, P. J., Jansen, R. A., Kleyna, J. T., Luu, J. X., Macri, L. M., McLeod, B. A., McLeod, K. K., McNamara, B. R., McLean, B., Milone, A. A. E., Mohr, J. J., Moraru, D., Peng, C., Peters, J., Prestwich, A. H., Stanek, K. Z., Szentgyorgyi, A., and Zhao, P. 1999. BVRI Light Curves for 22 Type IA Supernovae. *Astronom. J. 117*, 707–724.

Riess, A. G., Press, W. H., and Kirshner, R. P. 1996. A Precise Distance Indicator: Type IA Supernova Multicolor Light-Curve Shapes. *Astrophys. J. 473*, 88–+.

Ruiz-Lapuente, P. and Spruit, H. C. 1998. Bolometric Light Curves of Supernovae and Postexplosion Magnetic Fields. *Astrophys. J. 500*, 360–+.

Sandage, A., Tammann, G. A., Saha, A., Reindl, B., Macchetto, F. D., and Panagia, N. 2006. The Hubble Constant: A Summary of the Hubble Space Telescope Program for the Luminosity Calibration of Type Ia Supernovae by Means of Cepheids. *Astrophys. J. 653*, 843–860.

Slipher, V. M. 1915. Spectrographic Observations of Nebulae. *Popular Astronomy 23*, 21–24.

Soderberg, A. M., Berger, E., Page, K. L., Schady, P., Parrent, J., Pooley, D., Wang, X.-Y., Ofek, E. O., Cucchiara, A., Rau, A., Waxman, E., Simon, J. D., Bock, D. C.-J., Milne, P. A., Page, M. J., Barentine, J. C., Barthelmy, S. D., Beardmore, A. P., Bietenholz, M. F., Brown, P., Burrows, A., Burrows, D. N., Byrngelson, G., Cenko, S. B., Chandra, P., Cummings, J. R., Fox, D. B., Gal-Yam, A., Gehrels, N., Immler, S., Kasliwal, M., Kong, A. K. H., Krimm, H. A., Kulkarni, S. R., Maccarone, T. J., Mészáros, P., Nakar, E., O'Brien, P. T., Overzier, R. A., de Pasquale, M., Racusin, J., Rea, N., and York, D. G. 2008. An extremely luminous X-ray outburst at the birth of a supernova. *Nature 453*, 469–474.

Sollerman, J., Lindahl, J., Kozma, C., Challis, P., Filippenko, A. V., Fransson, C., Garnavich, P. M., Leibundgut, B., Li, W., Lundqvist, P., Milne, P., Spyromilio, J., and Kirshner, R. P. 2004. The late-time light curve of the type Ia supernova 2000cx. *A&A 428*, 555–568.

Stritzinger, M. and Sollerman, J. 2007. Late-time emission of type Ia supernovae: optical and near-infrared observations of SN 2001el. *A&A 470*, L1–L4.

Thomas, R. C., Aldering, G., Antilogus, P., Aragon, C., Bailey, S., Baltay, C., Baron, E., Bauer, A., Buton, C., Bongard, S., Copin, Y., Gangler, E., Gilles, S., Kessler, R., Loken, S., Nugent, P., Pain, R., Parrent, J., Pécontal, E., Pereira, R., Perlmutter, S., Rabinowitz, D., Rigaudier, G., Runge, K., Scalzo, R., Smadja, G., Wang, L., and Weaver, B. A. 2007. Nearby Supernova Factory Observations of SN 2006D: On Sporadic Carbon Signatures in Early Type Ia Supernova Spectra. *Astrophys. J. Lett. 654*, L53–L56.

Turatto, M., Benetti, S., Cappellaro, E., Danziger, I. J., Della Valle, M., Gouiffes, C., Mazzali, P. A., and Patat, F. 1996. The properties of the peculiar type Ia supernova 1991bg. I. Analysis and discussion of two years of observations. *MNRAS 283*, 1–17.

Whelan, J. and Iben, I. J. 1973. Binaries and Supernovae of Type I. *Astrophys. J. 186*, 1007–1014.

Winget, D. E., Hansen, C. J., Liebert, J., van Horn, H. M., Fontaine, G., Nather, R. E., Kepler, S. O., and Lamb, D. Q. 1987. An independent method for determining the age of the universe. *Astrophys. J. Lett. 315*, L77–L81.

Woosley, S. E., Kasen, D., Blinnikov, S., and Sorokina, E. 2007. Type Ia Supernova Light Curves. *Astrophys. J. 662*, 487–503.